



NAVAL POSTGRADUATE SCHOOL

MONTEREY, CALIFORNIA

DISSERTATION

**THE BERING SEA: COMMUNICATION WITH THE
WESTERN SUBARCTIC GYRE, MESOSCALE ACTIVITY,
SHELF-BASIN EXCHANGE, AND THE FLOW THROUGH
BERING STRAIT**

by

Jaclyn Clement Kinney

March 2011

Dissertation Supervisor:

Wieslaw Maslowski

Approved for public release; distribution is unlimited.

THIS PAGE INTENTIONALLY LEFT BLANK

REPORT DOCUMENTATION PAGE			<i>Form Approved OMB No. 0704-0188</i>	
Public reporting burden for this collection of information is estimated to average 1 hour per response, including the time for reviewing instruction, searching existing data sources, gathering and maintaining the data needed, and completing and reviewing the collection of information. Send comments regarding this burden estimate or any other aspect of this collection of information, including suggestions for reducing this burden, to Washington headquarters Services, Directorate for Information Operations and Reports, 1215 Jefferson Davis Highway, Suite 1204, Arlington, VA 22202-4302, and to the Office of Management and Budget, Paperwork Reduction Project (0704-0188) Washington DC 20503.				
1. AGENCY USE ONLY (Leave blank)		2. REPORT DATE March 2011	3. REPORT TYPE AND DATES COVERED Dissertation	
4. TITLE AND SUBTITLE: The Bering Sea: Communication With the Western Subarctic Gyre, Mesoscale Activity, Shelf-Basin Exchange and the Flow Through Bering Strait			5. FUNDING NUMBERS	
6. AUTHOR(S) Jaclyn Clement Kinney			8. PERFORMING ORGANIZATION REPORT NUMBER	
7. PERFORMING ORGANIZATION NAME(S) AND ADDRESS(ES) Naval Postgraduate School Monterey, CA 93943-5000			10. SPONSORING / MONITORING AGENCY REPORT NUMBER	
9. SPONSORING / MONITORING AGENCY NAME(S) AND ADDRESS(ES) N/A			11. SUPPLEMENTARY NOTES The views expressed in this thesis are those of the author and do not reflect the official policy or position of the Department of Defense or the U.S. Government. IRB Protocol Number ____ N/A ____	
12a. DISTRIBUTION / AVAILABILITY STATEMENT Approved for public release; distribution is unlimited.			12b. DISTRIBUTION CODE	
13. ABSTRACT) A 1/12th-degree, pan-Arctic ice-ocean numerical model is used to better understand the circulation and exchanges in the Bering Sea. Understanding the physical oceanography of the Bering Sea is significant for the U.S. Navy due to the expected increase in ship traffic and exploration of natural resources that will likely coincide with the ongoing retreat of sea ice in the Western Arctic. This model represents a large step forward in the ability to simulate the mesoscale eddies and meanders in the Alaskan Stream and the deep Bering Sea basin, which are shown to exert a strong control on the flow into and out of the western Aleutian Island passes. Model results show that upwelling of deep Bering Sea water, which is the primary source of nutrients for important ecosystems of the Bering, Chukchi, and Beaufort seas, is enhanced by the presence of cyclonic eddies in the vicinity of canyons along the slope. High values of eddy kinetic energy in Bering and Anadyr straits help explain the areas of high biological productivity located just downstream in the Chirikov Basin and north of Bering Strait. Model results show significant horizontal and vertical shear in the flow through Bering Strait, and indicate a need for more observations of the flow structure on a continuous basis.				
14. SUBJECT TERMS Bering Sea, Physical Oceanography, Polar Oceanography, Arctic Oceanography			15. NUMBER OF PAGES 162	
			16. PRICE CODE	
17. SECURITY CLASSIFICATION OF REPORT Unclassified	18. SECURITY CLASSIFICATION OF THIS PAGE Unclassified	19. SECURITY CLASSIFICATION OF ABSTRACT Unclassified	20. LIMITATION OF ABSTRACT UU	

THIS PAGE INTENTIONALLY LEFT BLANK

Approved for public release; distribution is unlimited

**THE BERING SEA: COMMUNICATION WITH THE WESTERN SUBARCTIC
GYRE, MESOSCALE ACTIVITY, SHELF-BASIN EXCHANGE, AND THE
FLOW THROUGH BERING STRAIT**

Jaclyn Clement Kinney
Research Associate, Department of Oceanography, Naval Postgraduate School
M.S., Naval Postgraduate School, 2005

Submitted in partial fulfillment of the
requirements for the degree of

DOCTOR OF PHILOSOPHY IN PHYSICAL OCEANOGRAPHY

from the

**NAVAL POSTGRADUATE SCHOOL
March 2011**

Author:

Jaclyn Clement Kinney

Approved by:

Wieslaw Maslowski
Research Professor of Oceanography
Dissertation Supervisor

John Walsh
Professor of Biological Oceanography

Mary Batteen
Professor of Oceanography

Robin Tokmakian
Research Associate Professor
of Oceanography

Peter Guest
Research Professor of
Meteorology

Approved by:

Jeffery Paduan, Chair, Department of Oceanography

Approved by:

Douglas Moses, Vice Provost for Academic Affairs

THIS PAGE INTENTIONALLY LEFT BLANK

ABSTRACT

A 1/12th-degree, pan-Arctic ice-ocean numerical model is used to better understand the circulation and exchanges in the Bering Sea. Understanding the physical oceanography of the Bering Sea is significant for the U.S. Navy due to the expected increase in ship traffic and exploration of natural resources that will likely coincide with the ongoing retreat of sea ice in the Western Arctic. This model represents a large step forward in the ability to simulate the mesoscale eddies and meanders in the Alaskan Stream and the deep Bering Sea basin, which are shown to exert a strong control on the flow into and out of the western Aleutian Island passes. Model results show that upwelling of deep Bering Sea water, which is the primary source of nutrients for important ecosystems of the Bering, Chukchi, and Beaufort seas, is enhanced by the presence of cyclonic eddies in the vicinity of canyons along the slope. High values of eddy kinetic energy in Bering and Anadyr straits help explain the areas of high biological productivity located just downstream in the Chirikov Basin and north of Bering Strait. Model results show significant horizontal and vertical shear in the flow through Bering Strait, and indicate a need for more observations of the flow structure on a continuous basis.

THIS PAGE INTENTIONALLY LEFT BLANK

TABLE OF CONTENTS

I.	INTRODUCTION.....	1
A.	GEOGRAPHY OF THE BERING SEA.....	1
B.	MAJOR FEATURES OF THE BERING SEA	3
C.	SIGNIFICANCE OF THE BERING SEA	4
II.	MODEL DESCRIPTION.....	7
III.	ORGANIZATION OF THE DISSERTATION	11
IV.	THE DEEP BERING SEA AND WESTERN SUBARCTIC GYRE COMMUNICATION.....	13
A.	INTRODUCTION.....	13
B.	GENERAL CIRCULATION.....	14
C.	VOLUME AND PROPERTY FLUX ACROSS THE ALEUTIAN ISLAND PASSES.....	16
1.	Comparison of Observed and Modeled Volume Transports.....	18
2.	Modeled Heat Fluxes	23
3.	Modeled Freshwater Fluxes	24
D.	MESOSCALE EDDIES IN THE ALASKAN STREAM AND THE DEEP BASIN.....	26
1.	Eddies in the Deep Bering Sea Basin.....	26
2.	Eddies in the Alaskan Stream.....	32
E.	CONCLUSIONS	36
V.	SHELF-BASIN EXCHANGE AND OUTER SHELF DYNAMICS.....	39
A.	INTRODUCTION.....	39
B.	GENERAL CIRCULATION.....	40
C.	VOLUME TRANSPORT	42
D.	HEAT TRANSPORT	46
E.	SALT AND FRESHWATER TRANSPORT	48
F.	BERING SLOPE CURRENT	49
G.	EXCHANGE IN CANYONS AND THE IMPORTANCE OF EDDIES..	53
H.	CONCLUSIONS	62
VI.	CIRCULATION AND ENERGETICS OF THE NORTHERN BERING SEA ..	65
A.	INTRODUCTION.....	65
B.	VOLUME TRANSPORT THROUGH ANADYR AND SHPANBERG STRAITS	65
C.	ANOMALOUS CIRCULATION EVENT	66
D.	EDDY KINETIC ENERGY.....	71
E.	CONCLUSIONS	75
VII.	THE FLOW THROUGH BERING STRAIT	77
A.	INTRODUCTION.....	77
B.	MODEL DESCRIPTIONS	80

1.	Bering Ecosystem Study Ice-Ocean Modeling and Assimilation System (BESTMAS)	80
2.	Estimating the Circulation and Climate of the Ocean, Phase II (ECCO2)	82
3.	Naval Postgraduate School Arctic Modeling Effort (NAME)	83
4.	Nucleus for European Modelling of the Ocean (NEMO) With ORCA Configuration.....	83
5.	Pan-Arctic Ice-Ocean Modeling and Assimilation System (PIOMAS).....	85
C.	BERING STRAIT OBSERVATIONAL MOORING DATA	85
D.	RESULTS	86
E.	SUMMARY AND CONCLUSIONS	105
VIII.	LINKAGES TO WEATHER INDICES, BIOLOGICAL PRODUCTIVITY, AND THE WESTERN ARCTIC.....	109
A.	LINKAGES TO LARGE-SCALE WEATHER INDICES	109
B.	PHYSICAL IMPACTS ON BIOLOGICAL PROCESSES	116
C.	DOWNSTREAM EFFECTS	117
IX.	OVERALL CONCLUSIONS	121
X.	FUTURE DIRECTIONS.....	123
	LIST OF REFERENCES	125
	INITIAL DISTRIBUTION LIST	141

LIST OF FIGURES

Figure 1.	Model bathymetry (m) and geography of the Bering Sea.....	2
Figure 2.	1/12° ice-ocean model domain and bathymetry (m).	10
Figure 3.	Model bathymetry (m) of the deep Bering Sea. Black lines indicate the locations of cross-sections and white text indicates the names of these cross-sections.	14
Figure 4.	The 26-year mean (1979–2004) upper 100 m circulation (vectors) and total kinetic energy (shading). Magenta contour lines represent bathymetry (m). Every second vector is shown. The direction of the Alaskan Stream is westward.	15
Figure 5.	Monthly mean time series of net volume transport (Sv; red line) through selected sections, as indicated. The black line represents a 13-month running mean and the green line indicates the overall mean. Means for each time series are shown to the right of each panel. Local maxima (red arrows) and minima/flow reversals (blue arrows) are indicated on the Near Strait time series.	21
Figure 6.	Monthly mean (red line), 13-month running mean (black line) and overall mean (green line) heat flux through selected passes as labeled. Heat flux is referenced to the freezing temperature, which is based on salinity.	24
Figure 7.	Monthly mean (red line), 13-month running mean (black line) and overall mean (green line) freshwater flux through selected passes as labeled. Freshwater flux is referenced to 33.8 psu.	26
Figure 8.	June 1987 upper 100 m circulation (vectors) and total kinetic energy (shading). Magenta contour lines represent bathymetry (m). The red line indicates the position of a cross section shown in Figure 5. Every second vector is shown.	27
Figure 9.	Vertical cross-sections of potential temperature (°C; color shading) and velocity (cm/s; contours) along the red line in Figure 4 during (a) June 1987, (b) 26-year mean June, and (c) the difference between these time periods. Solid contour lines indicate northward velocity and dashed lines indicate southward velocity.	30
Figure 10.	Vertical cross-sections of salinity (color shading) and velocity (cm/s; contours) along the red line in Figure 4 during (a) June 1987, (b) 26-year mean June, and (c) difference between these time periods. Solid contour lines indicate northward velocity and dashed lines indicate southward velocity.	31
Figure 11.	Monthly mean total kinetic energy (shading; cm^2/s^2) and velocity vectors (cm/s) in the upper 400 m during each of the flow reversals as shown in Figure 5. The year and month are indicated above each panel. The red line indicates the position of Near Strait and the green contour lines indicate bathymetry.	34

Figure 12.	Monthly mean total kinetic energy (shading; cm^2/s^2) and velocity vectors (cm/s) in the upper 400 m during each of the flow maxima as shown in Figure 5. The year and month are indicated above each panel. The red line indicates the position of Near Strait and the green contour lines indicate bathymetry.....	35
Figure 13.	26-year (1979–2004) mean 0–220m circulation and total kinetic energy. Every second vector is shown.....	40
Figure 14.	Schematic circulation (0–220m) and total kinetic energy based on Figure 13. The locations of model cross-sections and names are included.	42
Figure 15.	26-year (1979–2004) volume transport (Sv; a) and heat flux (TW; relative to -0.1°C ; b) across various sections. Arrows indicate net direction (positive is North or West) and are scaled relative to the largest value in each figure. The shading indicates depth (m). The 50 m and 200 m isobaths are shown as dotted lines. The mean flux divergence for each polygon is shown in italics and is circled.	45
Figure 16.	26-year (1979–2004) mean salt flux (million kg/s; a) and freshwater flux (mSv; relative to $S=34.8$; b) across various sections. Arrows indicate net direction (positive is North or West) and are scaled relative to the largest value in each figure. The shading indicates depth (m). The 50 m and 200 m isobaths are shown as dotted lines. The mean flux divergence for each polygon is shown in italics and is circled.	47
Figure 17.	Locations of Bering Slope Current and canyon cross-sections (solid black lines). The location of the 200-m isobath is shown as a thick dashed line.	50
Figure 18.	Time series of monthly mean volume transport (a,d), heat flux (b,e) and mean temperature (c,f) across BSC1 (top 3 panels) and BSC4 (lower 3 panels). Heat flux is referenced to -0.1°C . The red line represents monthly mean values, while the thick black line represents a 13-month running mean and the horizontal line represents the 26-year mean. Section locations are shown in Figure 17.	51
Figure 19.	Time series of monthly mean heat (a,c) salt (b,d) flux anomaly across BSC3 (a,b) and the Zhemchug Canyon section (C6; c,d) shown in Figure 17. The red line represents monthly mean values, while the black line represents a 13-month running mean and the horizontal green line represents zero. The circles and squares represent the salt and heat flux maximum (November 1993) and minimum (November 1995), respectively through Zhemchug Canyon. The stars represent local peaks in the heat and salt flux anomaly through Zhemchug Canyon associated with eddies shown in Figure 20.....	56
Figure 20.	The bottom water salinity anomaly and sea surface height anomaly contours (blue is positive and red is negative; contour interval of 5 cm) during (a) March 1982, (b) July 1987, (c) November 1993, and (d) May 2002 in the vicinity of Zhemchug Canyon. The vectors represent monthly mean velocity over the entire water column during each respective month....	57

Figure 21.	The vertical section of velocity (contours; cm/s) and salinity anomaly (shading) (a) along the Zhemchug canyon (section BSC3), and (b) cross the Zhemchug canyon (section C6) during November 1993.	58
Figure 22.	Hovmuller plot of temperature anomaly ($^{\circ}\text{C}$; a) and salinity anomaly (b) along the Bering Sea 200-m isobath.	61
Figure 23.	Bathymetry (m) of the northern Bering Sea and locations of cross-sections (thick black lines): BS (Bering Strait), AS (Anadyr Strait), SS (Shpanberg Strait), AC (Anadyr Current), and SL (St. Lawrence Island). The direction of positive flow is northward across BS and SL, northeastward across AS and SS, and eastward across AC.	67
Figure 24.	Monthly mean volume transport over a 23-year time series (1979–2001). Positive fluxes represent flow to the north or east according to the model grid (see Figure 23), while negative fluxes represent flow to the south or west. The smoothed net flux (thick green line) is a 13-month running mean. The 23-yr mean is shown at the end of each time-series.	68
Figure 25.	Sea ice concentration on (A) February 19, 1999 and (B) February 19, 2001 as determined using data obtained from the U.S. National Ice Center (adapted from Clement et al., 2004). Model monthly mean sea ice concentration during (C) February 1999 and (D) February 2001.	70
Figure 26.	Model wind forcing fields averaged over November and December (A) 1998 and (B) 2000. (C) The magnitude difference (2000–1998) and both wind fields (1998 in black; 2000 in white).	71
Figure 27.	Seasonally average EKE at the surface (0–5 m) calculated from daily 1987 snapshots (against the 23-year mean; 1979–2001): (A) Winter (J-F-M) average, (B) Spring (A-M-J) average, (C) Summer (J-A-S) average, and (D) Autumn (O-N-D) average.	73
Figure 28.	Seasonally average EKE at 20–26 m calculated from daily 1987 snapshots (against the 23-year mean; 1979–2001): (A) Winter (J-F-M) average, (B) Spring (A-M-J) average, (C) Summer (J-A-S) average, and (D) Autumn (O-N-D) average.	74
Figure 29.	Bathymetry (m) in the vicinity of the Bering Strait (a). Depth contours are every 10 m from the International Bathymetric Chart of the Arctic Ocean (Jakobsson et al. 2000). Model bathymetry (m) from (b) BESTMAS, (c) ECCO2, (d) NAME, (e) ORCA, and (f) PIOMAS. The approximate locations of the moored observations are indicated with black circles. The cross-sections across Bering Strait are shown as black lines in each model bathymetry figure. Different orientations in figures b-f are due to different coordinate systems used in each model.	79
Figure 30.	Vertical section of the long-term mean northward velocity (cm/s) across Bering Strait from all models. Positive velocity is northward. A black X marks the approximate location of the A2 mooring within each model domain.	88
Figure 31.	Monthly mean velocity at ~10 above the bottom from the A2 mooring location (upper) and A3 mooring location (lower). Model results are	

	shown in color and the observations are shown in black. Mean values for the time period when data are available are shown on the far right.	91
Figure 32.	Monthly mean near-bottom temperature ($^{\circ}\text{C}$) at the (a) A2 and (b) A3 mooring locations. Model results are shown in various colors and observations are shown in black. Mean values for the time period when data are available are shown on the far right.	95
Figure 33.	Monthly mean near-bottom salinity at the (a) A2 and (b) A3 mooring locations. Model results are shown in various colors and observations are shown in black. Mean values for the time period when data are available are shown on the far right.	96
Figure 34.	Monthly mean volume transport from the models and observations. The observations are based on the near-bottom velocity at the A3 mooring location multiplied by a cross-sectional area of 4.25 km^2 , as per Woodgate et al. (2010). Mean values for the time period when data are available are shown on the far right.	98
Figure 35.	Annual mean (a) volume transport, (b) heat, and (c) freshwater fluxes. Heat is referenced to -1.9°C for NAME, ECCO2, and ORCA, in order to compare with cited observations in the text. Heat is referenced to -1.8°C for PIOMAS and BESTMAS, due to model limitations. Freshwater is referenced to 34.8 psu. Observed volume transport and freshwater flux values do not include the ACC and stratification, which likely add $\sim 0.1 \text{ Sv}$ and $800\text{--}1,000 \text{ km}^3/\text{yr}$ (see Woodgate et al. 2006). The dashed black line (c) represents the freshwater flux with the estimated ACC and stratification correction of an additional $900 \text{ km}^3/\text{yr}$. The observed heat flux values include an estimate for the ACC using SST for a 10-m surface layer (lower bound; lower black line) and a 20-m surface layer (upper bound; upper black line). Observed heat flux values are described further in Woodgate et al. (2010).....	99
Figure 36.	Annual cycles of (a) volume transport, (b) heat flux, and (c) freshwater transport. The annual cycles are averaged over 1991–2004, except for ORCA (1991–2001) and ECCO2 (1992–2004). The heat flux is referenced to -1.9°C for NAME, ECCO2, and ORCA. The reference temperature is -1.8°C for PIOMAS and BESTMAS due to model limitations. The freshwater transport is referenced to 34.8 psu.	103
Figure 37.	Monthly mean volume transport anomalies from the annual cycle (Sv). The annual cycle for each model and the data are shown in Figure 36a.	105
Figure 38.	Bering Strait velocity (cm/s) from the (a) 9-km model during the 26-year mean March and (b) 2-km model during spin-up mean March.	108
Figure 39.	Monthly mean (upper) and (lower) 13-month running mean values of the AO, PDO, and PNA.	111

LIST OF TABLES

Table 1.	26-year-mean fluxes across Aleutian Island cross-sections. Net volume flux (Net Vol.) is given in Sv, with the standard deviation shown below each value of net volume flux. Positive (northward) volume flux (Pos. Vol.) and negative (southward) volume flux (Neg. Vol.) values are also shown. The heat and freshwater flux values are shown in the same way. Heat flux values are given in TW, and freshwater flux values are given in mSv ($10^3 \text{ m}^3/\text{s}$). The locations of the sections are shown in Figure 3.	17
Table 2.	Comparison of observed and modeled net volume transport values (Sv) for Buldir Pass, Near Strait, and Kamchatka Pass. Values for Buldir Pass and Near Strait are northward and values for Kamchatka Pass are southward. Model values are the mean of 26 years (1979–2004). Observed values are for time periods shown in parenthesis.	19
Table 3.	26-yr mean volume transport (Sv), salt flux (million kg/s), freshwater flux (mSv; relative to 34.8), and heat transport (TW; relative to -0.1°C). Numbers in parenthesis represent standard deviation.....	44
Table 4.	Net heat transport (TW) across various locations in the Bering Sea.	48
Table 5.	Correlation coefficients for volume transport, heat flux, and section mean temperature between Bering Slope Current sections. The number in parenthesis is the lag time in months. The first column (Mo. Mean) for each parameter is the correlation for the monthly mean values. The second column (Annual Cycle Removed) is the correlation after removing the annual cycle. All correlations are significant at the 95% level except for those marked with a *.	53
Table 6.	Twenty-six-year mean (1979–2004) volume transport (Sv), salt flux (million kg/s), freshwater flux (mSv; relative to 34.8), and heat transport (TW; relative to -0.1°C) for canyon sections. Numbers in parenthesis represent standard deviation.	55
Table 7.	Basin information on the five models used in this study.	80
Table 8.	Cross-sectional area across Bering Strait for the models and observations and friction coefficients for the models.	89
Table 9.	Mean velocity, volume transport, near-bottom temperature, and near-bottom salinity from the models and from observations, for the time period when observations are available, as shown in Figures 31–34. However, the values from ECOO2 are for 1992–2004 only and the values from ORCA are for 1990–2001 only. Error estimates are shown in parenthesis. All model errors are calculated as the standard error of the mean (sample standard deviation divided by the square root of the sample size).	92
Table 10.	Long-term mean velocity, volume transport, near-bottom temperature, and near-bottom salinity from the models, for the time periods shown in Figures 31–34. Error estimates are shown in parenthesis.....	93

Table 11.	Correlation coefficients between models and the observations of northward velocity, temperature, and salinity at A2 and A3 locations. All correlations are significant at the 95% level.	93
Table 12.	Depth information (m) for the models and the observations at the A2 and A3 mooring locations.....	97
Table 13.	Correlation coefficients between the mean temperature across BSC sections and large-scale weather indices. Correlations are for the 13-month running mean values of both the temperature time series and the weather indices for 1979–2004. Correlations with no lag are shown (Corr. no lag) with the associated p-value. The maximum correlation (Max. Corr.) is also shown for a lag range of +/- 50 months, along with the lag time and p-value. A negative lag means that the mean temperature across the BSC section is leading the weather index. The significance level used is 95%.....	112
Table 14.	Correlation coefficients between the net volume transport through Bering Sea cross-sections and large-scale weather indices. Correlations are for the 13-month running mean values of both the volume transport time series and the weather indices for 1979–2004. Correlations with no lag are shown (Corr. no lag) with the associated p-value. The maximum correlation (Max. Corr.) is also shown for a lag range of +/- 50 months, along with the lag time and p-value. A negative lag means that the volume transport through the cross-section is leading the weather index.	114

LIST OF ACRONYMS AND ABBREVIATIONS

ACC	Alaska Coastal Current
ADCP	Acoustic Doppler Current Profiler
ANSC	Aleutian North Slope Current
ARDB	Arctic Runoff Data Base
AO	Arctic Oscillation
BESTMAS	Bering Ecosystem Study ice-ocean Modeling and Assimilation System
BSC	Bering Slope Current
CTD	Conductivity Temperature Depth
ECCO2	Estimating the Circulation and Climate of the Ocean, Phase II
ECMWF	European Centre for Medium-Range Weather Forecasts
EEZ	Exclusive Economic Zone
EKE	Eddy Kinetic Energy
ENSO	El Niño/Southern Oscillation
ETOPO2	Earth Topography Five Minute Gridded Elevation Data Set
ETOPO5	Earth Topography Two Minute Gridded Elevation Data Set
GEBCO	General Bathymetric Charts of the Oceans
IBCAO	International Bathymetric Chart of the Arctic Ocean
JRA25	Japanese 25-year reanalysis
MITgcm	Massachusetts Institute of Technology general circulation model
NAM	Northern Hemisphere Annular Mode
NAME	Naval Postgraduate School Arctic Modeling Effort
NCAR	National Center for Atmospheric Research

NCEP	National Centers for Environmental Prediction
NEMO	Nucleus for European Modelling of the Ocean
PDO	Pacific Decadal Oscillation
POP	Parallel Ocean Program
POIM	Parallel Ocean and sea Ice Model
PIOMAS	Pan-Arctic Ice-Ocean Modeling and Assimilation System
PHC	Polar Science Center Hydrographic Climatology
PNA	Pacific/North American Teleconnection Pattern
S	Salinity
SSH	Sea Surface Height
SSHA	Sea Surface Height Anomaly
SST	Sea Surface Temperature
TKE	Total Kinetic Energy

ACKNOWLEDGMENTS

I would like to thank my advisor, Dr. Wieslaw Maslowski, for giving me the opportunity to pursue this degree and for his continued guidance and advice throughout the process. I also thank my committee members, Drs. John Walsh, Mary Batteen, Peter Guest, and Robin Tokmakian for helpful comments and insight, which improved an earlier version of this dissertation.

This research was financially supported by the U.S. National Science Foundation, the U.S. Department of Energy Climate Change Prediction Program, the National Aeronautics and Space Administration Ocean and Ice Program, and the Office of Naval Research. Computer resources were provided by the Arctic Region Supercomputing Center (ARSC) through the U.S. Department of Defense High Performance Computer Modernization Program (HPCMP) Grand Challenge Project.

I would like to thank several people who contributed expertise, data, and/or model results including: Jaromir Jakacki, Steve Okkonen, Robert Osinski, Waldemar Walczowski, Andrew Roberts, Jacqueline Grebmeier, Lee Cooper, Yvegeny Aksenov, Beverly de Cuevas, An Nguyen, Mike Steele, Rebecca Woodgate, and Jinlun Zhang.

I am grateful for my family and friends, who have continued to support and encourage me throughout the years. Special thanks goes to my husband, Travis, for his love, patience, and motivation.

THIS PAGE INTENTIONALLY LEFT BLANK

I. INTRODUCTION

A. GEOGRAPHY OF THE BERING SEA

The Bering Sea is a high-latitude, semi-enclosed, marginal sea, which links the North Pacific Ocean and the Arctic Ocean (Figure 1). To the south, the Bering Sea is separated from the North Pacific Ocean by the Aleutian Island Arc, a chain of volcanically-formed small islands and passages. The Bering Sea is composed of approximately equal areas of continental shelf and deep basin. The deep basin makes up the southwestern part of the Bering Sea and has a maximum depth of ~4,000 m. Two submarine features (Shirshov Ridge and Bowers Ridge) create three sub-basins within the deep Bering Sea: Aleutian (the largest), Kamchatka, and Bowers basins. The Bering Sea slope is ~1300 km in length and runs from the easternmost Aleutian Islands to just south of Cape Navarin, Siberia.

The northeastern portion of the Bering Sea is continental shelf, which is extensive in the east (>500 km) and narrows to the west (<100 km). Most of the Bering Sea shelf is <100 m deep, and the shelf break occurs at ~170m deep (Okkonen 1996). Three straits are located on the northern Bering Sea shelf: Anadyr Strait (between Siberia and St. Lawrence Island), Shpanberg Strait (between St. Lawrence Island and Alaska), and Bering Strait (between Siberia and Alaska). The Bering Strait is the northernmost border of the Bering Sea and is the only Pacific connection to the Arctic Ocean.

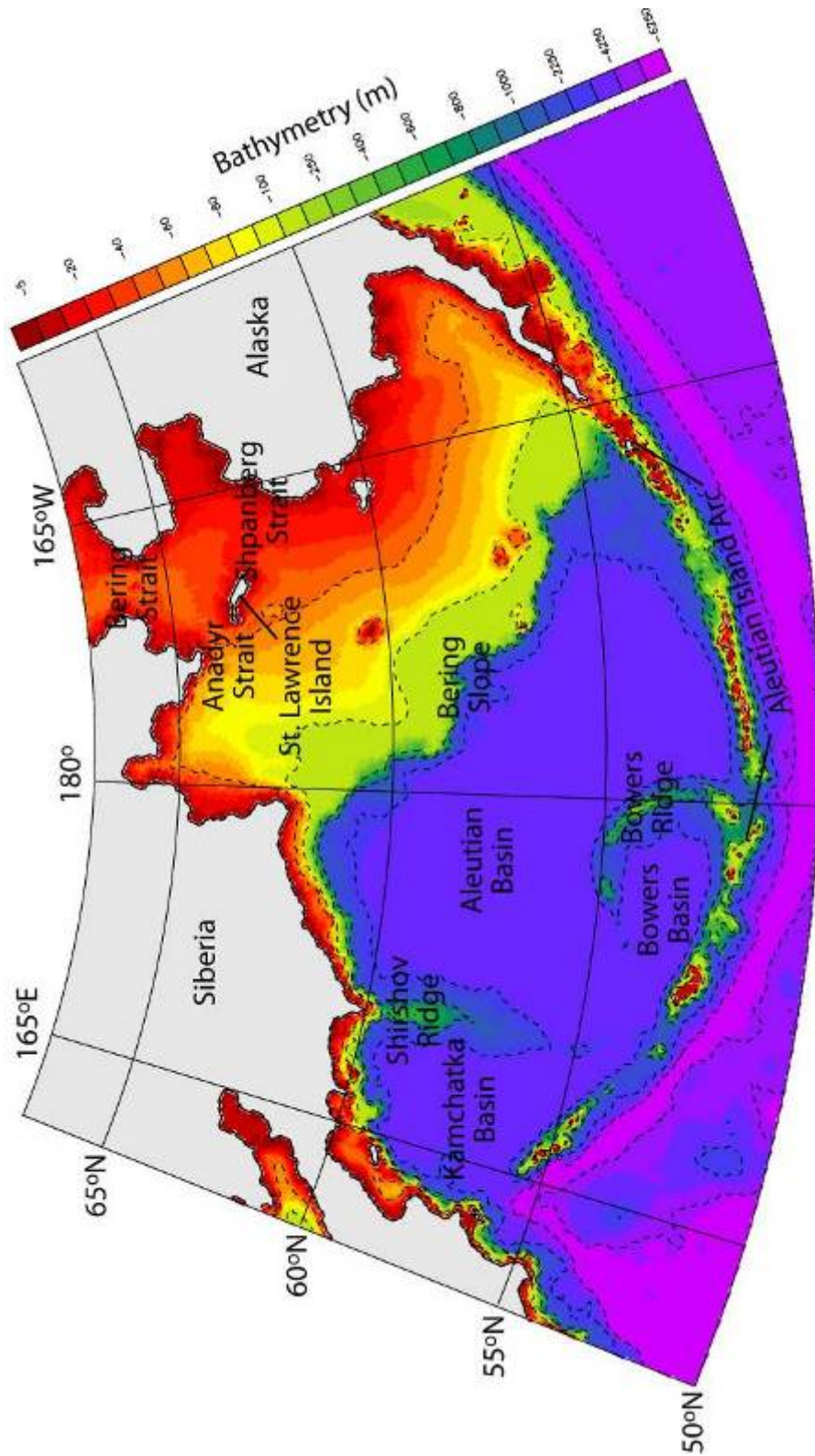


Figure 1. Model bathymetry (m) and geography of the Bering Sea.

B. MAJOR FEATURES OF THE BERING SEA

The Bering Sea, like many subpolar seas, is characterized by seasonal extremes in solar radiation, meteorological forcing, and ice cover (Stabeno et al. 1999). The primary storm track in the North Pacific is along the Aleutian Island Arc, which forms the statistical feature known as the Aleutian Low (Overland 1981; Overland and Pease 1982). During summer, the Aleutian Low is usually weak and weather is mild, due to the long periods of daylight and high insolation. Significant changes occur in atmospheric pressure fields during winter, with a strengthened Siberian High and an intensified Aleutian Low. This results in strong, very cold winds from the northeast and an increase in the frequency and intensity of storms.

Portions of the shelf and coastal region experience seasonal sea ice cover for approximately nine months per year (October–June), with ice reaching the shelf break in late winter of some years, although satellite observations indicate a decrease in the extent of sea ice and a lengthening of the ice-free period since 1979 (Frey et al. 2011). Maximum ice extent tends to occur in March, with little to no ice present from July–September. Active polynya regions include the St. Lawrence Island Polynya (just south of the island), as well as coastal areas just south of the Siberian Peninsula and Seward Peninsula (Schumacher et al. 1983). Intense ice formation in these areas leads to salinization of the water column and the erosion of the thermocline (Schumacher et al. 1983). Most of the sea ice in the Bering Sea is formed *in situ*, with very little moving southward through Bering Strait (Tabata 1974; Muench and Ahlnäs 1976). Large-scale ice motion (predominately southward) is driven primarily by regional wind forcing, except in local areas where currents may be strong enough to oppose the wind (Muench and Ahlnäs 1976). Pease (1980) described the sea ice process in the Bering Sea as a “conveyor belt” system, where ice growth occurs primarily in the north, ice is advected southward due to wind stress, and ice melt occurs at the thermodynamic limit. Subsequently, as meltwater cools the upper layer, the sea ice extent is allowed to advance farther south.

Major circulation features include the Alaskan Stream, a westward-flowing current located just south of the Aleutian Island Arc. The stream provides the inflow into the Bering Sea via the Aleutian Island Passes (Favorite 1974). The Bering Slope Current flows along the northeastern boundary of the Aleutian Basin above the continental slope (Kinder et al. 1975), although more recent observations (e.g., Okkonen 1993) and model results presented herein indicate that this current may be more a system of eddies rather than a continuous feature. The Anadyr Current is located in the northwestern Bering Sea and flows along the western boundary, generally toward Bering Strait. The Alaska Coastal Current (ACC) is a narrow (order of ten km; Woodgate and Aagaard 2005), buoyancy-driven current which originates south of the Aleutian Islands, flows through Unimak pass and other eastern passes, and continues northward along the Alaskan coast. Observational results indicate that the presence of the ACC may be seasonal at Bering Strait (Paquette and Bourke 1974; Ahlnäs and Garrison 1984; Woodgate and Aagaard 2005).

C. SIGNIFICANCE OF THE BERING SEA

The Bering Sea shelf is a highly productive region of the world ocean (e.g., Grebmeier et al. 1988 and references therein). Many species of fish, shellfish, seabirds, and marine mammals are sustained by large populations of the lower trophic levels (e.g., phytoplankton and zooplankton). The northern Bering Sea supports a historically abundant benthic population of large clams and polychaetes. These benthic organisms support populations of Pacific walrus, diving sea ducks, and grey whales. However, recent declines in these benthic populations may be affecting the higher trophic organisms (Grebmeier and Dunton 2000; Grebmeier et al. 2006), some of which are believed to have critically small populations.

Almost half of the total U.S. annual catch of commercial fish and shellfish comes from Alaskan waters (Macklin et al. 2002; Sigler et al. 2010), primarily in the southeast Bering Sea. Important commercial species include pollock, salmon, halibut and crab. Because this region is an important national and international fishery, much fisheries research has been conducted in some parts of the Bering Sea (e.g., Busby et al. 2005;

Ciannelli and Bailey 2005; Mueter et al., 2006). For example, Sigler et al. (2010) note that walleye pollock experienced low recruitment during the “warm” years of 2001–2005, possibly due to very low abundance of their main prey (zooplankton). The pollock fishery, which had a wholesale value of \$1.4 billion in 2008 in the U.S., was subsequently affected by decreased commercial catches (Sigler et al. 2010). Mechanisms for the climate-related changes are still not completely clear and are currently being investigated. In general, there is a need for more understanding of the physical processes that control environmental conditions for these organisms. This knowledge is important not only for scientific understanding, but also for people who rely directly on the Bering Sea for food and employment. Limited observations exist for the Bering Sea, as compared to temperate waters, and even less work has been done in other marine science fields, particularly in numerical modeling. Model results presented herein will advance understanding of important physical processes in the Bering Sea.

THIS PAGE INTENTIONALLY LEFT BLANK

II. MODEL DESCRIPTION

Early models of the Bering Sea were two-dimensional and barotropic (e.g., Overland and Roach 1987; Spaulding et al. 1987). These models were able to represent important features of the northern Bering Sea circulation. Overland and Roach (1987) showed that the large-scale (Pacific-Arctic) pressure gradient was responsible for driving the background northward flow through Bering Strait. However, their ability to represent baroclinic flow and shelf-basin exchange was restricted. More recent work in the Bering Sea includes that of Overland et al. (1994). They used a primitive equation, three-layer hydrodynamic model at $1/8^\circ$ horizontal resolution. However, the domain did not include the shelf and slope, but was instead limited to the Bering Sea basin only. Mizobata et al. (2006) used a numerical model based on the Princeton Ocean Model (Blumberg and Mellor 1987) to simulate the eddy field in the vicinity of Zhemchug Canyon. While this model has a high horizontal resolution (5 km), the domain covers only a fraction of the Bering Sea slope and results may be significantly influenced by the prescribed lateral boundary forcing. The following analyses utilize results from a numerical model with a pan-Arctic domain that includes the entire deep basin, slope and shelf of the Bering Sea, as well as the North Pacific Ocean southward to $\sim 30^\circ\text{S}$.

This model was developed by the Naval Postgraduate School Arctic Modeling Effort (NAME; <http://www.oc.nps.edu/NAME/name.html>). The model is configured on a $1/12^\circ$ rotated spherical coordinate grid (Arakawa B grid; Mesinger and Arakawa 1976). The coupled sea ice–ocean model has 45 z -coordinate vertical depth layers with eight levels in the upper 50 m and fifteen levels in the upper 200 m (Figure 2). The high vertical resolution, especially in the upper water column, allows for more realistic representation of the shallow Arctic and sub-Arctic shelves. The ~ 9 -km horizontal model grid permits calculation of flow through the narrow straits of the northern and southern Bering Sea and permits eddies with diameters as small as 36 km, however, the smallest eddies are likely not resolved (Maslowski et al. 2008b). According to Chelton et al.

(1998), the typical Rossby radius of deformation range is ~12–20 km in the Bering Sea. Thus, fully eddy-resolving models of the Bering Sea require a grid cell size of order few kilometers.

The model domain contains the sub-Arctic North Pacific (including the Sea of Japan and the Sea of Okhotsk) and North Atlantic Oceans, the Arctic Ocean, the Canadian Arctic Archipelago and the Nordic Seas (Figure 2). The region of interest, the Bering Sea, is therefore far away from the artificially closed lateral boundaries in the North Pacific at 30°N, greatly reducing the potential effect of boundary conditions. In an effort to balance the net flow of Pacific Ocean water into the Arctic Ocean, a U-shaped 500-m deep, 162-km (18 grid point) wide channel was created through North America connecting the Atlantic Ocean to the Pacific Ocean. A westward wind forcing of $1.75 \text{ dyne cm}^{-2}$ is prescribed along the channel. Flow through the Bering Strait and the channel is predicted in the model at each time step. Model bathymetry is derived from two primary sources: ETOPO5 at five-minute resolution for the region south of 64°N and International Bathymetric Chart of the Arctic Ocean (Jakobsson et al. 2000) at 2.5-km resolution for the region north of 64°N.

The regional ocean model adapts the Los Alamos National Laboratory Parallel Ocean Program model (POP; Dukowicz and Smith 1994). The combination of the free surface and high resolution allows the use of unsmoothed, very realistic bathymetry. This is important for representing steep bathymetry, such as continental slopes. Yukon (and other Arctic) river runoff is included in the model as a virtual freshwater flux at the river mouth using the observed daily-averaged annual cycle of each river's discharge. In the Gulf of Alaska the freshwater flux from runoff (Royer 1981) is introduced by restoring the surface ocean level (of 5 m) to climatological (Polar Science Center Hydrographic Climatology; PHC; Steele et al., 2001) monthly mean temperature and salinity values over a monthly time scale (as a correction term to the explicitly calculated fluxes between the ocean and overlying atmosphere or sea ice). This approach was used in part due to the lack of realistic discharge observations for the many small rivers, which empty into the Gulf of Alaska, as well as a lack of domain-wide and time-varying

precipitation/evaporation data. A 4°-wide band of ocean points along the domain boundary is restored to annual average PHC temperature and salinity climatology on a ten-day timescale.

The sea ice model uses viscous plastic ice rheology (Zhang et al. 1999; Zhang and Hibler 1997) and the zero-layer approximation for heat conduction through ice after Semtner (1976). The surface heat budget follows Parkinson and Washington (1979). The sea ice model was initialized on January 1, 1979 with a 2-m-thick slab of ice placed over all grid cells with sea surface temperatures $< 0.0^{\circ}\text{C}$.

The ocean model was initialized with climatological, three-dimensional temperature and salinity fields (PHC) and integrated for 48 years in a spin-up mode. During the spin-up, daily averaged annual climatological atmospheric forcing derived from 1979 to 1993 reanalysis from the European Centre for Medium-Range Weather Forecasts (ECMWF) was used for 27 years. The spin-up was continued using repeated 1979 ECMWF annual cycle for six years and then 1979–1981 interannual fields for the last 15 years of spinup. This approach is especially important in establishing realistic ocean circulation representative of the time period at the beginning of the actual interannual integration. At the same time, the spin-up procedure was designed to force the model into a quasi-equilibrium state that is minimally sensitive to the specific initial conditions. The ocean time step is 480 s and the ice model time step is 48 min. The ECMWF atmospheric forcing fields include: 10-m east-west and north-south (u and v) wind velocity components, surface pressure, temperature and dew point, and incoming longwave and shortwave radiation. The final run with realistic daily averaged ECMWF interannual forcing starts in 1979 and continues through 2004. Results from this integration (26 years) are used for the following analyses.

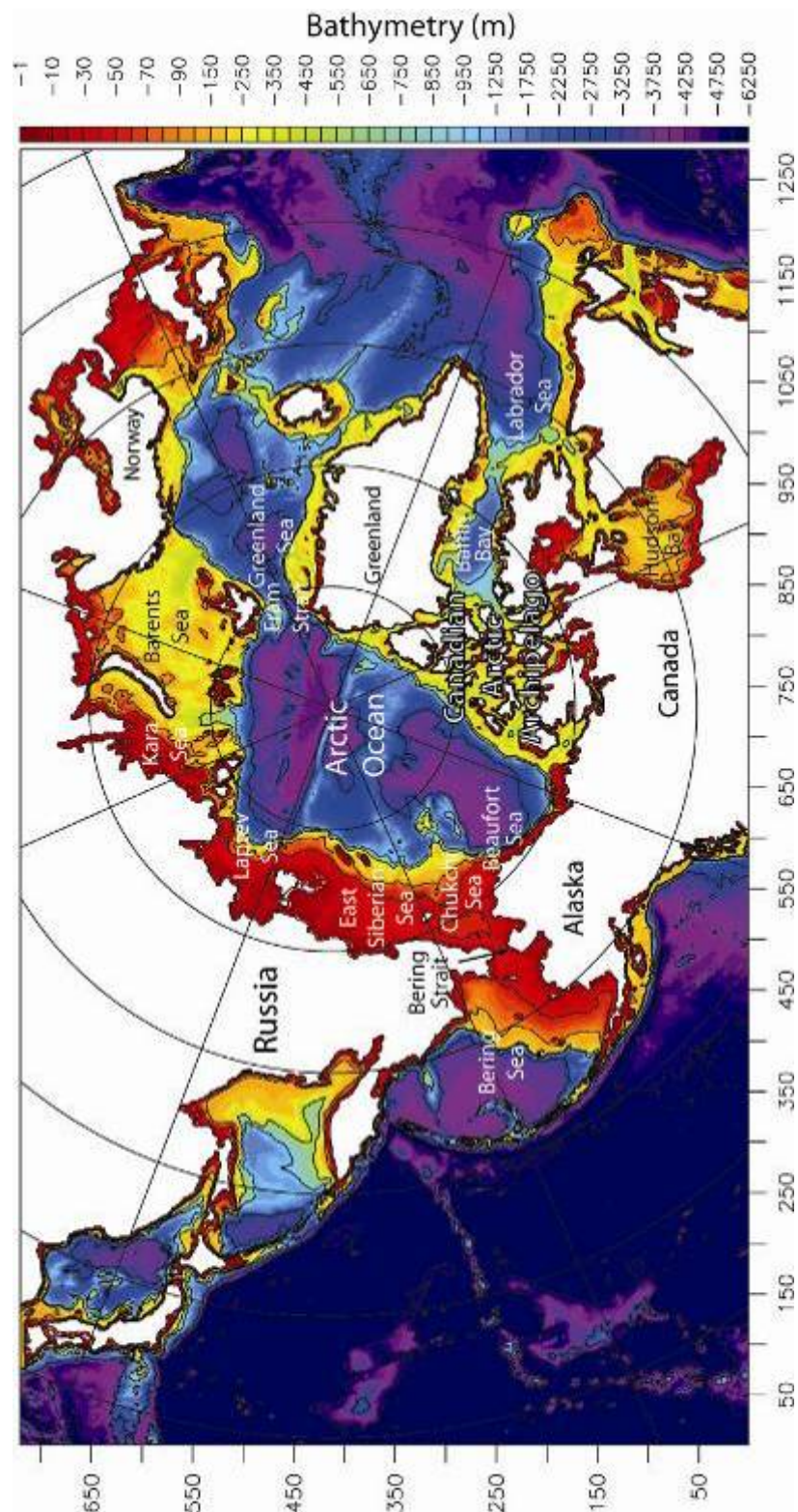


Figure 2. 1/12° ice-ocean model domain and bathymetry (m).

III. ORGANIZATION OF THE DISSERTATION

The following four chapters are organized geographically, beginning at the southern boundary of the Bering Sea, with Chapter IV on the communication between the deep Bering Sea and the Western Subarctic Gyre, as well as the circulation and mesoscale activity within this region. Chapter V is focused on the shelf-basin exchange and outer shelf dynamics. In Chapter VI, the circulation and energetics are examined across the northern Bering Sea shelf. The flow and property exchange through the northern boundary of the Bering Sea (Bering Strait) are intercompared from observations and multiple model results in Chapter VII. Chapter VIII shows the linkages of the Bering Sea modeled circulation with large-scale weather indices, as well as the physical impacts on biological processes, and the downstream effects of Bering Sea processes. The overall conclusions are discussed in Chapter IX. Finally, some suggestions for future research are presented in Chapter X.

THIS PAGE INTENTIONALLY LEFT BLANK

IV. THE DEEP BERING SEA AND WESTERN SUBARCTIC GYRE COMMUNICATION

A. INTRODUCTION

The deep Bering Sea basin is bordered by the Aleutian Island Arc to the south, by the Bering Sea slope to the northeast, and by the Kamchatka Peninsula to the northwest. Depths greater than 3000 m are found throughout the basin, except in the vicinity of two large submarine features: Bowers Ridge (north of Amchitka Pass) and Shirshov Ridge, which extends southward from Kamchatka Peninsula. The model bathymetry of the deep Bering Sea, along with a series of cross sections to be discussed in the following section is shown in Figure 3. The general circulation of the Bering Sea basin is typically described as cyclonic in the long-term mean. However, transport within the gyre can vary by more than 50% (Stabeno et al. 1999). Causes associated with this variation have been identified as either changes in the Alaskan Stream inflow (Overland et al. 1994) and/or variability of the wind-driven transport within the basin (Bond et al. 1994). The low-frequency variations in the wind stress curl account for ~ 1.5 Sv of the variability in the transport within the deep Bering Sea basin (Bond et al. 1994); however, the majority of the variability is due to variations in the curl on daily to monthly timescales.

This chapter includes discussion of the general circulation within the Bering Sea basin and along the Aleutian Islands from the long-term model mean results. In addition, volume and property flux values across Aleutian Island Passes are shown and compared to available observations. Finally, the mesoscale meanders and eddies within the basin and along the Alaskan Stream are discussed and validated with limited observations.

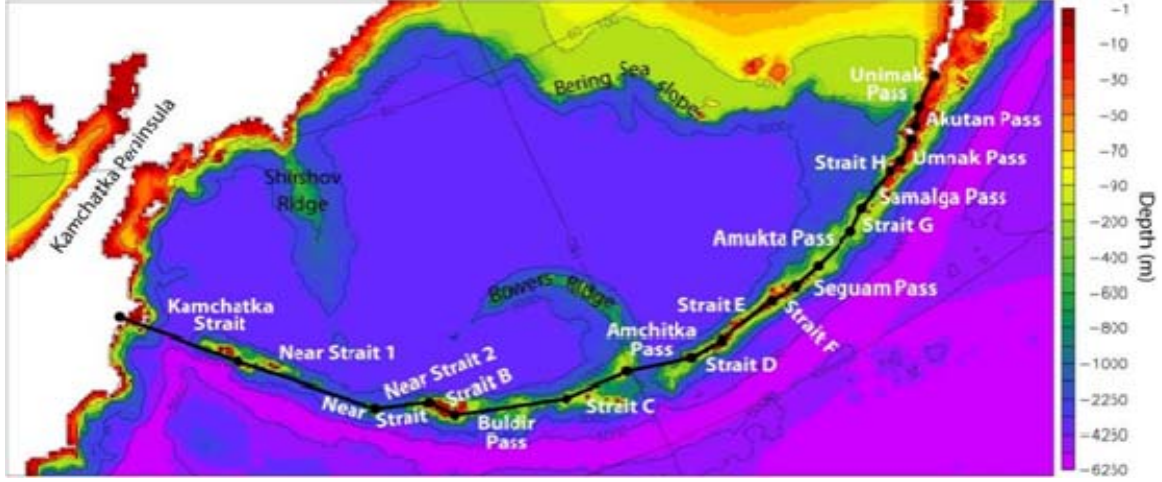


Figure 3. Model bathymetry (m) of the deep Bering Sea. Black lines indicate the locations of cross-sections and white text indicates the names of these cross-sections.

B. GENERAL CIRCULATION

The Alaskan Stream flows primarily westward just south of the Aleutian Island Arc (Figure 4). This current is a major feature of the northern North Pacific, as indicated by the high values of total kinetic energy (TKE) in Figure 4. TKE is calculated as:

$$TKE = \frac{(u^2 + v^2)}{2} \quad (1)$$

with u and v representing the x- and y-components of velocity. TKE is useful for determining the relative speed of a current. The Alaskan Stream has a significant effect on the flow and property flux through the Aleutian Passes and, therefore, on the Bering Sea. The mean modeled volume transport is between 34 and 44 Sv, with intensification occurring downstream (Maslowski et al. 2008a).

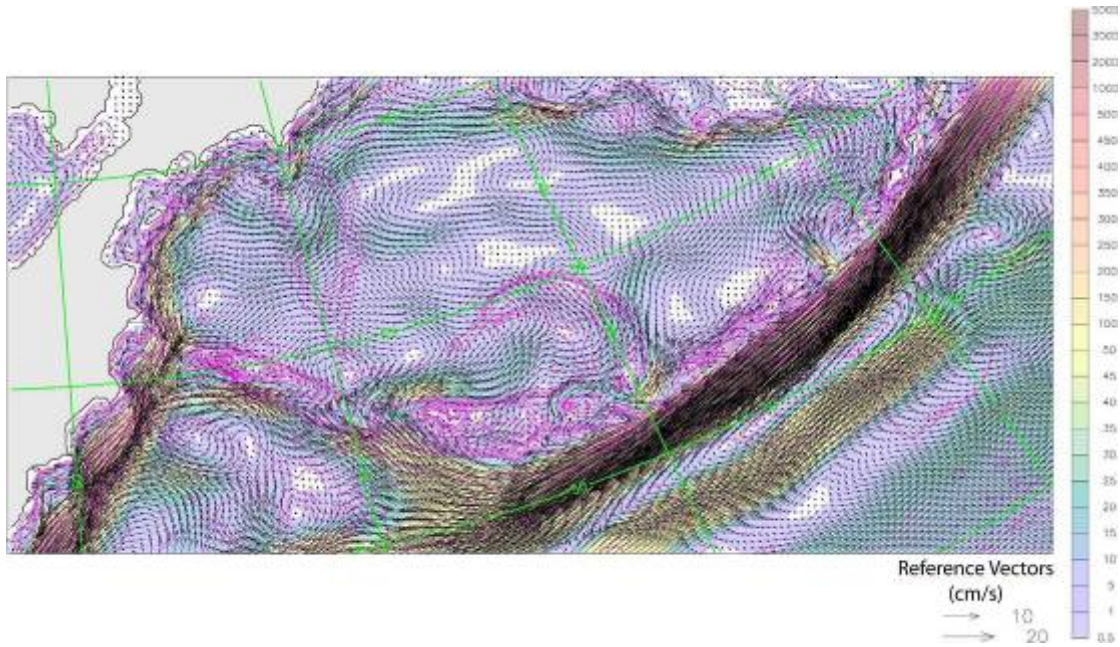


Figure 4. The 26-year mean (1979–2004) upper 100 m circulation (vectors) and total kinetic energy (shading). Magenta contour lines represent bathymetry (m). Every second vector is shown. The direction of the Alaskan Stream is westward.

Communication between the Bering Sea and the North Pacific (primarily the Alaskan Stream) occurs through several passes along the Aleutian Islands. Inflow through these passes contributes to the eastward-flowing Aleutian North Slope Current (ANSC; Figure 4), which is located north of the Aleutian Islands. The ANSC is partially deflected by the bathymetry of Bowers Ridge and flow through Amchitka and Amukta passes. These are areas with relatively strong northward inflow, which tends to push the ANSC northward. The generally eastward flow of the ANSC begins to turn northwestward between 177–167°W, forming the Bering Slope Current (BSC). The BSC extends from the eastern Aleutian Islands along the shelf-break toward the coast of Russia. Long-term mean volume transport was estimated to be ~2–3.5 Sv (Clement Kinney et al. 2009), however the BSC is more a system of eddies, rather than a continuous current (Okkonen 1993; Clement Kinney et al. 2009). A major portion of the BSC separates from the slope around 180°, and gradually turns southwestward. The shallower portion is bathymetrically steered southwestward along the Siberian coast

within the 500-m isobath, forming the Kamchatka Current. West of Shirshov Ridge, these two merge and flow primarily southward into the North Pacific Ocean. These general circulation features compare favorably with available observations published by Stabeno and Reed (1994), Verkhunov and Tkachenoko (1992), Reed et al. (1993), and Cokelet et al., (1996).

C. VOLUME AND PROPERTY FLUX ACROSS THE ALEUTIAN ISLAND PASSES

According to Stabeno et al. (1999), volume transport into the Bering Sea is highly variable on time scales of weeks to years. Inflow from the North Pacific into the Bering Sea occurs primarily through Near Strait, Buldir Pass, Amchitka Pass, and Amukta Pass (Stabeno and Reed 1993). Outflow from the Bering Sea into the North Pacific occurs largely through Kamchatka Pass (Stabeno and Reed 1993). Table 1 shows the model results of 26-year-mean (1979–2004) volume, heat, freshwater, and salt flux across each pass or strait shown in Figure 3. Heat flux is referenced to the freezing temperature (based on salinity) and freshwater flux is referenced to 33.8. Some passes were labeled alphabetically because they either did not have a recognized geographic place name or were artifacts of the 9-km grid cell spacing. The smallest islands were not resolved by the model bathymetry and at times created very shallow passes that are not present in reality. These alphabetically-labeled artificial passes had very low mean volume transport values, with most $< \pm 0.006$ Sv (the value at Strait C is -0.136 Sv). Model results have previously been compared with observations in Amuka Pass and Amchitka Pass (Maslowski et al. unpublished). Other passes in the central and eastern Aleutians also tend to have net northward flow, however they are much shallower and narrower, which means that they contribute little to the overall volume and property flux (Table 1). Therefore, this chapter will focus on the larger and deeper western passes including: Buldir Pass, Near Strait, and Kamchatka Strait.

Table 1. 26-year-mean fluxes across Aleutian Island cross-sections. Net volume flux (Net Vol.) is given in Sv, with the standard deviation shown below each value of net volume flux. Positive (northward) volume flux (Pos. Vol.) and negative (southward) volume flux (Neg. Vol.) values are also shown. The heat and freshwater flux values are shown in the same way. Heat flux values are given in TW, and freshwater flux values are given in mSv ($10^3 \text{ m}^3/\text{s}$). The locations of the sections are shown in Figure 3.

Pass/Strait	Net Vol. /s.d.	Pos. Vol. /Neg. Vol.	Net Heat /s.d.	Pos. Heat /Neg. Heat	Net FW /s.d.	Pos. FW /Neg. FW
Unimak	0.069 0.078	0.096 -0.026	1.933 2.406	2.968 -1.035	4.110 4.570	5.492 -1.381
Akutan	-0.001 0.025	0.011 -0.012	-0.209 0.890	0.305 -0.514	-0.013 1.368	0.589 -0.601
Umnak	0.003 0.024	0.015 -0.012	-0.026 0.856	0.485 -0.510	0.195 1.296	0.797 -0.603
Strait H	0.002 0.003	0.003 -0.002	0.058 0.112	0.124 -0.065	0.083 0.156	0.161 -0.078
Samalga	0.041 0.090	0.344 -0.303	1.085 3.013	10.760 -9.674	2.355 4.653	15.145 -12.790
Strait G	0.040 0.100	0.116 -0.077	1.131 3.156	3.721 -2.590	2.111 5.256	6.067 -3.956
Amukta	1.601 0.842	1.753 -0.152	50.378 25.783	55.408 -5.030	64.783 31.020	71.284 -6.501
Seguam	0.026 0.059	0.102 -0.076	0.724 2.171	3.441 -2.717	1.375 2.975	4.767 -3.392
Strait F	0.006 0.024	0.029 -0.023	0.121 0.854	0.983 -0.862	0.306 1.100	1.315 -1.009
Strait E	-0.004 0.071	0.058 -0.062	-0.426 2.516	1.944 -2.370	-0.002 3.214	2.659 -2.661
Strait D	-0.006 0.054	0.046 -0.053	-0.367 1.917	1.579 -1.946	-0.196 2.471	2.117 -2.313
Amchitka	1.890 2.299	2.962 -1.072	58.580 64.668	87.697 -29.117	50.394 32.053	63.806 -13.412
Strait C	-0.136 0.757	0.464 -0.600	-4.194 23.156	14.344 -18.537	-2.881 18.225	12.410 -15.291
Buldir Pass	1.216 1.566	2.178 -0.962	36.673 47.016	66.280 -29.607	22.635 29.406	45.088 -22.453
Strait B	-0.003 0.019	0.009 -0.012	-0.081 0.604	0.302 -0.383	-0.092 0.732	0.332 -0.424
Near Strait 1	2.520 4.418	3.806 -1.286	70.282 123.340	106.062 -35.780	22.686 49.537	39.576 -16.890

Pass/Strait	Net Vol. /s.d.	Pos. Vol. /Neg. Vol.	Net Heat /s.d.	Pos. Heat /Neg. Heat	Net FW /s.d.	Pos. FW /Neg. FW
Near Strait	2.537	9.283	66.455	238.023	15.180	70.384
2	6.607	-6.746	170.506	-171.568	54.676	-55.205
Near Strait	5.057	13.089	136.737	344.085	37.866	109.961
(total)	5.384	-8.032	137.200	-207.348	48.680	-72.095
Kamchatka	-8.903	2.983	-195.267	59.597	-116.494	13.729
	4.849	-11.886	107.142	-254.864	37.752	-130.223

1. Comparison of Observed and Modeled Volume Transports

Multi-year continuous observations of the flow through the western passes are not available. Available observations include satellite-tracked drifters and short-term CTD measurements. Observations of the inflow through Buldir Pass were ~1 Sv during September 1992 (Stabeno and Reed 1993), based on CTD measurements (see Table 2 for a comparison of modeled and observed volume transport values). The model results show a long-term mean of 1.2 Sv [standard deviation (S.D.) = 1.566] net northward flow through Buldir Pass and show that September is the minimum of the annual cycle. Therefore, the observed value during September 1992 may be an underestimate of the long-term mean.

Table 2. Comparison of observed and modeled net volume transport values (Sv) for Buldir Pass, Near Strait, and Kamchatka Pass. Values for Buldir Pass and Near Strait are northward and values for Kamchatka Pass are southward. Model values are the mean of 26 years (1979–2004). Observed values are for time periods shown in parenthesis.

Observation/Model	Buldir Pass	Near Strait	Kamchatka Pass
NAME Model	1.2 (net), 2.2 (northward), -1.0 (southward)	5.1 (net), 13.1 (northward), -8.0 (southward)	-8.9 (net), 3.0 (northward), -11.9 (southward)
Stabeno and Reed (1993)	~1 (Sept. 1992)		
Favorite (1974)		10 (1955–1974, discontinuous)	
Reed and Stabeno (1993)		~5 (Sept. 1992)	
Stabeno and Reed (1992)		~ 3 (Aug. 1991)	-6.8 (Aug. 1991)
Verkhunov and Tkachenko (1992)			~ -11 (Oct.–Nov. 1990) -6 to -7 (Apr –May 1990)
Panteleev et al. (2006)			-24 (1932–2004, discontinuous)

Early observations of the northward flow through Near Strait range from 3.7 to 26 Sv (Arsen’ev 1967; Ohtani 1970; Hughes et al. 1974). Favorite (1974) concluded that a total of 10 Sv was a typical value. However, the methods behind all of these observations cannot be considered precise. More recently, Reed and Stabeno (1993) collected observations of volume flux through Near Strait during September 1992. Based on CTD casts, they found ~5 Sv of Alaskan Stream inflow through Near Strait. This compares

well with the 26-year mean modeled net inflow of 5.057 Sv (a combination of the flow through sections labeled Near Strait 1 and Near Strait 2; S.D. = 5.4; Table 1; Figure 3). Based on satellite-tracked drifters released throughout the region, Stabeno and Reed (1992) noted an anomalous lack of inflow through Near Strait that began in summer 1990 and persisted at least through fall 1991. Modeled time series of volume flux through Near Strait over 26 years (Figure 5) show seven time periods when the transport was near-zero or even reversed. These anomalies last from three months to almost two years. While the model results do not show a lack of inflow at exactly the same time period as Stabeno and Reed (1992), the processes underlying the anomaly appear to be the same. These processes will be discussed in the next section. Stabeno and Reed (1992) note that a strong and prolonged reduction of inflow into the Bering Sea would likely lead to a large cooling of subsurface waters. A reduction of inflow would also promote salinization of surface waters, thereby increasing the depth of wintertime convection.

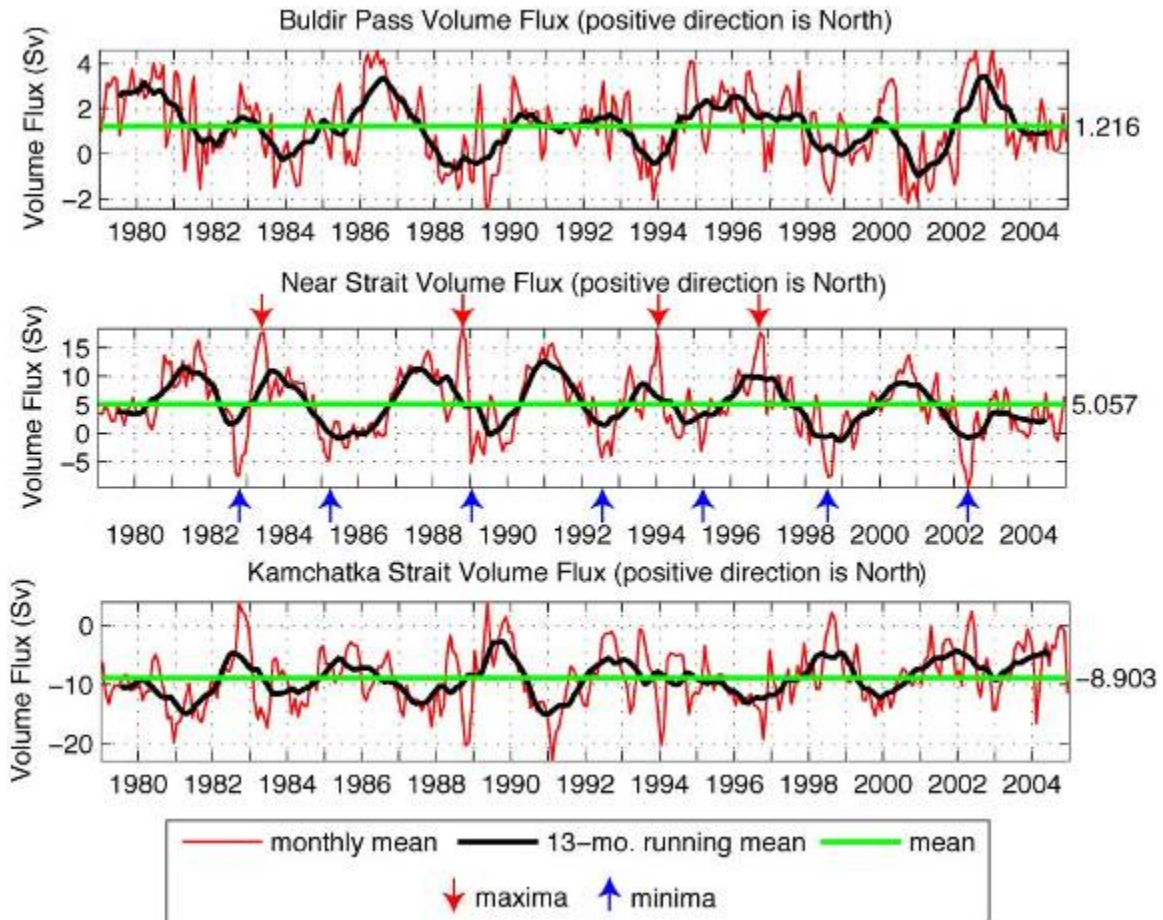


Figure 5. Monthly mean time series of net volume transport (Sv; red line) through selected sections, as indicated. The black line represents a 13-month running mean and the green line indicates the overall mean. Means for each time series are shown to the right of each panel. Local maxima (red arrows) and minima/flow reversals (blue arrows) are indicated on the Near Strait time series.

Kamchatka Strait is the westernmost pass and is the primary location of southward flow out of the Bering Sea. Estimates of the Sverdrup transports within the deep Bering Sea basin imply that the local mean wind stress curl accounts for a significant portion (about 6 Sv) of the Kamchatka Current (Bond et al. 1994), which flows southward out of the Bering Sea via Kamchatka Strait. Outflow through Kamchatka Strait was estimated at ~11 Sv based on observations during April–May 1990 and at 6–7 Sv during October–November 1990 (Verkhunov and Tkachenko, 1992). Stabeno and Reed (1992) made observations in Kamchatka Strait that yielded an estimate

of 6.8 Sv flowing southward during August 1991. However, they believe that this value is not typical of the Kamchatka flow, which instead is normally higher and closer to ~11 Sv. Panteleev et al. (2006) reconstructed the Bering Sea circulation as a variational inverse of the hydrographic and atmospheric climatologies, transport estimates through the Bering Strait, and surface drifter data. Based on this work, they estimate that the summer transport through Kamchatka Strait is 24 Sv southward, which is approximately twice as large as previous estimates. Panteleev et al. (2006) speculate that the difference between their estimate and previous observations is due to underestimation of the barotropic velocity component in the traditional transport estimates. The model results during 1979–2004 give a value of 8.9 Sv (S.D. = 4.8) net southward flow, which is within the range of the observations (Table 2), though much lower than the estimate by Panteleev et al. (2006). A more detailed comparison would be required to resolve this discrepancy, including the effect of only summertime observational results throughout the Bering Sea in the estimate by Panteleev et al. (2006) and their representation of the flow through other passes.

It is important to note that flow through these passes and straits is highly variable on time scales from weeks to years. Stabeno and Reed (1992) found a dramatic decrease in the inflow of Alaskan Stream water into the Bering Sea from summer 1990–fall 1991. At the time of their publication, this was completely unexpected, since all previously available measurements showed relatively constant values of inflow and outflow. A high degree of variation occurs in the modeled time series of volume flux through the western passes and straits. Several strong flow reversals occur over the course of the 26-year time series in Near Strait and Buldir Pass. Five flow reversals occur in Kamchatka Strait, up to a few Sv northward, during the 26-year simulation. The monthly mean volume flux time series through Near Strait and Kamchatka Strait are significantly correlated (at the 99% significance level). The correlation coefficient is -0.77 for the monthly means values and -0.79 when the annual cycle is removed from both time series. The correlation essentially means that when the inflow into the Bering Sea via Near Strait is strong, the outflow via Kamchatka Strait also tends to be strong. Also, when the flow through one of these straits is weak, the other would be expected to be weak. This correlation from

model results is in qualitative agreement with observations by Stabeno and Reed (1992), which showed a weakened Near Strait inflow (~ 3 Sv) coincident with a weakened Kamchatka Strait outflow (6–7 Sv) in August 1991.

2. Modeled Heat Fluxes

Twenty-six-year mean modeled heat fluxes across the Aleutian Island Passes are shown in Table 1. The reference temperature used to calculate the heat flux is the freezing temperature, which is based on salinity in this calculation. The highest net northward heat fluxes into the Bering Sea in descending order are through Near Strait, Amchitka Pass, Amukta Pass and Buldir Pass (Figure 6). The net monthly mean heat flux through Near Strait ranges from 203 TW southward to 483 TW northward. The range of variability is ~ 5.0 times the mean net heat flux (137 TW) at Near Strait. The net monthly mean heat flux through Amchitka Pass ranges from 96 TW southward to 287 TW northward. The range of variability is ~ 6.5 times the mean net heat flux (59 TW) at Amchitka Pass. The net monthly mean heat flux through Amukta Pass ranges from 6 TW southward to 137 TW northward. The range of variability is ~ 2.9 times the mean net heat flux (50 TW) at Amukta Pass. The net monthly mean heat flux through Buldir Pass ranges from 74 TW southward to 142 TW northward. The range of variability is ~ 5.8 times the mean net heat flux (37 TW) at Buldir Pass. Southward heat flux occurs primarily through Kamchatka Strait with a southward mean of 255 TW and a northward mean of 60 TW, which gives a net mean heat flux of 195 TW southward. When the net mean heat flux is summed for all of the cross-sections shown in Table 1, the total net mean heat flux across the Aleutian Island Passes is 87 TW northward.

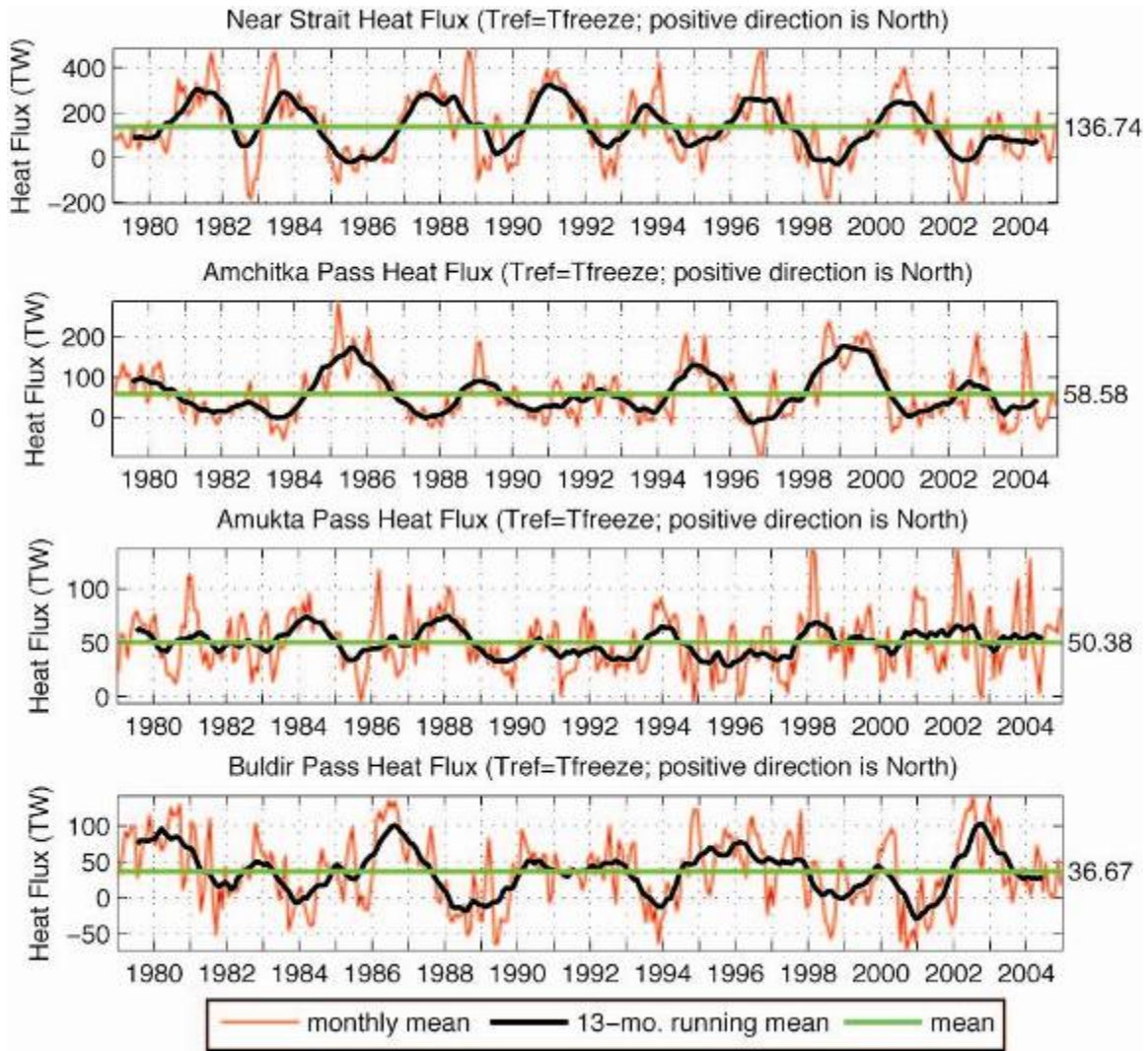


Figure 6. Monthly mean (red line), 13-month running mean (black line) and overall mean (green line) heat flux through selected passes as labeled. Heat flux is referenced to the freezing temperature, which is based on salinity.

3. Modeled Freshwater Fluxes

Freshwater flux, using a reference salinity of 33.8, was calculated across the sections shown in Figure 3. Almost 70% of the northward freshwater flux from the North Pacific into the Bering Sea occurs between Unimak and Amchitka Passes, even though only 37% of the volume transport inflow occurs there. The highest mean freshwater fluxes entering the Bering Sea occur through Amukta Pass, Amchitka Pass, Near Strait

and Buldir Pass, in descending order (Figure 7). The net monthly mean freshwater flux through Amukta Pass ranges from 3 mSv southward to 180 mSv northward. The range of variability is ~2.8 times the mean net heat flux (65 mSv) at Amukta Pass. The net monthly mean freshwater flux through Amchitka Pass ranges from 54 mSv southward to 135 mSv northward. The range of variability is ~3.8 times the mean net heat flux (50 mSv) at Amchitka Pass. The net monthly mean freshwater flux through Near Strait ranges from 110 mSv southward to 186 mSv northward. The range of variability is ~7.8 times the mean net heat flux (38 mSv) at Near Strait. The net monthly mean freshwater flux through Buldir Pass ranges from 48 mSv southward to 102 mSv northward. The range of variability is ~6.5 times the mean net heat flux (23 mSv) at Buldir Pass. When the net mean freshwater flux is summed for all of the cross-sections shown in Table 1, the total net mean freshwater flux across the Aleutian Island Passes is 67 mSv northward.

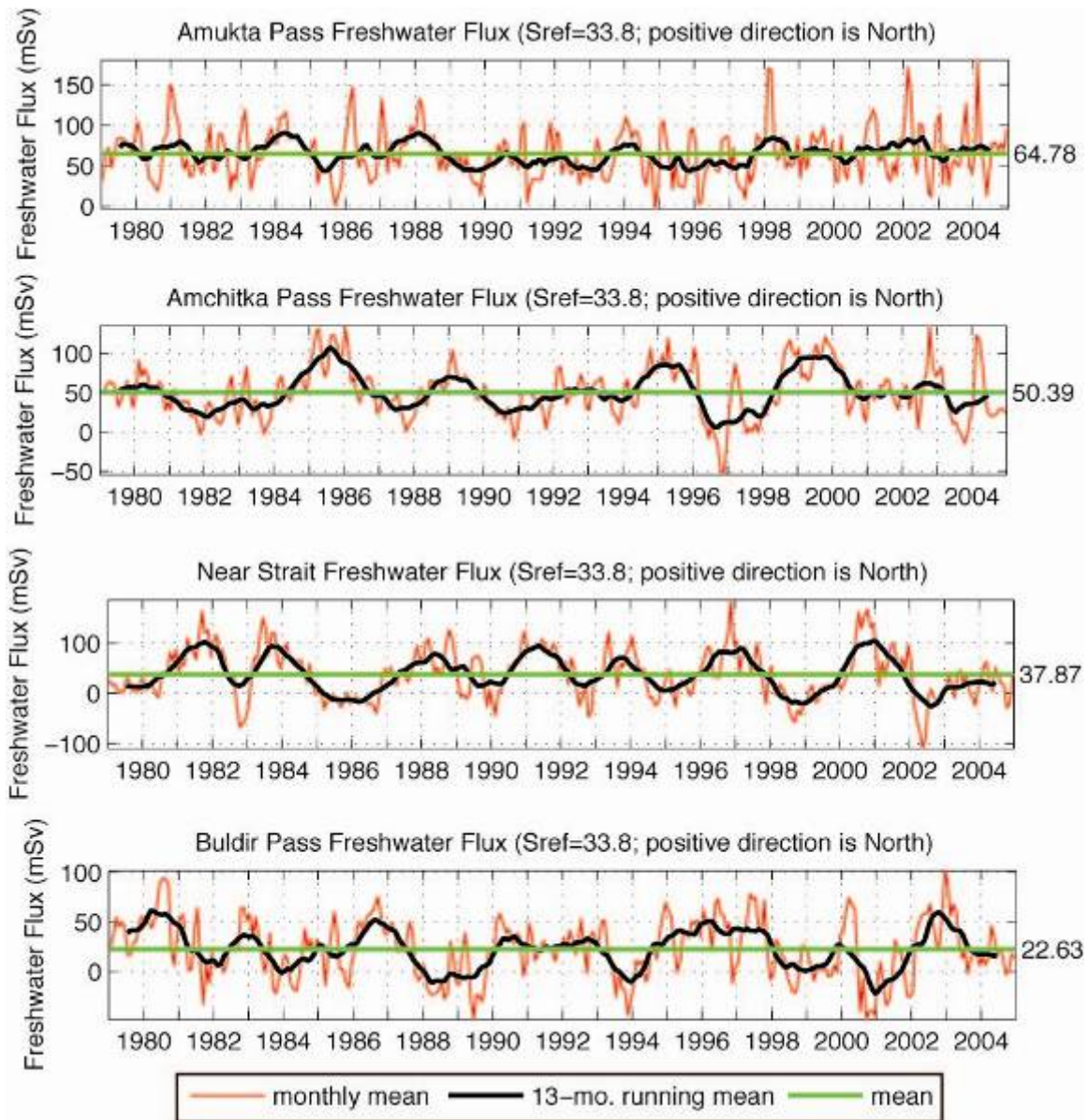


Figure 7. Monthly mean (red line), 13-month running mean (black line) and overall mean (green line) freshwater flux through selected passes as labeled. Freshwater flux is referenced to 33.8 psu.

D. MESOSCALE EDDIES IN THE ALASKAN STREAM AND THE DEEP BASIN

1. Eddies in the Deep Bering Sea Basin

The Bering Sea circulation over the deep basin is cyclonic in the mean, as shown in Figure 4. However, animations of monthly mean model results over the 26-year

simulation show frequent eddy activity throughout this area. For instance, at least 14 mesoscale eddies are present in the Bering Sea during June 1987, as shown in Figure 8 (Clement Kinney and Maslowski 2008). Half of these are anticyclonic and the other half are cyclonic. Diameters of these eddies are 120 km and greater and velocities are up to 40 cm/s. Lifetimes of these eddies are typically a few months. The 9-km horizontal resolution of the model makes it possible to resolve eddies with diameters as small as 36 km, however, the smallest eddies are likely not resolved. Recalling that the Bering Sea has a Rossby radius of deformation of $\sim 12\text{--}20$ km according to Chelton et al. (1998).

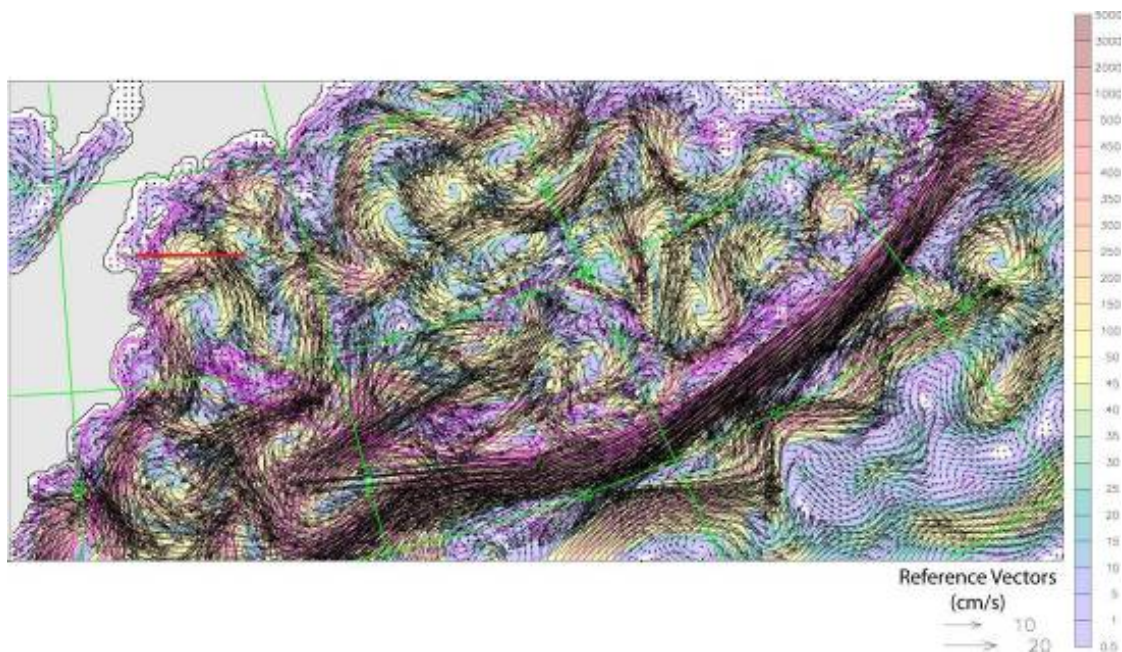


Figure 8. June 1987 upper 100 m circulation (vectors) and total kinetic energy (shading). Magenta contour lines represent bathymetry (m). The red line indicates the position of a cross section shown in Figure 5. Every second vector is shown.

Observations of eddies in the deep Bering Sea basin have been made by Cokelet et al. (1996) and Stabeno and Reed (1994), among others (e.g., Solomon and Ahlnäs 1978; Kinder et al. 1980; Paluszkievicz and Niebauer 1984). Stabeno and Reed (1994) observed a large anticyclonic eddy west of Bowers Ridge that had a diameter of ~ 200 km and velocities of 30–40 cm/s. This eddy is similar in size and velocity to those from the

model; diameters are 120 km and greater, with velocities up to 40 cm/s. Cokelet et al. (1996) also observed a strong anticyclonic eddy here and suggested that it may be a recurring feature.

Schumacher and Stabeno (1994) suggest several possible mechanisms for the formation of eddies in this region, including instabilities, wind forcing, strong flows through the passes, and topographic interactions. Cokelet et al. (1996) suggest that instabilities along the Bering Slope and Kamchatka Current and interactions with canyons and embayments at the landward edge of these currents, as well as inflows through the Aleutian Island Passes, may be responsible for eddy generation. Stabeno and Reed (1994) observed several eddies and meanders within the Kamchatka Current and the Bering Sea Basin by utilizing satellite-tracked drifters. Several anticyclonic eddies were observed in the western side of the basin and resulted from the interaction of the Kamchatka Current with topographic features. Stabeno and Reed (1994) suspect that these features are semi-permanent, since they appeared in drifter trajectories from more than one year. Model results (Figure 8) show two anticyclonic eddies associated with the Kamchatka Current during June 1987. (A cyclonic eddy (part of a counter-rotating pair) is also present near the Kamchatka Current at that time.)

A vertical section of potential temperature through the southernmost eddy (Figure 9; cross-section location shown in Figure 8) shows the cold core of the eddy with temperatures less than 1°C from ~25–250 m depth. The anticyclone reversed the flow of this boundary current to over 15 cm/s northward, with a (local) southerly flow ~75 km further offshore due to the eddy. Temperatures were up to 2.5 °C colder than the 26-year mean within the core of the eddy. Typical June temperatures in this location are 1.5–3°C and the usual speed of the southward-flowing Kamchatka Current is up to 9 cm/s in the core (Figure 9). A shallower thermocline is also apparent when the eddy is present, as shown by the temperature difference Figure 9c (negative values just below the surface). The temperature signature of the modeled eddy is similar to observations by

Rogachev et al. (2007) of cold-core eddies within the Kamchatka Current. One of the observed eddies was located just south of Kamchatka Strait and displayed temperatures near 0°C at its core.

The salinity section reveals a strong displacement of isohalines (> 200 m) across the eddy during June 1987, as compared to the 26-year mean (1979–2004; Figure 10a). The relatively fresh core of the anticyclone exhibited salinities of 32.5 as deep as 200 m. Typically, water with such a fresh signal is confined to the shelf (Figure 10b). Salinity differences (between June 1987 and the 26-year mean June) show that the core of the eddy was up to 0.75 psu fresher than average, as well as ~ 0.15 psu fresher at the surface. Rogachev and Gorin (2004) observed salinities of < 33 psu in an eddy near Kamchatka Strait during April 1991.

Animations (not shown) of monthly mean velocity and sea surface height anomaly show that over the 26-year simulation (1979–2004), the Kamchatka Current was continuously populated with meanders and southwestward-moving anticyclonic eddies, such as the one just described. The diameters of these eddies were 83–139 km and the lifetimes were typically a few months. This is corroborated by observations of eddies with similar trajectories (Rogachev and Gorin 2004; Rogachev and Carmack 2002). Okkonen (1993) suggested that the anticyclonic eddies found in the western Bering Sea, such as the ones found within the path of the Kamchatka Current, may be related to planetary topographic waves.

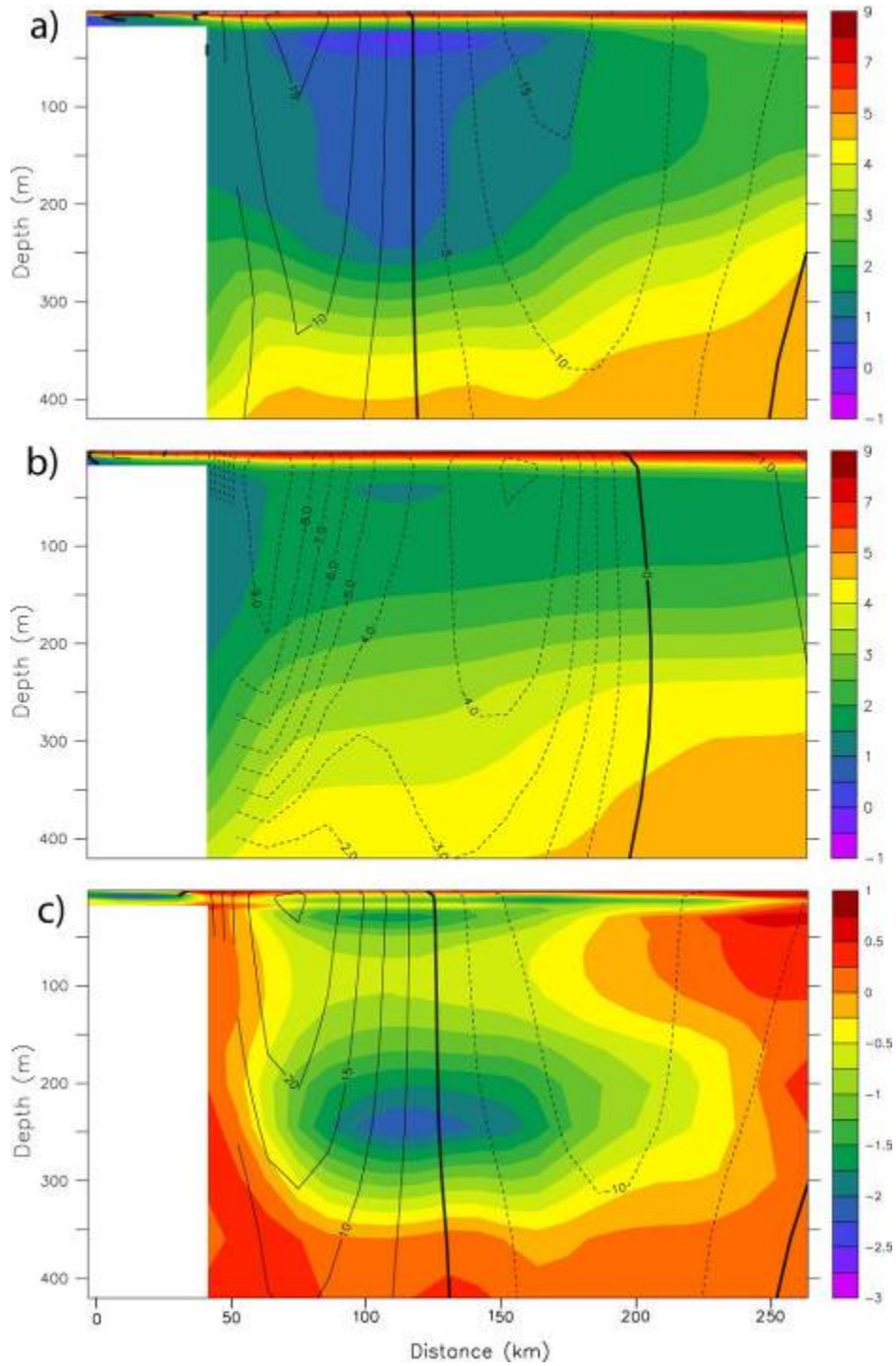


Figure 9. Vertical cross-sections of potential temperature ($^{\circ}\text{C}$; color shading) and velocity (cm/s ; contours) along the red line in Figure 4 during (a) June 1987, (b) 26-year mean June, and (c) the difference between these time periods. Solid contour lines indicate northward velocity and dashed lines indicate southward velocity.

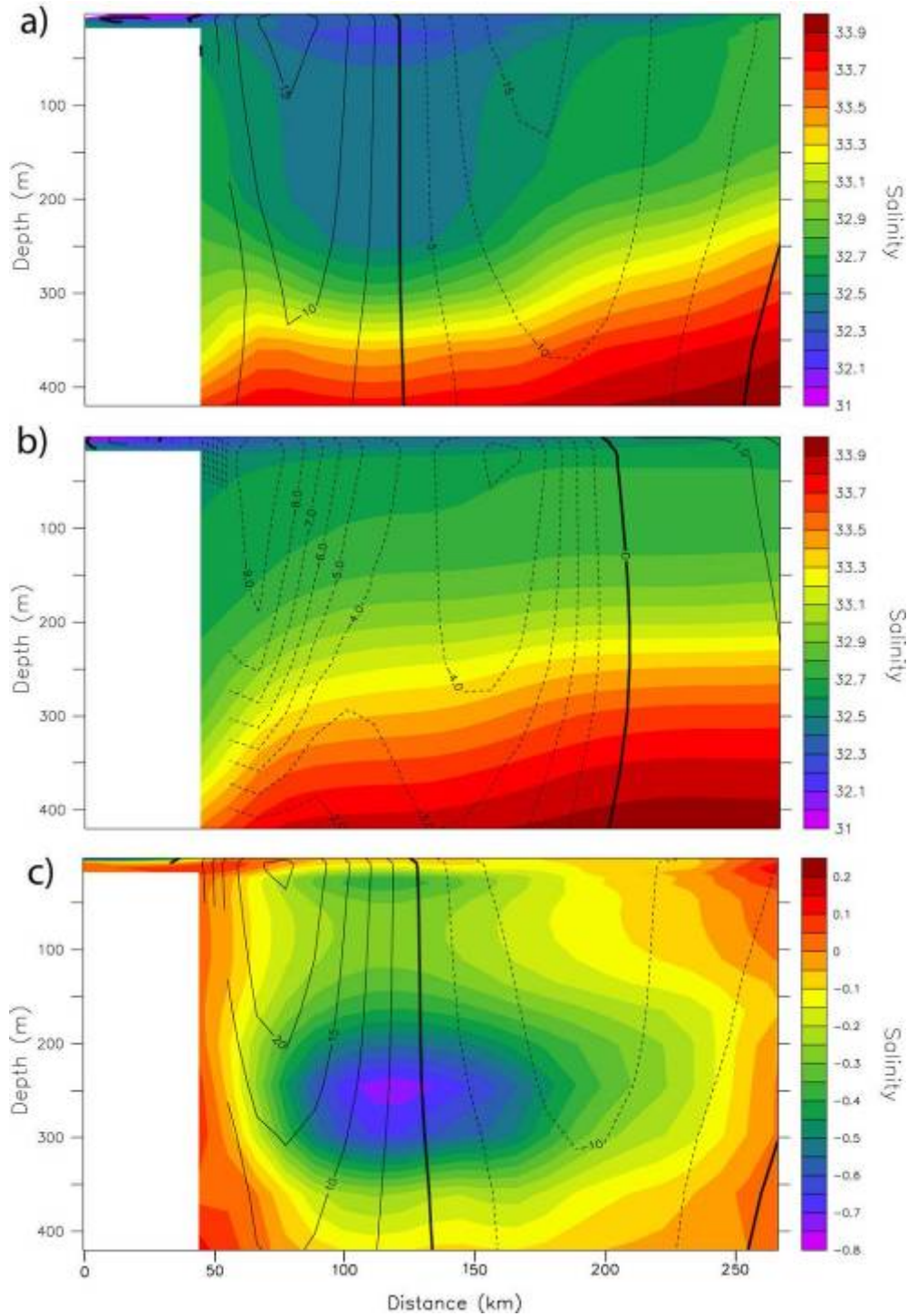


Figure 10. Vertical cross-sections of salinity (color shading) and velocity (cm/s; contours) along the red line in Figure 4 during (a) June 1987, (b) 26-year mean June, and (c) difference between these time periods. Solid contour lines indicate northward velocity and dashed lines indicate southward velocity.

2. Eddies in the Alaskan Stream

Maslowksi et al. (2008a) discussed anticyclonic eddies that propagate along the path of the Alaskan Stream with an average diameter of 168 km and phase speed of ~ 2.3 km day⁻¹. These are similar to observations by Okkonen (1992), as well as those of Crawford et al. (2000) who detected the presence of six anticyclonic eddies over a period of seven years with an average diameter of 160 km and a mean phase speed of ~ 2.5 km day⁻¹. In the model simulations, these eddies did not reduce the strength of the Alaskan Stream, however there was an off-shore (or southward) shift in the velocity core. The mesoscale eddies were shown to have a strong effect on the volume and property fluxes through the eastern and central Aleutian passes (Maslowksi et al. 2008a). Large increases in the northward volume, heat, and salt fluxes through Amukta and Amchitka passes occurred during the presence of an eddy in the Alaskan Stream (Maslowksi et al. 2008a). Okkonen (1996) estimated that an eddy observed to separate from the Alaskan Stream south of Amchitka Pass represented 21% of the mean annual transport into the Bering Sea.

Model results show that the larger and deeper passes of the western Aleutian Islands are also affected by these mesoscale features. The numerous eddies and meanders of the Bering Sea and within the Alaskan Stream play a critical role in determining the flow through the western Aleutian passes and straits. As mentioned above, there were seven flow reversals in Near Strait throughout the 26-year simulation. Eddy activity in the vicinity of the strait has a strong impact on the flow through the strait. Figure 11 shows the local circulation in the upper 400 m during each of the seven flow reversals. There does not appear to be a consistent circulation regime associated with a flow reversal, instead the reversals occur due to the relative positions of multiple eddies and meanders both north and south of Near Strait. For example, during October 1982 (Figure 11), mesoscale activity modified the flow through Near Strait: on the eastern side, a large anticyclone modified the path of the Alaskan Stream inflow and on the western side, anticyclonic flow is found within the strait, creating a strong southward flow. A total of 18.6 Sv flowed southward at this time, with 11 Sv flowing northward,

which equaled a net southward flux of 7.6 Sv. In March 1985, a large anticyclone has pushed part of the Alaskan Stream into Near Strait, causing a southward flow there. At the same time, the anticyclone is blocking northward flow through the strait. During May 1989, an anticyclone is actually responsible for a northward flow (10.5 Sv) in the eastern part of Near Strait, however a stronger southward flow (14.3 Sv) exists across the western part of the strait (likely due to a cyclone to the north), which gives a net southward transport of 3.8 Sv. Anticyclonic blocking occurs again in July 1992, March 1995, and May 2002. August 1998 shows a strong southward flow in the central part of Near Strait, which originates in the Bering Sea, due to local cyclonicity.

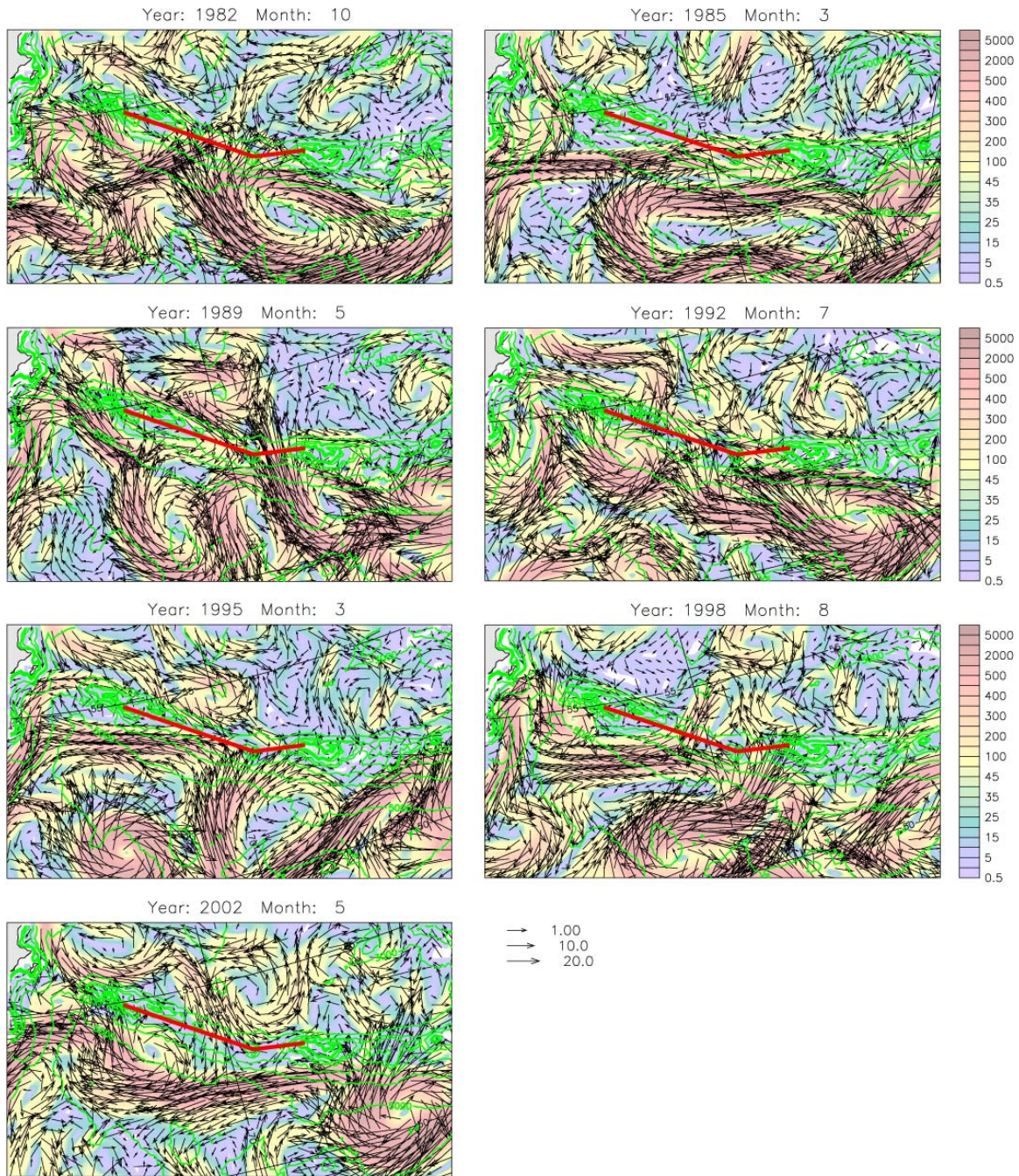


Figure 11. Monthly mean total kinetic energy (shading; cm^2/s^2) and velocity vectors (cm/s) in the upper 400 m during each of the flow reversals as shown in Figure 5. The year and month are indicated above each panel. The red line indicates the position of Near Strait and the green contour lines indicate bathymetry.

Four local maxima are identified in the time series of volume transport through Near Strait (Figure 5). Similar to the flow reversals, these maxima are strongly affected by eddies and meanders both north and south of the strait. During June 1983, the northern part of a large, irregularly shaped anticyclone reached into the strait, thereby creating a strong net northward flow (17.7 Sv; Figure 12). Note that this same anticyclone contributed to a flow reversal 8 months earlier by blocking northward flow in the eastern part of the strait (Figure 11). The October 1988 circulation pattern is quite complex, however a strong northward flow in the central part of the strait appears to be related to an anticyclonic meander of the Alaskan Stream. January 1994 and March 1996 both show upstream anticyclones that are pushing water northward through the eastern part of Near Strait.

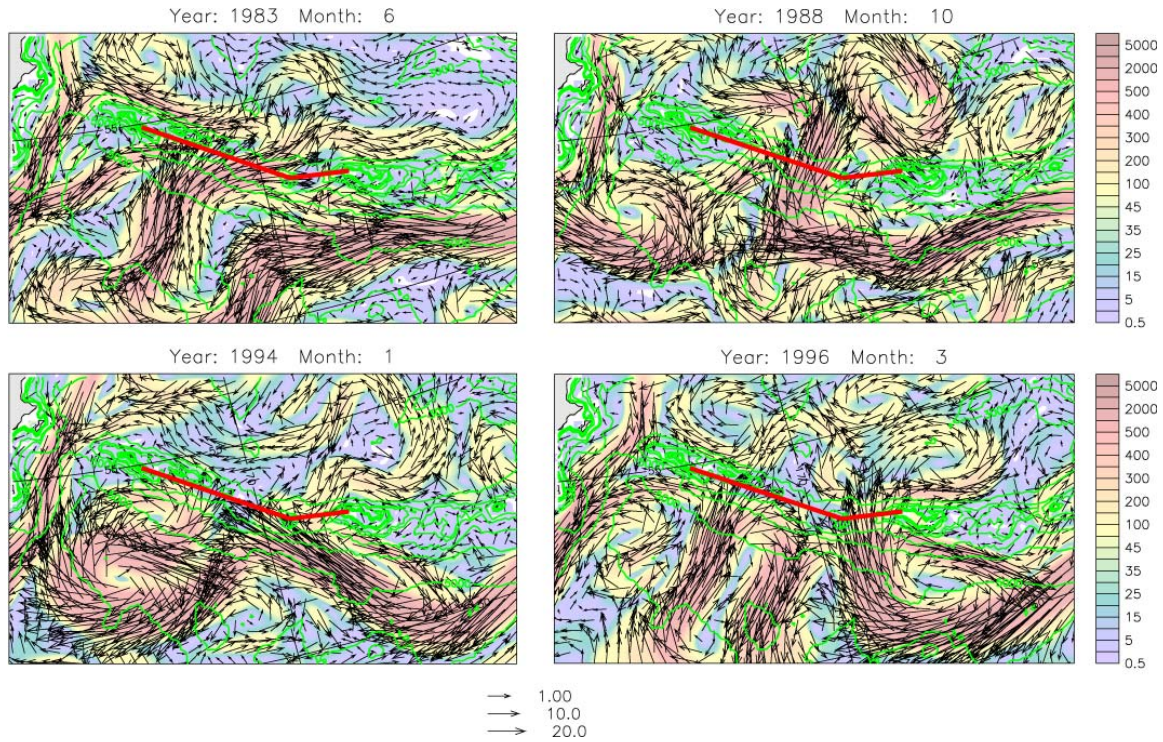


Figure 12. Monthly mean total kinetic energy (shading; cm^2/s^2) and velocity vectors (cm/s) in the upper 400 m during each of the flow maxima as shown in Figure 5. The year and month are indicated above each panel. The red line indicates the position of Near Strait and the green contour lines indicate bathymetry.

E. CONCLUSIONS

High-resolution modeling of the Bering Sea basin has been limited. Hermann et al. (2002) presented results from their regional, eddy-resolving model for 1995 and 1997. However, their limited domain (the southeast Bering Sea) did not include the Bering Sea basin. Instead, they focused on comparing hindcast results from 1995 and 1997, primarily of the eastern portion of the Bering Slope Current and the ANSC. Model results were also compared with Eulerian and Lagrangian observations.

Previous modeling work by Overland et al. (1994) focused on a limited domain: from 166°W to 157°E and from 46°N to the Bering shelf break. The primitive equation, three-layer hydrodynamic model had $1/8^{\circ}$ resolution and excluded shallow regions <500 m deep. The Alaskan Stream was specified as a boundary condition at inflow and outflow points with a constant volume transport of 15 Sv. This approach allowed Overland et al. (1994) to realize general circulations features (e.g., complex cyclonic flow in the Bering Sea basin) similar to observations. However, they were not able to simulate the meanders in the Kamchatka Current that were identified by Stabeno and Reed (1994), nor were they able to show enough interannual variability in the flow through Near Strait to account for observations by Stabeno and Reed (1992) or Reed et al. (1993). The prescribed boundary condition for the Alaskan Stream and the climatological atmospheric forcing that was used may have prevented Overland et al. (1994) from simulating realistic variability in the flow through Near Strait. Although early observations (e.g., Reed 1984; Stabeno and Reed 1991) showed little eddy energy of the Alaskan Stream where it entered the Overland et al. (1994) domain (near 166°W), more recent observations are in stark contrast. For example, Crawford et al. (2000) observed 6 multi-year anticyclonic meanders and eddies in the Alaskan Stream using data from the TOPEX/Poseidon altimeter between 1992 and 1998. All of these mesoscale features formed east of 166°W , with some forming east of Kodiak Island. The range of variability in the Near Strait inflow from Overland et al. (1994) was between $\sim 5\text{--}7$ Sv (see Figure 7 in Overland et al. 1994) over a period of ten years (sampled daily), whereas NAME simulates variability between -9.5 and 18.3 Sv over a period of 26 years (sampled monthly; Figure 5).

Results presented herein are the first from a high-resolution, multi-decadal simulation of the entire Bering Sea. Utilizing a large pan-Arctic domain with a non-prescribed Alaskan Stream and Aleutian throughflow allows reproduction of the observed meanders and eddies in the Alaskan Stream and Kamchatka Current (Figure 8). Strong interannual variability in flow through Near Strait (Figure 5) was simulated by the model, which captures (and exceeds) the range of variability that has been observed (Stabeno and Reed 1992; Reed et al. 1993). The modeled net northward flow through Near Strait approached zero and reversed 7 times from 1979–2006 for time periods of three months to two years. Therefore, it is believed that short-term observations (months to years) may not be representative of the actual mean flow. This indicates a need for continuous monitoring of the flow through Near Strait.

During the 26-year simulation, meanders and eddies are continuously present in the Kamchatka Current, as well as elsewhere throughout the Bering Sea. This is consistent with results from Cokelet and Stabeno (1997), which show that the background flow in the interior of the Bering Sea is dwarfed by the energetic eddies which populate the region.

THIS PAGE INTENTIONALLY LEFT BLANK

V. SHELF-BASIN EXCHANGE AND OUTER SHELF DYNAMICS

A. INTRODUCTION

The research presented in this chapter seeks to identify and discuss the regions and processes of shelf-basin exchange within the Bering Sea. It is also an attempt to provide a quantitative measure of mean volume and property fluxes across the outer shelf, defined as a region between 50-m and 200-m isobaths. This exchange is important to biological productivity along the slope and on the Bering Sea shelf because the deep basin is the main source of nutrients for these locations. In addition, the downstream biological production within the Chukchi and Beaufort seas is strongly dependent upon the influx of nutrients from the deep Bering Sea via Bering Strait (Walsh et al. 1989; Codispoti et al. 2005; Walsh et al. 2004; Walsh et al. 2005). Without this nutrient source, biological production on the Bering Sea shelf and, consequently, in the Western Arctic would be much lower. Stabeno et al. (1999) state a need to identify and understand the mechanisms, which provide nutrients to the euphotic zone of the Bering Sea shelf. Model results presented herein will describe some of these mechanisms.

A description of the general circulation from the long-term-mean point of view based on model results is presented in Section B. Sections C–E present analyses of volume, heat, salt, and freshwater transports through a number of cross-sections spanning the entire outer shelf, which is an attempt to determine the important pathways of shelf-basin exchange and describe the outer shelf dynamics. Section F contains a description of the mean state and variability of the Bering Slope Current and also includes a discussion of the eddy kinetic energy. Section G contains analysis of the exchanges through Zhemchug Canyon and the effects of eddy interactions along the slope and within canyons on shelf-basin exchange. Finally, the results of the study are discussed and major findings are identified in Section H. This chapter was published by Clement Kinney et al. (2009).

B. GENERAL CIRCULATION

Twenty-six-year (1979–2004) mean modeled circulation and TKE (0–220 m) are shown in Figure 13. The Alaskan Stream to the south of the Aleutian Island Chain and Anadyr Current (between Siberia and St. Lawrence Island) reach mean speeds in excess of 35 cm/s. The Bering Slope Current (BSC) is characterized by speeds up to ~12 cm/s in the long-term mean. The Bering Sea middle shelf domain ranges between < 1–7 cm/s, with higher speeds located north of the Zhemchug Canyon region (~170–175°W).

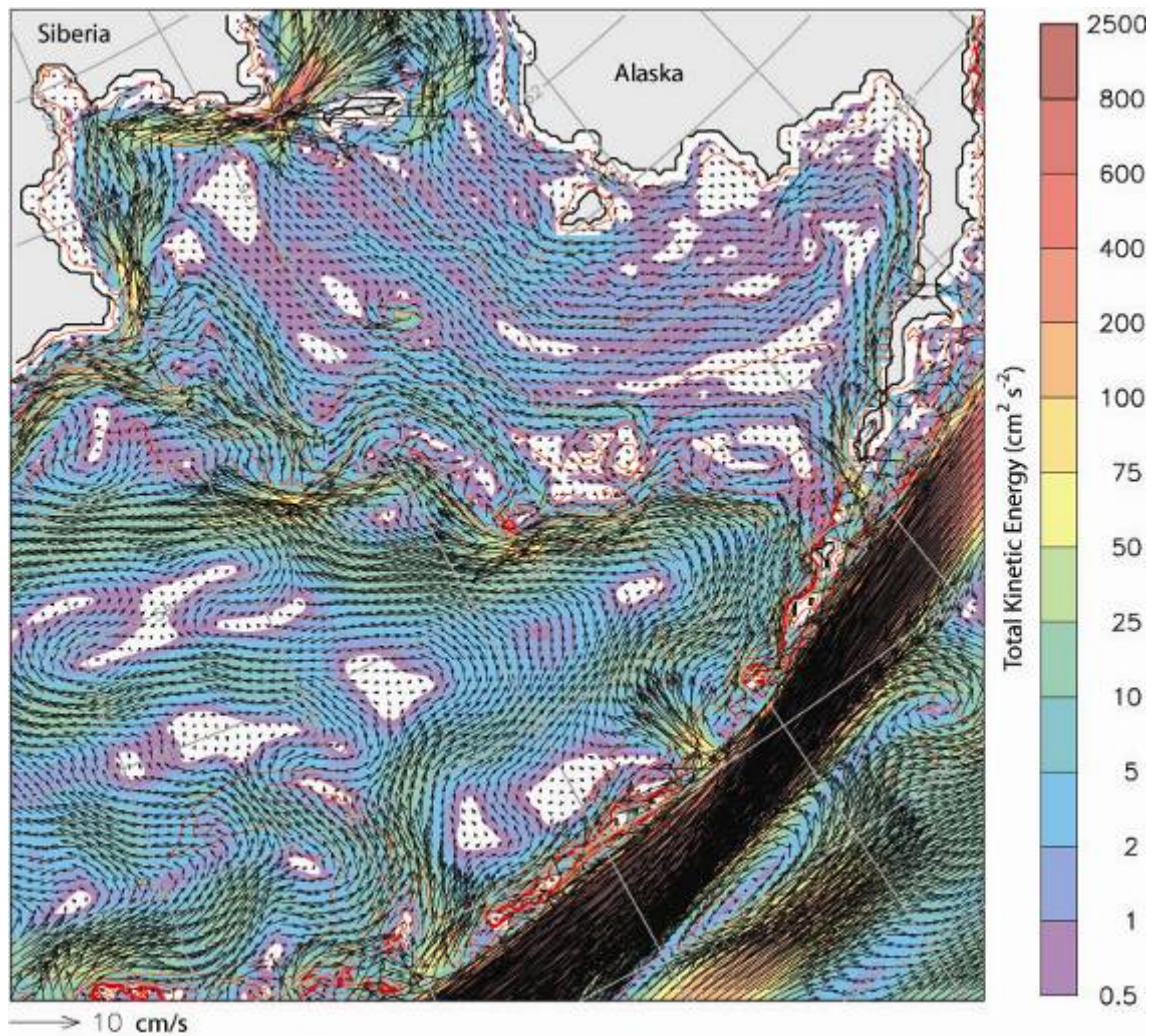


Figure 13. 26-year (1979–2004) mean 0–220m circulation and total kinetic energy. Every second vector is shown.

Previous modeling and observational studies (Kinder et al. 1986, see Figure 5; Schuert and Walsh 1993) mention that the BSC splits into two branches as it nears the coast of Siberia near Cape Navarin. One branch was believed to turn north and circulate around of the Gulf of Anadyr, while the other was thought to turn southward and eventually, form part of the Kamchatka Current. However, little direct observational evidence is available to substantiate this idea. Model results show that the vast majority of the BSC follows the bathymetry and turns south as it nears Cape Navarin (Figure 13; see Figure 14 for geographic place names). Very little to none of the water from the BSC turns northward upon nearing the Siberian coast. There is also evidence of a narrow coastal current flowing northward around the cape; however this northward flowing water is not derived from BSC water. Based on their observations, Stabeno et al. (1999) propose a schematic circulation in agreement with model results presented here, showing the majority of BSC water turning southward near Cape Navarin.

In an effort to visually simplify the mean circulation, a schematic circulation based on Figure 13 was constructed (Figure 14). This is an update to a previously published schematic (Figure 1 in Clement et al. 2005) and the major difference is the above-mentioned southward turn of the Bering Slope Current as opposed to a north-south split. The current schematic shows the generally northwestward flow across the shelf, as well as the Anadyr Current and Alaska Coastal Current (ACC). The Alaskan Stream is strongest with significant throughflow (primarily northward into the Bering Sea) occurring through Unimak, Amukta and Amchitka passes.

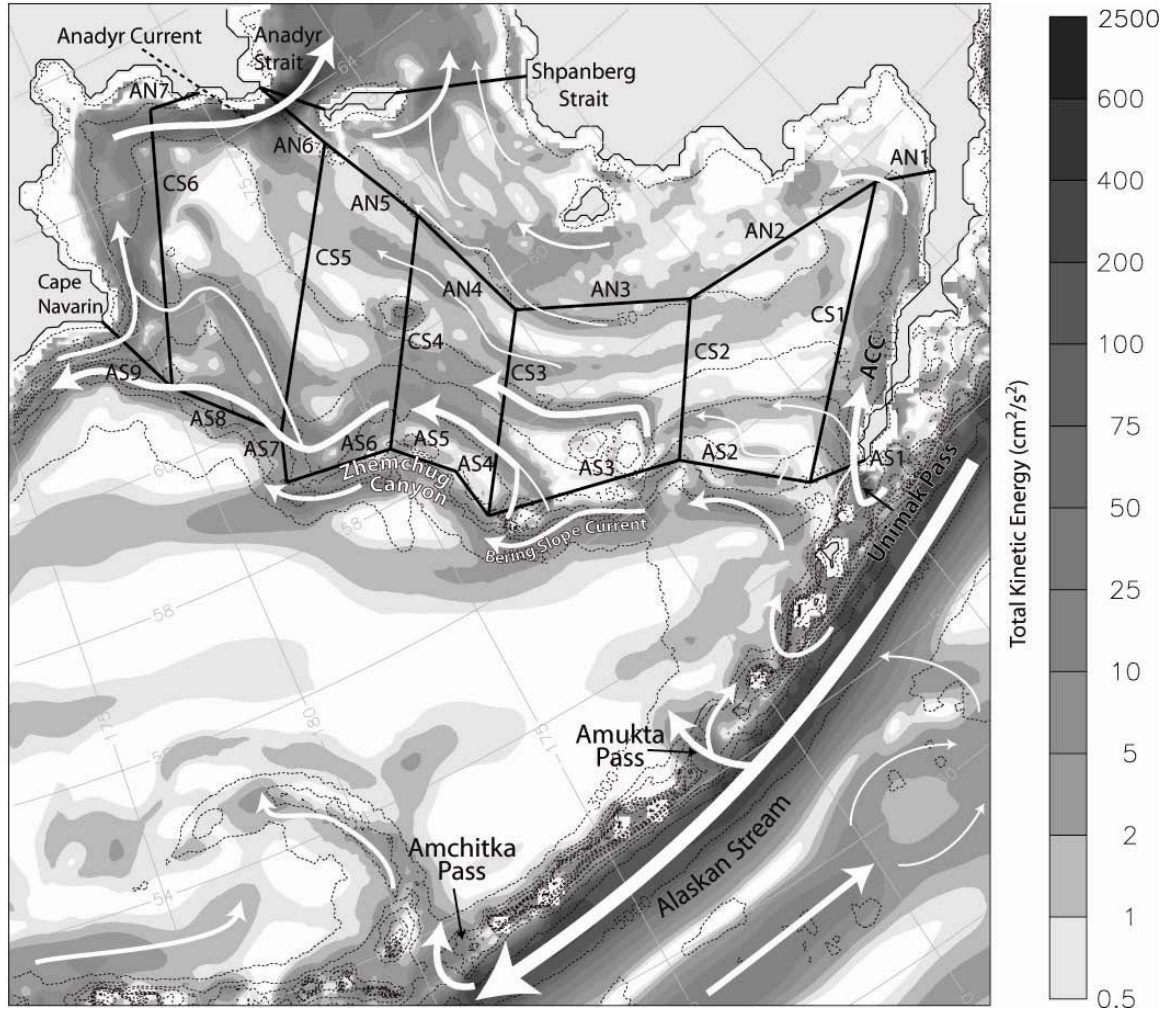


Figure 14. Schematic circulation (0–220m) and total kinetic energy based on Figure 13. The locations of model cross-sections and names are included.

C. VOLUME TRANSPORT

We have created a series of cross-sections, which approximate the 50- and 200-m isobaths and several sections connecting the two isobaths. Monthly mean values of volume, heat, salt and freshwater flux across each section were calculated for the years 1979–2004. Table 3 shows the 26-year mean values of these fluxes for each cross-section. The section locations are shown and labeled in Figure 14. Figure 15a shows the 26-year mean value of volume transport (S_v) across each section with an arrow indicating the mean direction of flow. Arrows are scaled as a percentage of the largest cross-sectional value shown in the figure (e.g., a volume transport of 0.5 S_v would have an

arrow twice as wide as a section with volume transport of 0.25 Sv). The net volume transport is positive (on-shelf) in the central and eastern part of the Bering Sea along the 200-m isobath. It is highest through the section north of Unimak Pass (AS1). In contrast, the westernmost sections (AS7–AS9) have relatively small negative (off-shelf) mean volume transport values. This is largely due to the separation of the BSC from the shelf-break west of AS6, which removes the source of large (>0.05 Sv) on-shelf transports. The cross-shelf sections (CS1–CS6) increase in volume transport from east to west, as upwelled water is accumulated and integrated into a generally northwestward flow along the outer shelf. The sharpest increase between consecutive cross-shelf sections occurs between CS3 and CS4 (increase of 0.224 Sv) over a distance of approximately 230 km. This increase in shelf transport is due to water being moved on-shelf through the Zhemchug Canyon (AS4–AS6) to the south. Sections along the 50-m isobath have very small values of net volume transport, except for section AN6, which has a value of 0.528 Sv or ~83% of the total net northward volume transport across the 50-m isobath. Bathymetric steering is the main cause of the low volume transports through sections AN1–AN5, since the 50-m isobath directs water toward AN6 and eventually through Anadyr Strait, which is a deeper pass than the eastern Shpanberg Strait.

Table 3. 26-yr mean volume transport (Sv), salt flux (million kg/s), freshwater flux (mSv; relative to 34.8), and heat transport (TW; relative to -0.1°C). Numbers in parenthesis represent standard deviation.

Section	Volume transport	Salt flux	Freshwater flux	Heat flux
AS1	0.200 (0.097)	6.398 (3.095)	16.142 (7.992)	5.052 (2.909)
AS2	0.142 (0.092)	4.562 (2.961)	10.803 (7.128)	2.951 (2.165)
AS3	0.145 (0.146)	4.687 (4.686)	10.669 (10.867)	2.351 (2.984)
AS4	0.093 (0.063)	2.991 (2.042)	6.701 (4.599)	1.755 (1.315)
AS5	0.124 (0.070)	4.021 (2.279)	8.877 (5.001)	2.184 (1.485)
AS6	0.125 (0.137)	4.052 (4.433)	8.435 (9.435)	2.164 (2.448)
AS7	-0.086 (0.103)	-2.777 (3.345)	5.897 (7.063)	-1.189 (1.891)
AS8	-0.003 (0.100)	-0.111 (3.223)	-0.146 (7.086)	0.555 (1.476)
AS9	-0.048 (0.316)	-1.545 (10.179)	-3.360 (23.526)	0.192 (2.459)
CS1	0.168 (0.146)	5.367 (4.654)	13.875 (12.092)	2.438 (3.797)
CS2	0.280 (0.152)	8.950 (4.854)	22.939 (12.246)	3.372 (2.487)
CS3	0.355 (0.276)	11.383 (8.849)	28.004 (21.438)	3.808 (28.004)
CS4	0.579 (0.297)	18.602 (9.541)	44.927 (22.971)	5.184 (3.778)
CS5	0.606 (0.333)	19.483 (10.712)	46.523 (25.698)	4.252 (3.507)
CS6	0.073 (0.312)	2.331 (10.013)	6.158 (24.108)	0.895 (2.380)
AN1	0.042 (0.049)	1.336 (1.559)	3.732 (4.453)	1.506 (1.835)
AN2	0.023 (0.089)	0.718 (2.814)	2.101 (8.439)	0.061 (1.951)
AN3	0.067 (0.122)	2.118 (3.848)	6.037 (11.000)	0.536 (1.533)
AN4	-0.017 (0.074)	-0.526 (2.347)	-1.445 (6.721)	0.027 (1.171)
AN5	0.011 (0.080)	0.361 (2.568)	0.786 (6.656)	0.067 (0.816)
AN6	0.528 (0.187)	17.065 (5.973)	37.644 (16.393)	1.737 (2.533)
AN7	-0.019 (0.018)	-0.620 (0.581)	-1.058 (1.066)	-0.042 (0.130)
Shpanberg Strait	0.132 (0.128)	4.219 (4.040)	10.607 (11.793)	1.058 (2.187)
Anadyr Strait	0.521 (0.179)	16.842 (5.700)	37.247 (16.173)	1.799 (2.597)

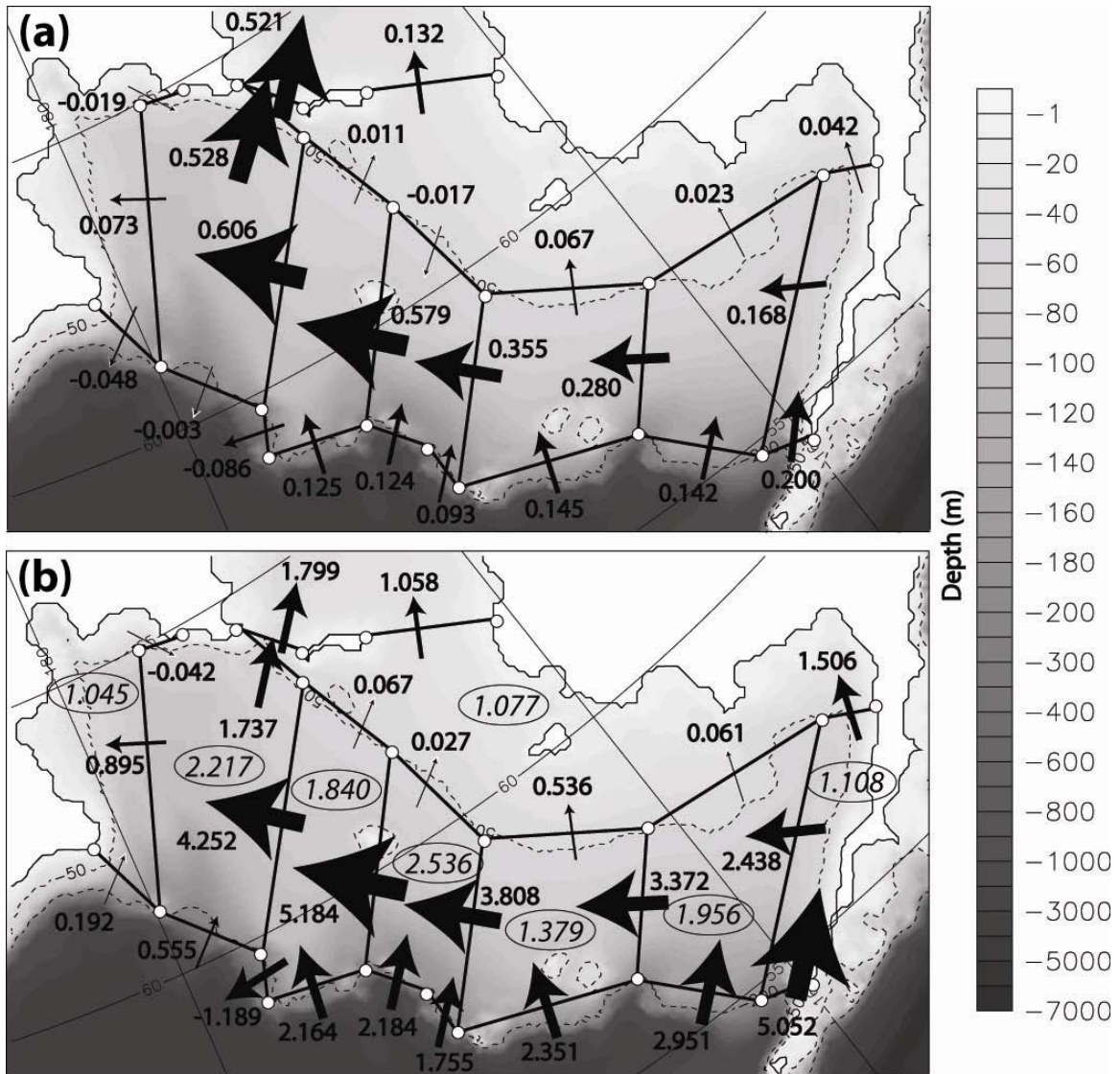


Figure 15. 26-year (1979–2004) volume transport (Sv; a) and heat flux (TW; relative to -0.1°C ; b) across various sections. Arrows indicate net direction (positive is North or West) and are scaled relative to the largest value in each figure. The shading indicates depth (m). The 50 m and 200 m isobaths are shown as dotted lines. The mean flux divergence for each polygon is shown in italics and is circled.

D. HEAT TRANSPORT

The heat flux referenced to -0.1°C was calculated through the sections shown in Figure 14. Pathways of heat transport onto and across the Bering Sea shelf are somewhat different from those of volume transport (Figure 15b). This is due to differing pathways of warmer (less dense) water from colder (more dense) water. The majority of heat flux onto the shelf occurs through section AS1 and is primarily water that has recently entered the Bering Sea via eastern Aleutian Island Passes and is relatively warm. Differences between volume and heat flux are also due to the fact that exchanges between the ocean and atmosphere change the amount of heat in the ocean over time, while the volume remains relatively constant. The largest on-shelf oceanic heat flux is through Zhemchug Canyon (a total of 6.1 TW through sections AS4–AS6), with the second largest on-shelf heat flux through Bering Canyon (5.1 TW, section AS1). In Figure 15b and Figure 16ab, several polygons are created by the cross sections. The mean values of heat transport, salt flux and freshwater flux across each section for each polygon are summed, such that means directed into/outside the polygon are positive/negative. The resulting sum (the flux divergence) is shown circled and in italics inside each respective polygon. The flux divergence values shown in Figure 15b indicate that a large amount of heat (2.5 TW) is lost to the atmosphere in the polygon northwest of Zhemchug Canyon that is bounded by CS3, AS4, AS5, CS4, and AN4. Lower heat flux divergence values occur in the easternmost and westernmost polygons, and also in the polygon north of the 50-m isobath.

along the 200-m isobath (AS1–AS9; shown in Figures 14 and 15b). Approximately 75% of this heat is lost to the atmosphere between the 200- and 50-m isobaths. (The sections used in calculating the total heat flux across the 50-m isobath were AN1–AN6). A smaller loss occurs between the 50-m isobath and Anadyr and Shpanberg straits. Eventually, the net oceanic heat flux into the Chukchi Sea through Bering Strait is ~ 2.4 TW or 14.9% of the 200-m isobath value. This implies that an increase in Bering Sea heat content could have a large impact on the Arctic Ocean, especially in light of the recent decline in sea ice.

Table 4. Net heat transport (TW) across various locations in the Bering Sea.

Location	Heat transport (TW)	Percentage of 200-m isobath value
200-m isobath	16.015	100%
50-m isobath	3.934	24.60%
Anadyr + Shpanberg straits	2.857	17.80%
Bering Strait	2.383	14.90%

E. SALT AND FRESHWATER TRANSPORT

The mean salt flux through the Bering Sea sections (Figure 16a) closely resembles the mean volume transport in a relative sense, due to the strong dependence of salt flux on volume flux. Significant on-shelf salt fluxes occur between Bering Canyon and Zhemchug Canyon and, as a result, cross-shelf fluxes (CS1–CS5) on the outer shelf increase as the water moves northwestward across the shelf. The vast majority of salt transport on the outer shelf (17 million kg/s or 83% of the total) eventually crosses the 50-m isobath at AN6 near Anadyr Strait, with very little northward salt transport northward across the central and eastern sections. This is primarily due to bathymetric steering, as mentioned above in Section C; the 50-m isobath directs the shelf flow toward AN6 and eventually northward through Anadyr Strait.

The mean freshwater flux (referenced to $S=34.8$) through the Bering Sea sections shows that the primary freshwater route across the 200-m isobath is through the easternmost section (AS1; Figure 16b). This section accounts for 31% of the total net northward freshwater transport along the 200-m isobath. Similar to volume and salt transport, the total freshwater flux accumulates as water moves northwestward across the shelf through sections CS1–CS5. Then, the majority of freshwater turns northeastward and flows through Anadyr Strait. Figure 16ab shows that the polygon in the Gulf of Andyr (bounded by AN6, CS5, AS8, CS6, and AN7) has the highest values for salt and freshwater flux divergence. This is likely related to the large amount of sea ice produced and melted in this region, along with sea ice export/import into the polygon from surrounding areas.

F. BERING SLOPE CURRENT

The Bering Slope Current extends from the eastern Aleutian Islands along the shelf-break toward Cape Navarin. It is a relatively broad, northwestward flow and, more recently, has been described as a system of eddies (Okkonen 1993). Eddies ranging in size from 90 to 325 km are found to populate the Bering Sea basin, especially along the downstream portion of the Bering Slope Current to the northwest (see previous chapter). Several cross-sections across the Bering Slope Current and across several canyons that lie along the Bering Sea shelf-break were created to examine the flow and property fluxes in this region (locations of these cross-sections are shown in Figure 17). Figure 18 shows time series of monthly mean volume transport, heat flux, and section mean temperature through sections BSC1 and BSC4 from model results. The long-term mean volume transport for the BSC is 2–3.5 Sv. Flow reversals occur periodically at BSC1, however at the westernmost section (BSC4) reversals occur multiple times per year, likely due to passing eddies. In fact, monthly mean volume transport at BSC4 ranges between -15 to 26 Sv.

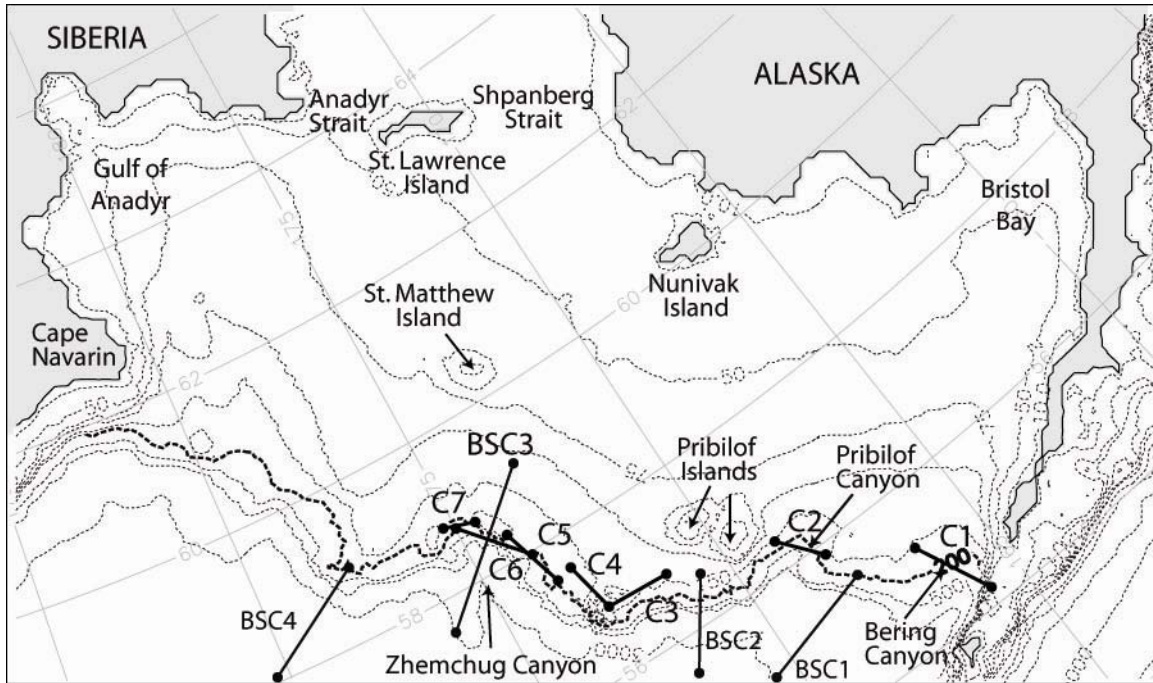


Figure 17. Locations of Bering Slope Current and canyon cross-sections (solid black lines). The location of the 200-m isobath is shown as a thick dashed line.

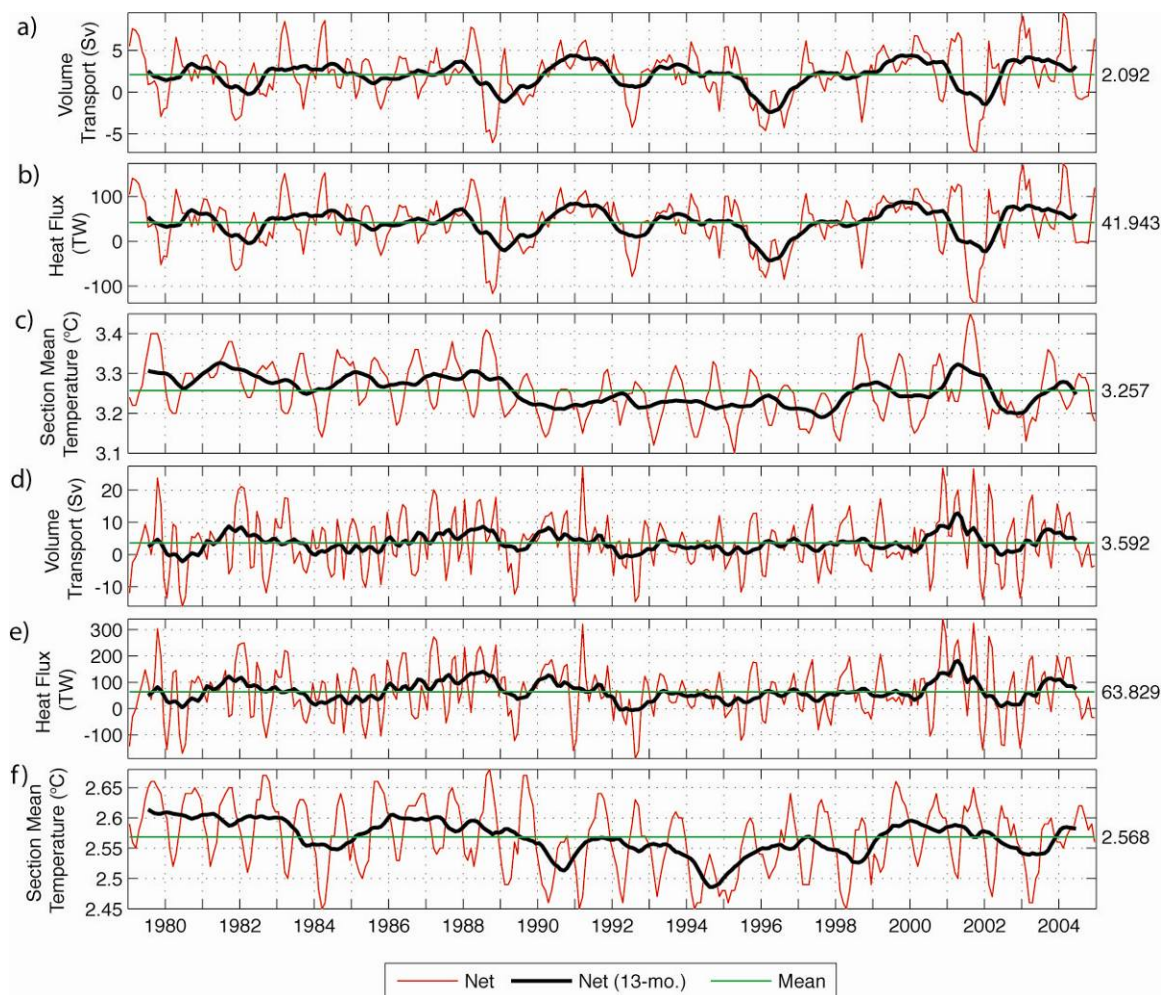


Figure 18. Time series of monthly mean volume transport (a,d), heat flux (b,e) and mean temperature (c,f) across BSC1 (top 3 panels) and BSC4 (lower 3 panels). Heat flux is referenced to -0.1°C . The red line represents monthly mean values, while the thick black line represents a 13-month running mean and the horizontal line represents the 26-year mean. Section locations are shown in Figure 17.

The BSC carries a significant amount of heat (42–64 TW; Figure 18b,e), of which a portion is transported onto the shelf across the slope, as shown in Figure 15b. Volume transport is strongly correlated with heat transport at BSC1 and BSC4 ($r = 0.99$ for monthly mean time series at each section); however, the low-frequency (smoothed) section mean temperature shows a different, somewhat decadal, signal. Section mean temperature was generally above average from 1979–1989 at BSC1 and BSC4. It then

dropped below the 26-yr mean from 1989 to 1998/1999 and has recently been above average. Linkages to large-scale weather indices are examined and discussed in Chapter VIII.

Correlation coefficients for volume transport, heat flux, and mean temperature between the four BSC sections are shown in Table 5. A significant (at the 95% level), but weak correlation exists for both volume transport and heat flux between BSC1 and BSC2, and these correlations become even less as fluxes across BSC1 are correlated with fluxes across sections further west. In fact, the correlations between BSC1 and BSC4 for both volume transport and heat flux are not significant (at the 95% level). This is possibly due to the increased eddy activity in the west, which acts to reduce the correlation with the upstream portion of the current. Another possible explanation for the reduced correlation between time series at eastern and western sections is that sometimes the BSC separates from the shelf break. This separation has been seen in animations of sea surface height, and also velocity throughout 26 years of model results. Over time scales of a few months, the position of the BSC is highly variable, especially in the western Bering Sea, and appears to be related to the formation of eddies just south of the shelf break. This separation from the shelf break is suggested in Figures 13 and 14, where TKE is high (up to $100 \text{ cm}^2 \text{ s}^{-2}$) near the junction of AS3–AS4 and near AS6–AS7. If the BSC separates from the shelf break, conditions at BSC4 are not likely to be similar to conditions at BSC1. Mean temperature is strongly correlated between all BSC sections; however, it is important to note that there is no lag time. This, along with the lack of a strong correlation in volume transport, indicates that the temperature correlation is due to larger-scale basin changes in temperature, instead of an advected signal.

Table 5. Correlation coefficients for volume transport, heat flux, and section mean temperature between Bering Slope Current sections. The number in parenthesis is the lag time in months. The first column (Mo. Mean) for each parameter is the correlation for the monthly mean values. The second column (Annual Cycle Removed) is the correlation after removing the annual cycle. All correlations are significant at the 95% level except for those marked with a *.

Section 1	Section 2	Volume transport		Heat Flux		Mean Temperature	
		Mo. Mean	Annual Cycle Removed	Mo. Mean	Annual Cycle Removed	Mo. Mean	Annual Cycle Removed
BSC1	BSC2	0.32 (0)	0.31 (4)	0.25 (0)	0.31 (4)	0.82 (0)	0.66 (0)
BSC1	BSC3	0.22 (0)	0.16 (0)	0.17 (0)	0.13 (0)	0.80 (0)	0.58 (0)
BSC1	BSC4	0.08* (0)	0.14 (7)	0.08* (0)	0.14 (7)	0.75 (0)	0.45 (0)
BSC2	BSC3	0.32 (0)	0.22 (0)	0.29 (0)	0.20 (0)	0.83 (0)	0.68 (0)
BSC2	BSC4	0.23 (1)	0.20 (1)	0.25 (0)	0.23 (1)	0.75 (0)	0.51 (0)
BSC3	BSC4	0.23 (5)	0.36 (5)	0.27 (5)	0.38 (5)	0.84 (0)	0.65 (0)

A previous study (Clement et al. 2005) addressed the eddy kinetic energy (EKE) of the Bering Sea during 1987 utilizing model results from the same model described herein. Along the BSC, the EKE was 20–100 cm² s⁻² southeast of Zhemchug Canyon, but was significantly higher (80–300 cm² s⁻²) northwest of Zhemchug Canyon. This is in agreement with Okkonen (1993) who found increased eddy activity in the downstream (western) leg of the BSC as compared to the upstream leg. However, it is possible that EKE is even higher in the real ocean, since this model is not yet fully eddy-resolving at 9-km horizontal resolution (Maslowski et al. 2008b).

G. EXCHANGE IN CANYONS AND THE IMPORTANCE OF EDDIES

Figures 15 and 16 indicate that volume transport and property fluxes are locally enhanced near canyons along the Bering Sea slope: Bering Canyon, located on the north side of the Alaska Peninsula, Pribilof Canyon, located south of the Pribilof Islands, and Zhemchug Canyon, located along the shelf break in the central Bering Sea between

171°W and 176°W (see Figure 17 for canyon locations). Circulation and property exchange associated with these canyons is examined in greater detail below.

Twenty-six-year (1979–2004) mean values of volume, heat, salt and freshwater transport through each canyon section are shown in Table 6. In the mean sense, the transport of water and all properties is northward through all of the canyons. However, reversals do occur and may sometimes even show up at the monthly mean time-scale (figures not shown). Because of the relatively strong on-shelf transports of volume, heat, and salt through section C6 (hereafter Zhemchug Canyon), the relationship between conditions in the BSC and exchange through Zhemchug Canyon are examined. Figure 19 shows heat and salt flux anomalies through sections BSC3 and C6 (perpendicular sections whose locations are shown in Figure 17). The two smoothed time series of heat flux anomaly are somewhat correlated, with C6 lagging BSC3 by four months ($r=0.51$, significant at the 90% level). The salt flux anomaly time series are slightly less correlated ($r=0.44$, significant at the 90% level), again with a four-month lag. The salt flux anomaly is highly variable and peaks at over 10 million kg/s during November 1993 (indicated with an open circle on Figure 20d). Based on Figure 20, the increase in salt transported northward onto the shelf in November 1993 is associated with a cyclonic eddy located just south of the canyon section. The eddy has a diameter of 145 km and persists for a period of ~3 months. In addition, three other peaks in the heat and salt flux anomalies are associated with cyclonic eddies (Figure 20). These peaks are represented with stars on the time series in Figure 20cd. A vertical section along the Zhemchug Canyon (BSC3) during the maximum salt anomaly (Nov. 1993) shows the high salinity anomaly core sitting above the slope, with positive salinity anomaly extending onto the shelf (Figure 21a). A section across Zhemchug Canyon (Figure 21b) shows that the salinity anomaly is positive near the surface (up to 0.12 psu) and also near the bottom (up to 0.18 psu), with the flow directed on-shelf. These figures show how the eddy is responsible for upwelling relatively salty water onto the central Bering Sea shelf. Focusing on the deeper water (>100m; where salinity can be used as a proxy for nutrients), one can say that this eddy accounted for a total of 28.6 trillion kg of salt being upwelled onto the shelf through the Zhemchug Canyon section during its three-month

lifetime. If the entire water column is included, then 107 trillion kg of salt was transported onto the shelf through Zhemchug Canyon during the same three-month period.

Table 6. Twenty-six-year mean (1979–2004) volume transport (Sv), salt flux (million kg/s), freshwater flux (mSv; relative to 34.8), and heat transport (TW; relative to -0.1°C) for canyon sections. Numbers in parenthesis represent standard deviation.

Section	Volume transport	Salt flux	Freshwater flux	Heat flux
C1	0.206 (0.084)	6.601 (2.705)	15.842 (6.495)	5.245 (2.892)
C2	0.009 (0.080)	0.281 (2.579)	0.679 (6.120)	0.556 (1.505)
C3	0.083 (0.087)	2.682 (2.799)	6.198 (6.492)	1.261 (1.593)
C4	0.135 (0.053)	4.357 (1.717)	9.839 (3.840)	2.501 (1.233)
C5	0.110 (0.071)	3.556 (2.303)	7.895 (5.122)	2.035 (1.444)
C6	0.195 (0.112)	6.284 (3.616)	13.927 (7.976)	3.550 (2.369)
C7	0.055 (0.056)	1.782 (1.812)	3.960 (3.988)	1.004 (1.010)

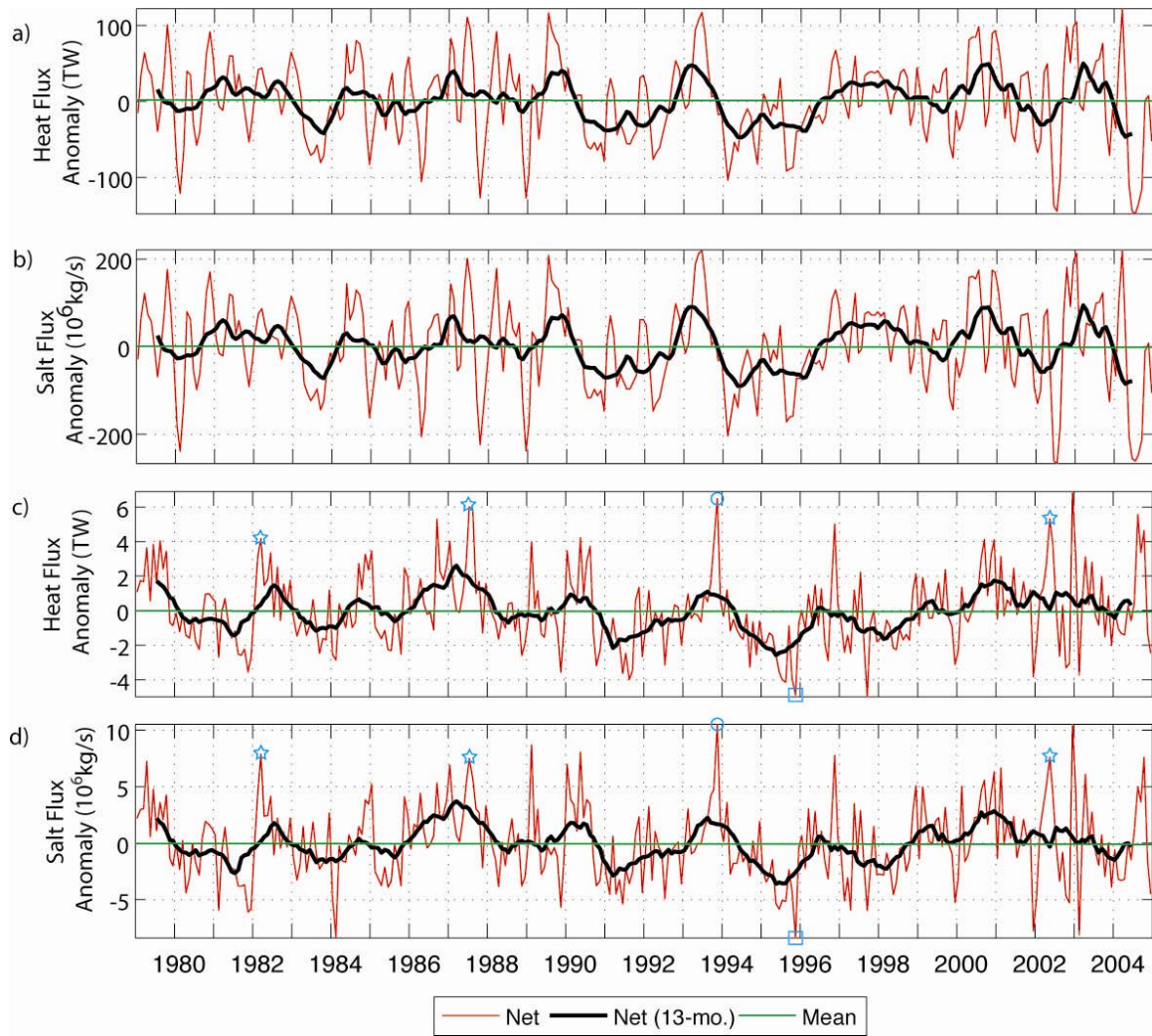


Figure 19. Time series of monthly mean heat (a,c) salt (b,d) flux anomaly across BSC3 (a,b) and the Zhemchug Canyon section (C6; c,d) shown in Figure 17. The red line represents monthly mean values, while the black line represents a 13-month running mean and the horizontal green line represents zero. The circles and squares represent the salt and heat flux maximum (November 1993) and minimum (November 1995), respectively through Zhemchug Canyon. The stars represent local peaks in the heat and salt flux anomaly through Zhemchug Canyon associated with eddies shown in Figure 20.

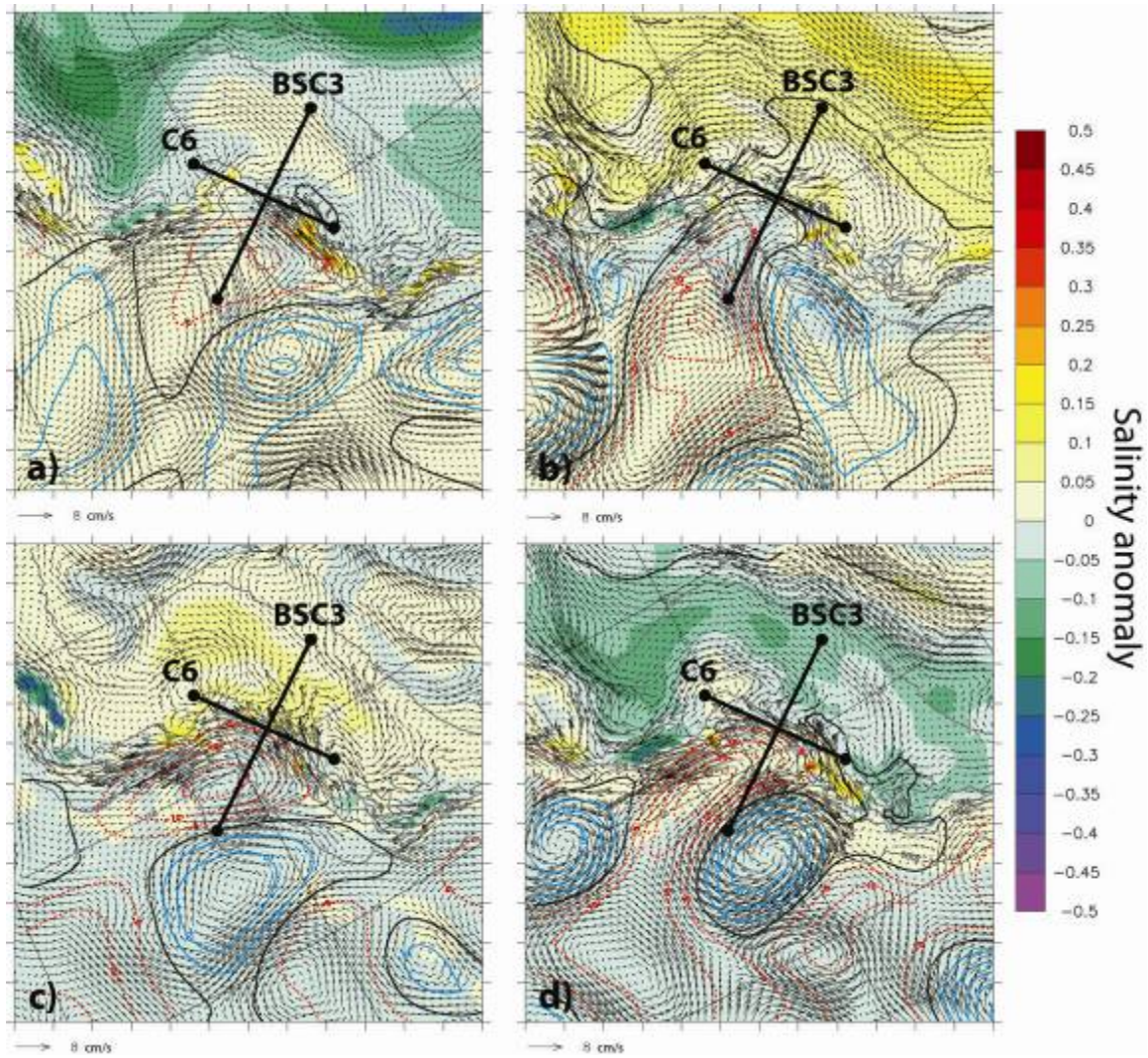


Figure 20. The bottom water salinity anomaly and sea surface height anomaly contours (blue is positive and red is negative; contour interval of 5 cm) during (a) March 1982, (b) July 1987, (c) November 1993, and (d) May 2002 in the vicinity of Zhemchug Canyon. The vectors represent monthly mean velocity over the entire water column during each respective month.

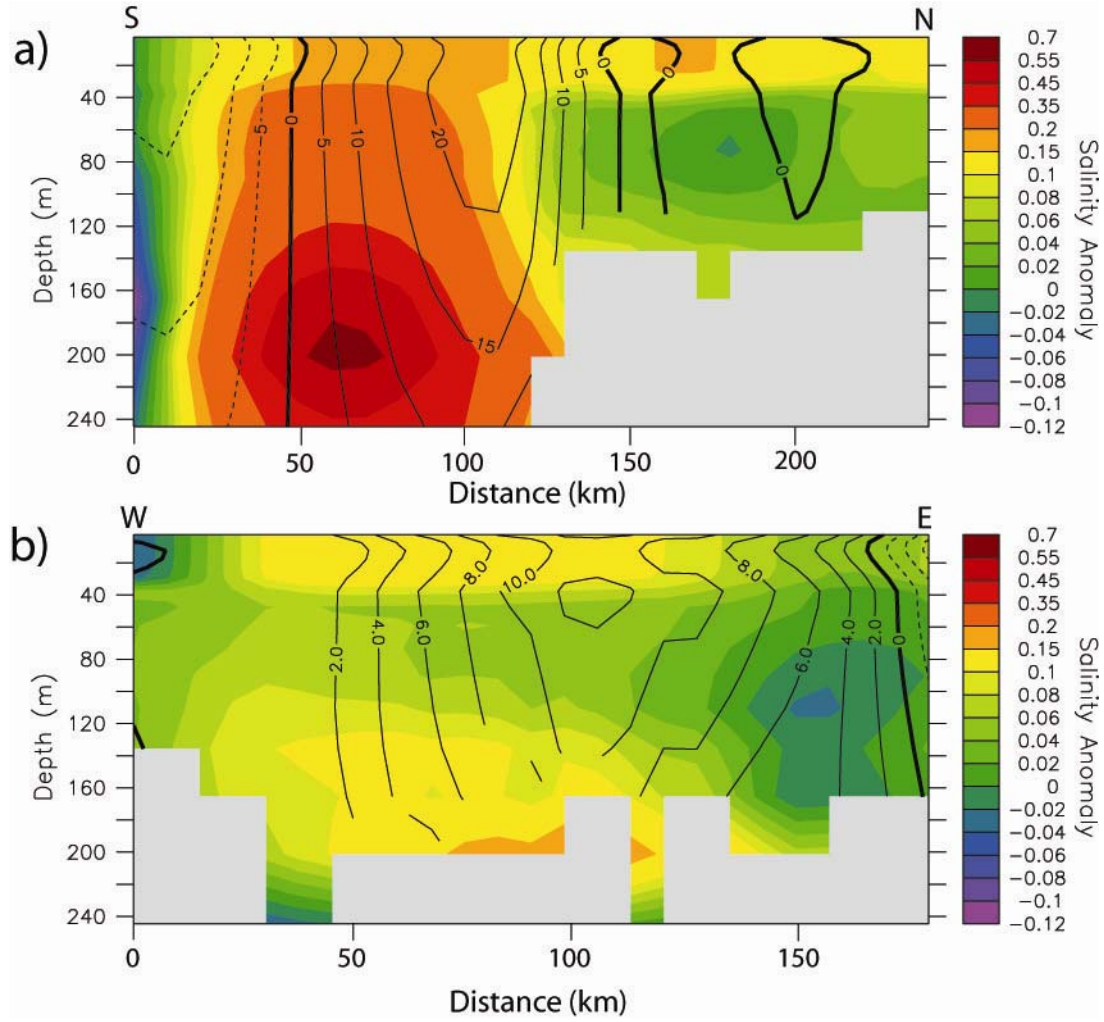


Figure 21. The vertical section of velocity (contours; cm/s) and salinity anomaly (shading) (a) along the Zhemchug canyon (section BSC3), and (b) cross the Zhemchug canyon (section C6) during November 1993.

The contribution of a transient motion (e.g., an eddy) to the time-averaged flux across a particular section can be quantified according to:

$$\bar{F} = \int (\overline{uc}) dA \quad (2)$$

where \bar{F} is a temporal mean flux (26-yr annual cycle; 1979–2004), $\int (...) dA$ is the area integral across the section, u is the normal component of velocity and c is the quantity being advected. Anomalies from the temporal mean are defined as:

$$\begin{aligned} u' &= u - \bar{u}; \\ c' &= c - \bar{c} \end{aligned} \quad (3)$$

Taking Equations (2) and (3) together gives:

$$\bar{F} = \int (\bar{u}\bar{c}) dA + \int (\overline{u'c'}) dA \quad (4)$$

The perturbations, u' and c' , should be derived from instantaneous measurements of u and c ; or in the case of model results, calculated based on high frequency temporal snapshot results. To make a fair calculation of the eddy transports, it would be best to use means (for u and c) that are daily, if not over a shorter time period. However, the model results are not available in three dimensions as daily means, due to storage limitations. Therefore, the monthly means must be used for calculating perturbation values. For the means (\bar{u} , \bar{c}), the 26-year annual cycle monthly means (e.g., mean Jan. over 26 years) are used. Transient motions contribute to the mean flux if u' and c' are correlated. The correlation coefficient between u' and S' across Zhemchug Canyon section was 0.32, while the correlation coefficient between u' and T' was 0.20. Both correlations were significant at the 99% level ($p=0.01$). The fractional contribution of eddy transports to the mean flux, \bar{F} , was small for both heat and salt flux ($< 8\%$). It is believed that the weak correlations and small eddy contributions to the mean flux are largely due to the fact that monthly means are used for calculation of perturbation values, which smooth out the short-lived perturbations (Marble 2001). This calculation does not fully quantify the eddy contribution to the mean flux; however, it is the best that can be made with the available model output. It is still apparent that eddies are responsible for several peaks in the heat and salt flux anomalies as shown in Figures 19–21.

Hovmuller plots of near-bottom salinity and temperature anomaly (after removing the annual cycle) for 1979–2004 show significant interannual and spatial variability along the 200-m isobath (Figure 22). Zhemchug Canyon experiences frequent events, likely due to strong eddy activity, in comparison to Bering Canyon, which is more consistent. Overall, the temperature and salinity anomalies tend to be the same sign (either negative or positive) along the entire length of the 200-m isobath; however, this is not always true.

For instance during 1987, temperature and salinity anomalies were negative in the west (0–400 km), with mainly positive anomalies in the east. When looking over longer time scales, the temperatures were warmer, especially in the west during the 1980s, followed by a drop in the early 1990s. Recently, however, temperatures along the slope have increased. Salinity anomalies show some temporal similarities with temperature anomalies. Decreased salinity anomalies were present over the slope during the 1990s and increased in 2001. However, unlike temperature anomalies, the salinity was relatively low in the 1980s. There is also a suggestion of propagating features in these figures, possibly planetary waves or eddy propagation, which would be a topic for a later paper.

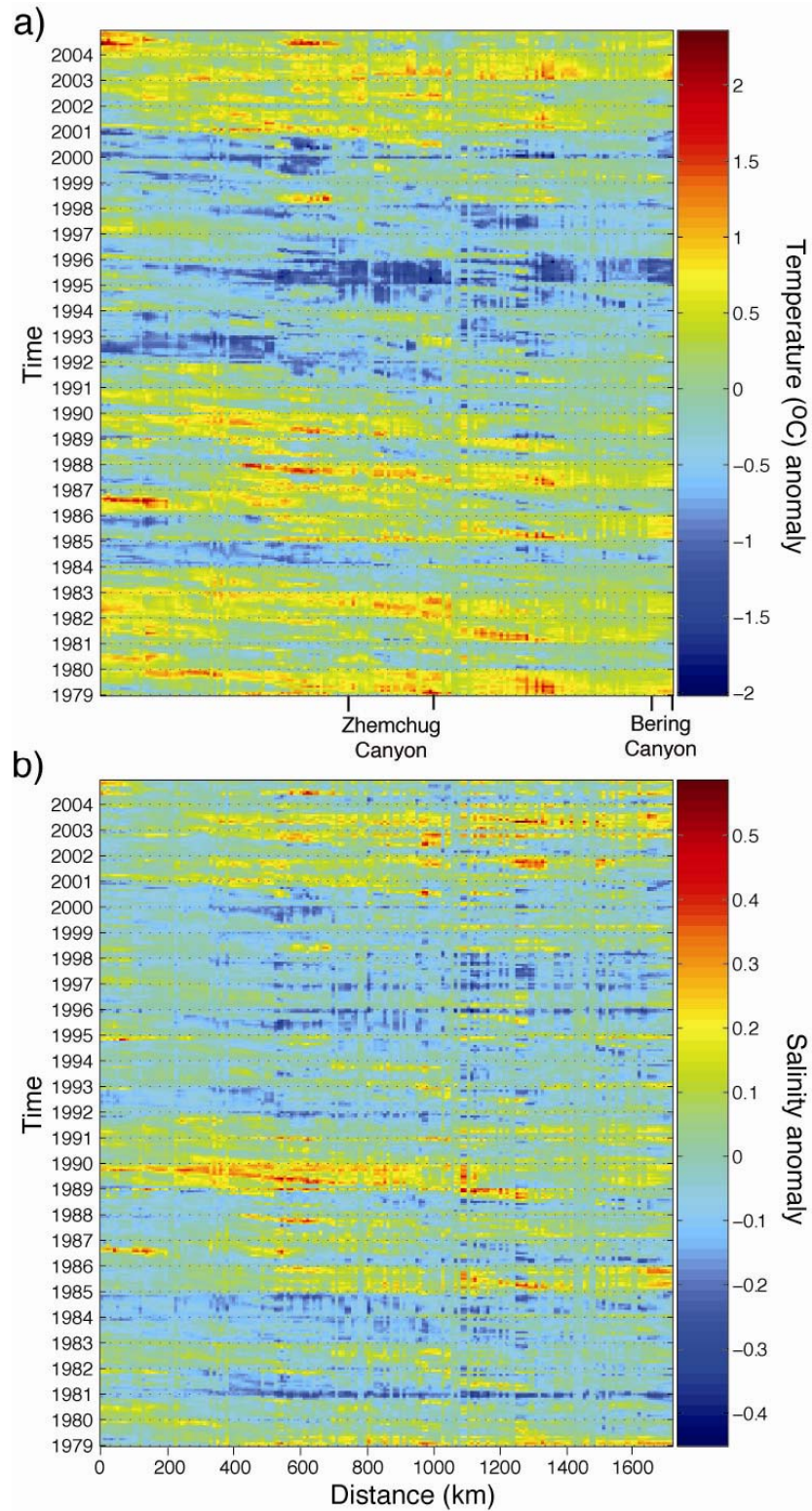


Figure 22. Hovmuller plot of temperature anomaly ($^{\circ}\text{C}$; a) and salinity anomaly (b) along the Bering Sea 200-m isobath.

H. CONCLUSIONS

The flow across the Bering Sea shelf is up to 3 cm/s in the mean sense and is highest near 60°N between St. Matthew and Nunivak islands. This area of strengthened flow is centered on and follows isobaths between 50 and 75 m. As expected, the strongest flow on the shelf is Anadyr Current to the west, which carries water toward Anadyr Strait at a mean speed of approximately 3–10 cm/s, depending upon the location. Several regions along the slope (especially certain canyons) that are important in shelf basin exchange also show up in the long-term mean circulation scheme (Figure 13).

In the model results, the BSC appears to be more a system of eddies rather than a continuous current, which emphasizes the need for a fully eddy-resolving, basin-wide model to represent its complex dynamics. Okkonen (1993) identified a representative eddy period as ~4 months. This time period is similar to modeled high frequency signals in the volume transport and heat flux at BSC4 (Figure 18d, e), as well as the heat and salt flux anomalies at BSC3 (Figure 19). The lack of correlation between various sections along the BSC, along with snapshots of SSH indicating frequent, multiple eddies (not shown), provide additional evidence for this conclusion.

There is little evidence for a north-south splitting of the BSC near Cape Navarin (Figure 13). Instead the majority of the BSC turns southwestward upon nearing the coast in the long-term mean model results. There is evidence of a coastal current flowing northeastward around Cape Navarin, however it is not derived of BSC water. According to the model results the main source of water for the Gulf of Anadyr comes from the outer shelf flow, roughly between the 100 and 200-m isobaths.

Paluszkiwicz and Niebauer (1984) and Okkonen et al. (2004) have suggested that topographic planetary waves generate eddies seen along the Bering slope. The modeled eddy described herein had a diameter of 145 km and lifetime of ~90 days. This is similar in size and duration to eddies observed by Paluszkiwicz and Niebauer (1984; 140 km / 84 days) and Okkonen (1993; 184 km / 72 days). Frequent eddies, such as the one described herein, may be important for transporting salt onto the Bering Sea shelf. However, if three-dimensional daily mean fields had been available to correlate velocity

and salinity along the Zhemchug Canyon section, instead of monthly means, this might have allowed a more quantitative statement to be made. On-shelf transport appears to be enhanced by the presence of canyons along the Bering Sea slope (Figures 15a, 16).

THIS PAGE INTENTIONALLY LEFT BLANK

VI. CIRCULATION AND ENERGETICS OF THE NORTHERN BERING SEA

A. INTRODUCTION

This chapter aims to quantify the long-term mean and variability of the circulation at time scales ranging from months to decades across the data-limited northern Bering Sea and through Bering Strait using the NPS pan-Arctic coupled ice-ocean model. One of the specific objectives in this study was to improve understanding of the flow and transports through Anadyr, Shpanberg, and Bering Straits (locations shown in Figure 23). Model results on the EKE are also provided to indicate regions of active horizontal and vertical mixing, which is a biologically important process. These two topics are geographically related within the northern Bering Sea and are part of a publication by Clement et al. (2005).

B. VOLUME TRANSPORT THROUGH ANADYR AND SHPANBERG STRAITS

In order to determine the characteristics of water flowing through Bering Strait, it is important to consider upstream conditions. Model results show that water from Anadyr Strait contributes 80% of the mean flow (23-year mean = 0.52 Sv) into the Chukchi Sea. The wider, but shallower Shpanberg Strait contributes only 0.13 Sv or 20% of the mean flow through Bering Strait and is primarily made up of relatively sluggish Alaska Coastal Water and Bering Shelf Water. It is worth noting that not all of the water flowing through Anadyr Strait is associated with the Anadyr Current. Instead some water moving northward on the northern Bering shelf also can go west around St. Lawrence Island through Anadyr Strait to reach Bering Strait. Overland and Roach (1987) used a two-dimensional barotropic model to investigate the Bering Strait transport and circulation patterns of the northern Bering Sea. They found that in their 18-km grid in the absence of wind, Anadyr Strait contributed 72% of the northward transport that would eventually enter the Chukchi Sea via Bering Strait. Historic current meter measurements during

summer and fall from 1985–1988 indicate that the split between Anadyr/Shpanberg straits is typically 30/70%, respectively (Coachman 1993).

Since the majority of Bering Strait throughflow is associated with the Anadyr Current, it is important to observe the characteristics of this water. However, most of Anadyr Strait lies in Russian territorial waters and international research efforts have been significantly limited in this area. Additional scientific efforts and field observations including long-term moorings in the Gulf of Anadyr and on the western side of Bering Strait, would be critical for determining the characteristics of the Pacific inflow into the Chirikov Basin north of St. Lawrence Island and eventually into the Arctic Ocean through the Bering Strait. Such data would allow further validation and constraining of ocean models for climate study.

C. ANOMALOUS CIRCULATION EVENT

Time series of the volume transport through five cross-sections (locations shown in Figure 23) are shown in Figure 24. Over 23 years, the sections show seasonal, as well as interannual, variability in flow across the northern Bering shelf. The net 23-year mean volume transport across Bering Strait is 0.65 Sv, with 0.72 Sv moving northward and a slight but annually regular component (0.07 Sv) moving southward. An annual minimum of 0.48 Sv was reached in 1994 and a maximum of 0.78 Sv in 1979, thus giving an interannual variability of approximately ± 0.15 Sv. A similar estimate of ± 0.2 Sv was made by Coachman (1993) based on observational studies during the Inner Shelf Transfer and Recycling in the Bering and Chukchi Seas (ISHTAR) program. Net monthly mean variation in transport is greater than 1 Sv, with a low of 0.11 Sv in December 1997 and a high of 1.28 Sv in August 1999. Examination of instantaneous transports across Bering Strait (calculated every model time-step of 480 s) reveals even stronger wind-driven variability, from 2.7 Sv northward to 2.5 Sv southward (data not shown).

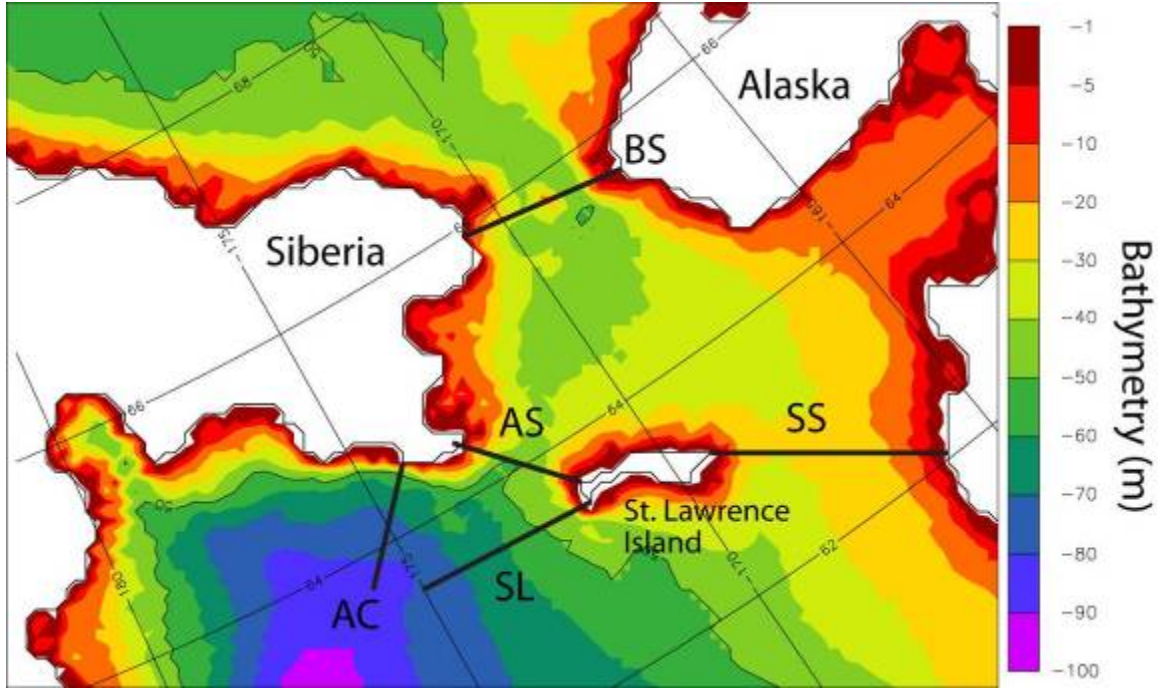


Figure 23. Bathymetry (m) of the northern Bering Sea and locations of cross-sections (thick black lines): BS (Bering Strait), AS (Anadyr Strait), SS (Shpanberg Strait), AC (Anadyr Current), and SL (St. Lawrence Island). The direction of positive flow is northward across BS and SL, northeastward across AS and SS, and eastward across AC.

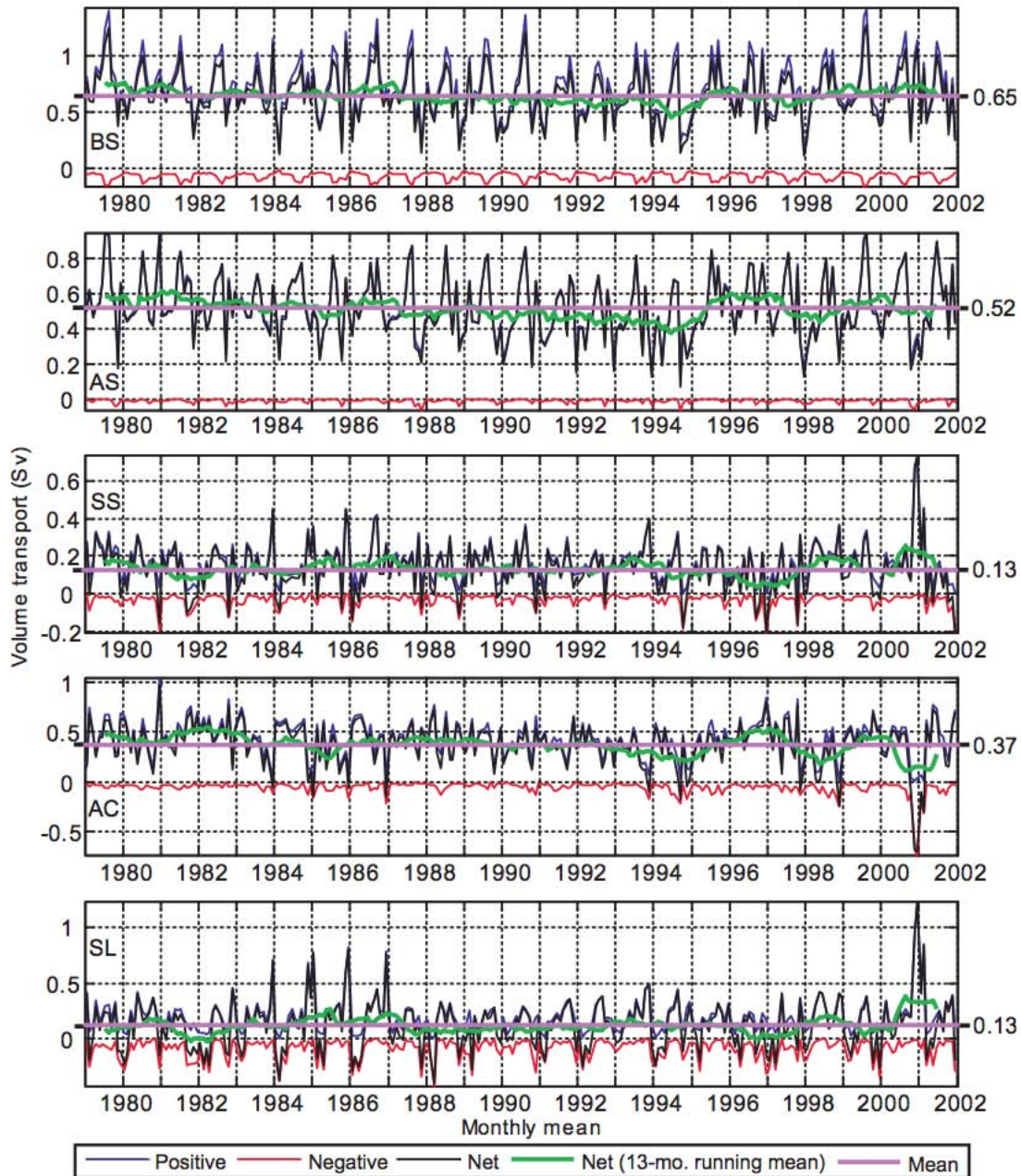


Figure 24. Monthly mean volume transport over a 23-year time series (1979–2001). Positive fluxes represent flow to the north or east according to the model grid (see Figure 23), while negative fluxes represent flow to the south or west. The smoothed net flux (thick green line) is a 13-month running mean. The 23-yr mean is shown at the end of each time-series.

With respect to other sections, SS, AC, and SL all had numerous negative monthly mean minima representative of flow reversals (Figure 24). The most notable flow reversal (up to 0.70 Sv) in the 23-year time series occurred along the AC section during November and December 2000. Flow continued to be westward across the northwestern Bering Sea until March 2001. This episode was also evident in the AS, SS, and SL sections, with greatly increased northwestward flow across the northern Bering shelf. This event also coincided with observations of reduced sea ice conditions during winter of 2000–2001 (Figure 25). Observations mainly derived from satellite data during February 1999 and 2001 show that ice concentrations were very low during 2001 as compared to a more typical year, 1999 (Figure 25a,b; Clement et al. 2004). The model shows a similar ice distribution in the two years, except for slightly lower ice concentrations (80–95%) instead of solid >95% ice cover reported during February 1999 (Figure 25c,d). These areas of slightly reduced ice cover concentrations in the model might be representative of the realistic presence of leads not observed by the U.S. National Ice Center. The strong flow reversal, which peaked in November and December 2000, and northwestward movement of sea ice occurred relatively quickly over the course of a few months during winter 2000–2001. The cause of this event is most likely wind forcing, as shown in Figure 26. While previous studies indicate that prevailing winds are out of the north to slightly northeast in the northern Bering Sea during winter (Muench and Ahlnäs 1976; Pease 1980; Overland 1981), a very different scenario took place during winter 2000–2001. Figure 26 depicts the ECMWF wind forcing fields used in the model averaged over the 2-month peak in flow reversal (November and December 2000) as compared to the more typical year (November and December 1998). In 1998, wind was out of the north with speeds of 3–4 m/s in the vicinity of Bering Strait and up to 4.5 m/s south of St. Lawrence Island. In contrast, during 2000 much stronger wind speeds of 5–6.5 m/s occurred near Bering Strait, with speeds up to 9.3 m/s in the Gulf of Anadyr. The average magnitude difference between 1998 and 2000 winter winds (Figure 26C) was 3.0 m/s and the wind direction was shifted an average of 43° to a more easterly pattern in 2000. Observational measurements from this time period corroborate an unusual wind and resulting ice cover pattern in winter 2000–2001 (Clement et al. 2004).

The dramatic response in sea ice and ocean conditions to this weather pattern suggests that wind is the dominant forcing mechanism in the northern Bering Sea. The wind forcing drove an Ekman transport on the shelf that resulted in an Anadyr Current flow reversal, as well as greatly increased northward transport across Shpanberg Strait.

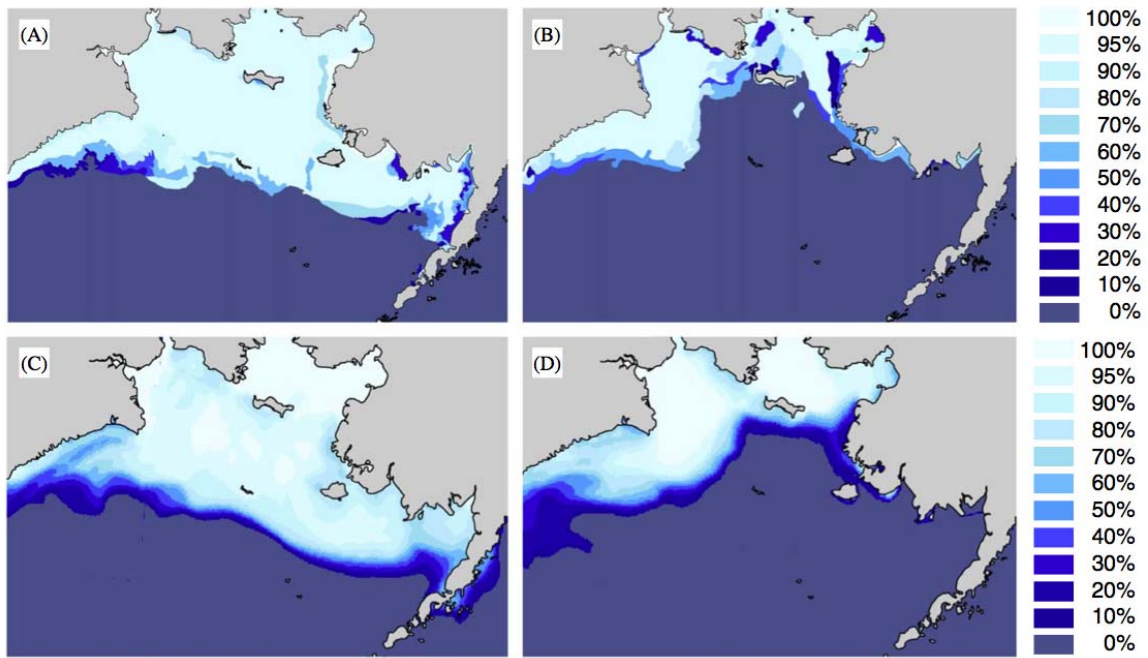


Figure 25. Sea ice concentration on (A) February 19, 1999 and (B) February 19, 2001 as determined using data obtained from the U.S. National Ice Center (adapted from Clement et al., 2004). Model monthly mean sea ice concentration during (C) February 1999 and (D) February 2001.

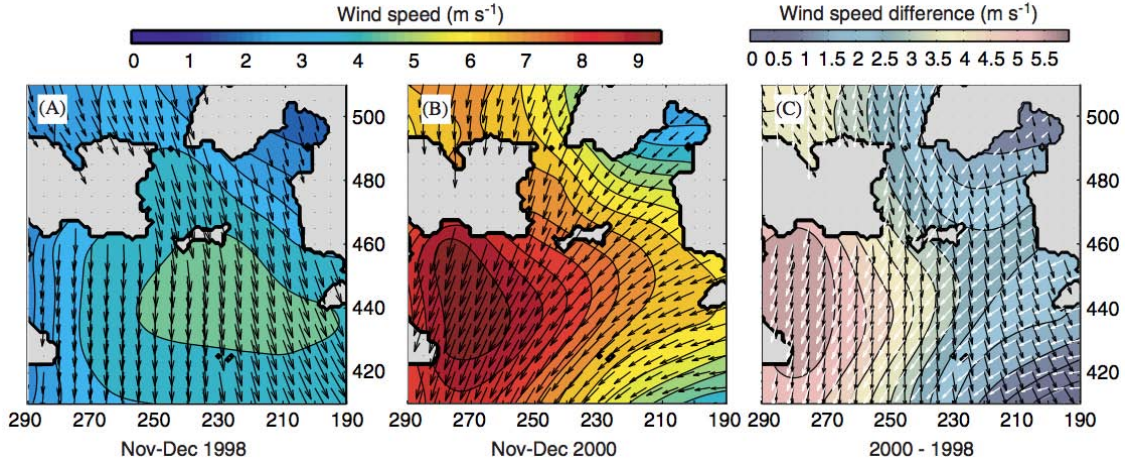


Figure 26. Model wind forcing fields averaged over November and December (A) 1998 and (B) 2000. (C) The magnitude difference (2000–1998) and both wind fields (1998 in black; 2000 in white).

D. EDDY KINETIC ENERGY

With a horizontal grid cell spacing of approximately 9 km, this model is able to resolve eddies with diameters as small as 36 km. As such, the eddy kinetic energy (EKE) distribution in the Bering Sea has been examined, as calculated from daily fluctuations (u', v') referred to the 23-year mean. EKE is an important model parameter, which, in the physical world, commonly represents regions of active mixing and associated increased biological productivity. Realistic representation of EKE in a model is often challenging but when achieved can provide useful information about the dynamics and productivity in a region. Observational estimates of EKE on the Bering shelf are not readily available, hence the following discussion serves to establish a quantitative, yet due to the need for even higher model spatial resolution, possibly incomplete reference. Results described below use either the surface level (0–5 m) or a subsurface level (20–26 m) as indicated. The year 1987 was chosen because it characterized an average transport through Bering Strait and it did not appear strongly biased toward any particular climate regime in the North Pacific or Arctic Ocean. The mean velocity components for 1979–2001, were calculated and then subtracted from the 1987 daily velocity values to obtain u' and v' :

$$u' = u_d - u_m, \quad v' = v_d - v_m \quad (5)$$

where u_d and v_d represent the daily velocity components and u_m and v_m represent the long-term (1979–2001) mean velocity components. From this the EKE can be calculated as:

$$EKE = \frac{(\overline{u'^2} + \overline{v'^2})}{2} \quad (6)$$

It is important to note that high EKE values indicate not only the presence of eddies, but also indicate any fluctuation around the mean velocity field.

Seasonal changes in EKE in the surface layer are visible across the Bering shelf, with highest values in autumn and winter (Figure 27). Bering and Anadyr straits maintain relatively high EKE throughout the year, but peak during autumn. The area directly south of St. Lawrence Island is also a region of increased EKE, while north of the island in the Chirikov Basin a distinct decrease is observed. Below the surface at 20–26 m depth, there is a sharp decrease in EKE across the middle shelf (Figure 28). Again, the EKE in the northern straits and along the BSC remains elevated.

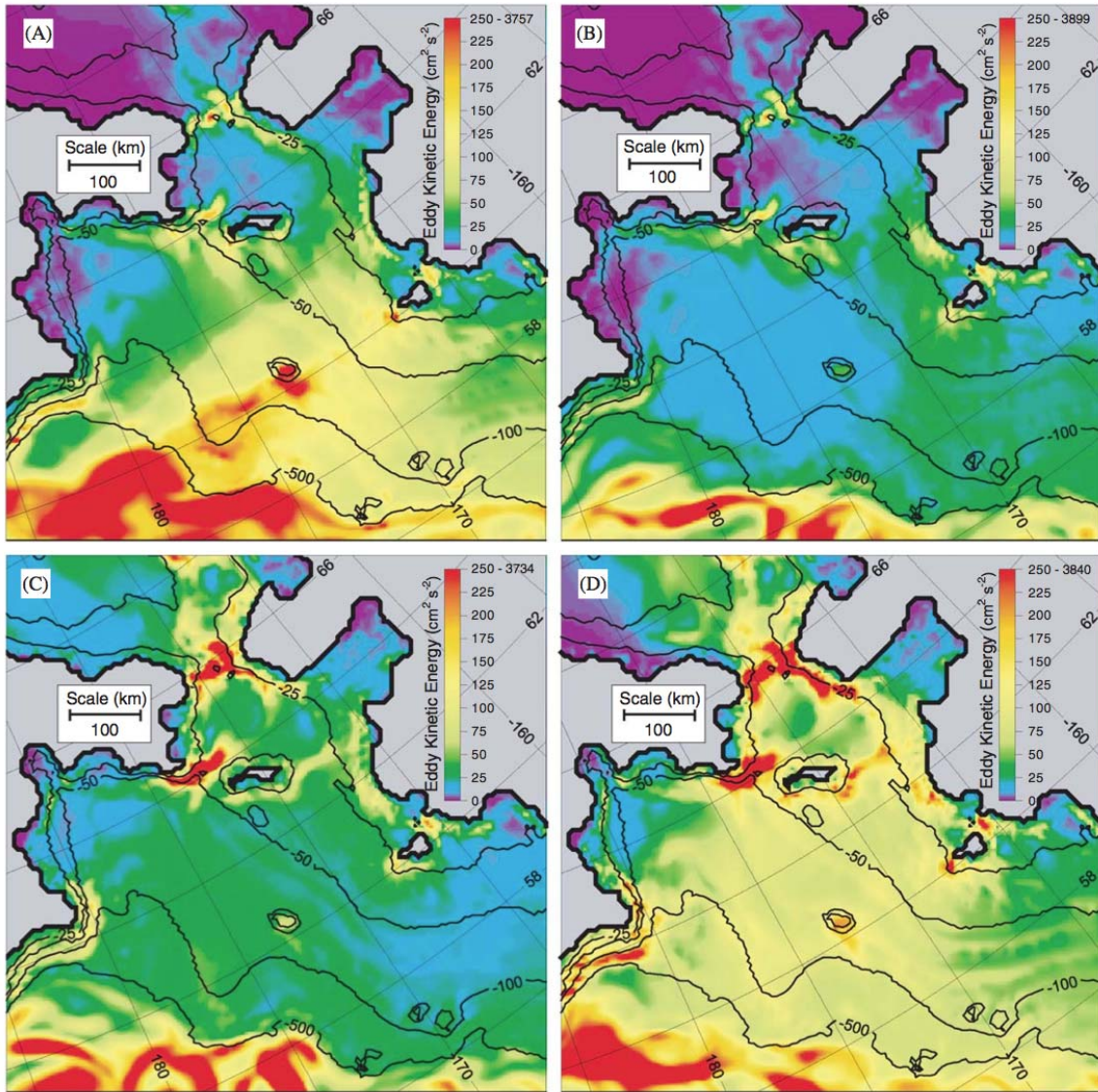


Figure 27. Seasonally average EKE at the surface (0–5 m) calculated from daily 1987 snapshots (against the 23-year mean; 1979–2001): (A) Winter (J-F-M) average, (B) Spring (A-M-J) average, (C) Summer (J-A-S) average, and (D) Autumn (O-N-D) average.

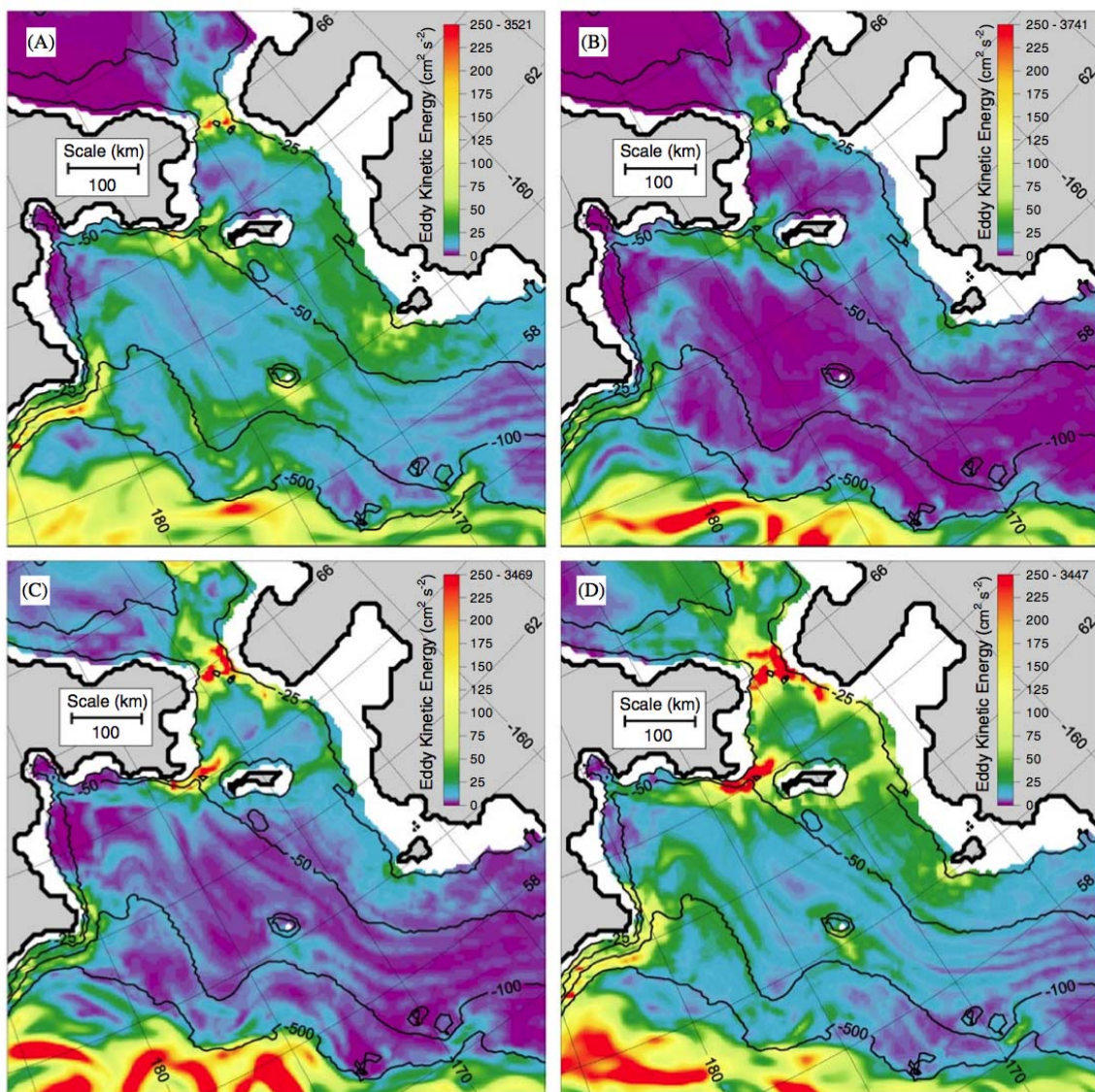


Figure 28. Seasonally average EKE at 20–26 m calculated from daily 1987 snapshots (against the 23-year mean; 1979–2001): (A) Winter (J-F-M) average, (B) Spring (A-M-J) average, (C) Summer (J-A-S) average, and (D) Autumn (O-N-D) average.

E. CONCLUSIONS

Model results indicate that water from Anadyr Strait contributes 80% of the mean flow into the Chukchi Sea via Bering Strait. The remainder of the northward flow through Bering Strait (20%) comes from the eastern side of the northern Bering Sea shelf via Shpanberg Strait. More observations of the flow through Anadyr Strait are needed, since it provides the majority of the Bering Strait throughflow; however, this is complicated by a political boundary (the Russian EEZ), which has historically restricted US access and limited international collaboration.

Time-series of volume transport show that the model is able to represent anomalous events, such as major flow reversals, which are corroborated by observations. Wind appears to be the dominant force driving water and ice movement across the northern Bering Sea at synoptic to interannual time scales. In addition to wind forcing, it is also important to consider buoyancy forcing along the Alaska coast, however this model is not able to fully resolve the narrow Alaska Coastal Current.

EKE fields show that the northern Bering Sea maintains year-round high energy and significant horizontal and vertical mixing, especially in Bering and Anadyr straits. The highest energy levels occur during autumn and winter throughout the shelf, coincident with observations of increased storminess during those seasons (Overland 1981; Overland and Pease 1982; Stabenro et al. 1999). Possible effects of these EKE fields on biological processes are discussed in Chapter IX.

THIS PAGE INTENTIONALLY LEFT BLANK

VII. THE FLOW THROUGH BERING STRAIT

A. INTRODUCTION

The Pacific Arctic Region spans the sub-Arctic Bering Sea northward through the Chukchi and Beaufort seas and the Arctic Ocean. A narrow passageway, the Bering Strait, connects the wide and shallow shelves of the Bering and Chukchi seas. The Bering Strait is the only Pacific connection to the Arctic Ocean. The narrow (~85 km wide) and shallow (~50 m deep) strait provides low-salinity and high-nutrient Pacific Water to the Chukchi Sea and the Arctic Ocean. Many global and regional models face challenges with resolving oceanic exchanges across this narrow and shallow strait, mainly due to the requirement of high spatial resolution and the associated high computational cost to resolve it. In fact, many coarse-resolution models either have a closed Bering Strait or use a prescribed boundary condition. For example, Goosse et al. (1997) demonstrated a significant improvement in modeled ocean dynamics in a coarse resolution ($3^{\circ} \times 3^{\circ}$) model with an opened Bering Strait. They also found that opening Bering Strait produced a more realistically positioned sea ice edge in the Bering Sea, because warm water was allowed to advect further north onto the Bering-Chukchi shelf. Arctic freshwater budgets were also improved, with increased freshwater storage in the Greenland and Norwegian Seas.

Scientific access across Bering Strait has been restricted due to the political boundary between the United States and Russia. The Russian-US Convention line, dividing the Exclusive Economic Zones (EEZs) of the two countries, lies between two islands near the center of the strait: Ratmanova Island (part of Russia, also called Big Diomedes in the U.S.) and Little Diomedes Island (part of the U.S.). While U.S. research has maintained moorings in the Bering Strait almost continuously since 1990, only for limited portions of that time has U.S. access been granted to the western side of the strait.

The main goal of this work is to analyze output on the Bering Strait throughflow from several state-of-the-art regional and global Arctic-focused models and to compare model results against the available limited observational data. The volume and property

fluxes will be analyzed over a long time series (up to 26 years depending on available results from individual models). In addition to interannual changes, annual cycles in these parameters will also be examined. Data are from moored instruments placed near-bottom in three point locations in the vicinity of the strait (Figure 29a). Both observations and modeling have their own limitations in Bering Strait. Numerical models are limited by relatively coarse resolution in the strait, errors in forcing and omitted processes (e.g., tides), whereas observational results are limited by spatial coverage across the strait, and lack of upper layer measurements.

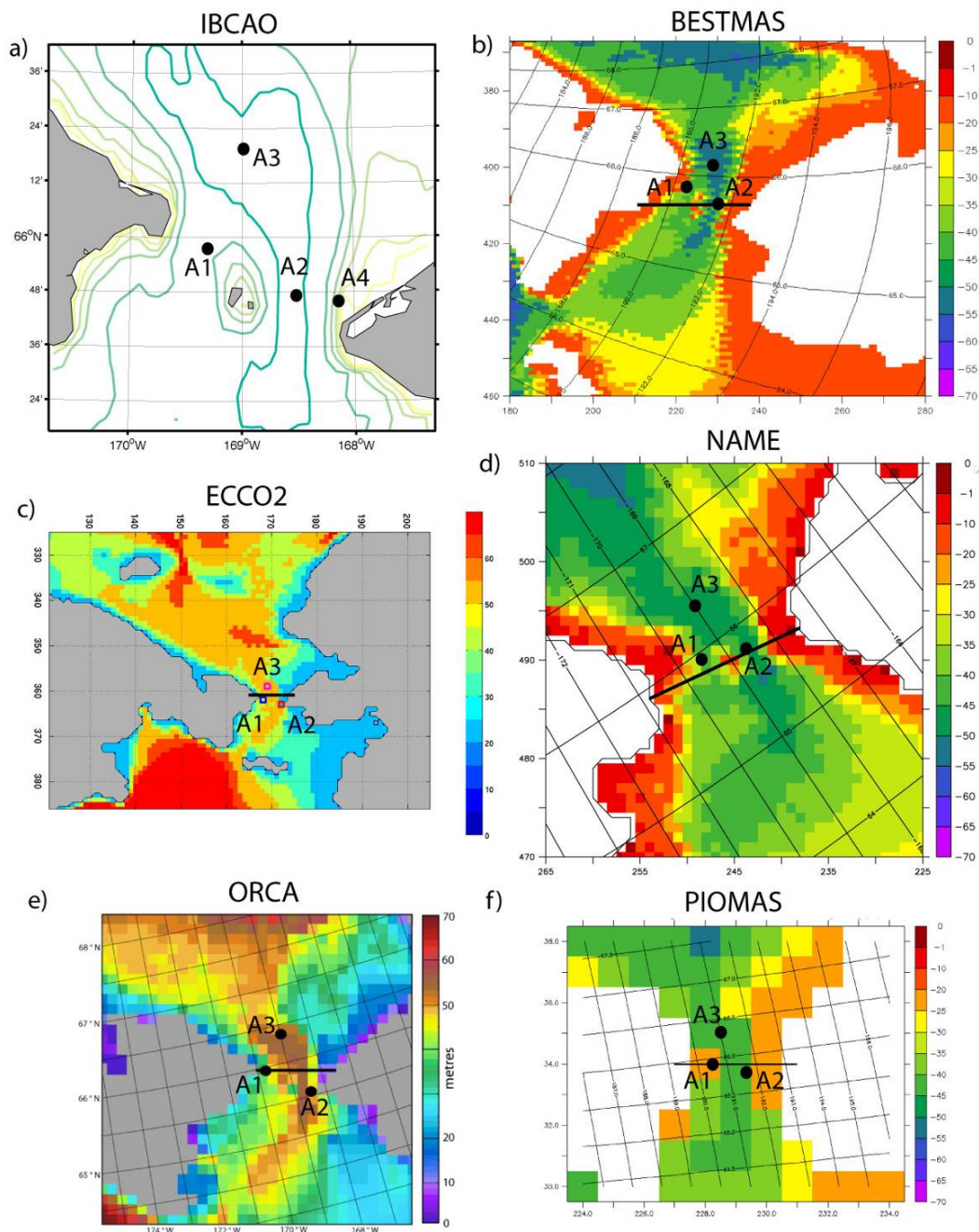


Figure 29. Bathymetry (m) in the vicinity of the Bering Strait (a). Depth contours are every 10 m from the International Bathymetric Chart of the Arctic Ocean (Jakobsson et al. 2000). Model bathymetry (m) from (b) BESTMAS, (c) ECCO2, (d) NAME, (e) ORCA, and (f) PIOMAS. The approximate locations of the moored observations are indicated with black circles. The cross-sections across Bering Strait are shown as black lines in each model bathymetry figure. Different orientations in figures b-f are due to different coordinate systems used in each model.

B. MODEL DESCRIPTIONS

In this section, important aspects of five global and regional sea ice-ocean coupled models are described. Results from each of these models were provided to the author in order to investigate Bering Strait inflow (Table 7).

Table 7. Basin information on the five models used in this study.

Model	Global/Regional	Atmospheric Forcing	Resolution in Bering Strait
BESTMAS	regional	NCEP/NCAR reanalysis	~7 km
ECCO2	regional	Japanese 25-year reanalysis	~18 km
NAME	regional	ECMWF reanalysis	~9 km
ORCA	global	DRAKKAR Forcing Set (DFS 3.1) reanalysis	~13 km
PIOMAS	regional	NCEP/NCAR reanalysis	~22 km

1. Bering Ecosystem STudy Ice-Ocean Modeling and Assimilation System (BESTMAS)

BESTMAS (Zhang et al. 2010) is based on the coupled Parallel Ocean and sea Ice Model (POIM) of Zhang and Rothrock (2003). The sea ice model is the multicategory thickness and enthalpy distribution (TED) sea ice model (Zhang and Rothrock 2001; Hibler 1980). It employs a teardrop viscous-plastic rheology (Zhang and Rothrock 2005), a mechanical redistribution function for ice ridging (Thorndike et al. 1975; Hibler 1980), and a LSR (line successive relaxation) dynamics model to solve the ice momentum equation (Zhang and Hibler 1997). The TED ice model also includes a snow thickness distribution model following Flato and Hibler (1995). The ocean model is based on the Parallel Ocean Program (POP) developed at Los Alamos National Laboratory (Smith et al. 1992; Dukowicz and Smith 1994). Given that tidal energy accounts for 60–90% of the total horizontal kinetic energy over the southeastern shelf region of the Bering Sea (Kinder and Schumacher 1981), tidal forcing arising from the eight primary constituents (M2, S2, N2, K2, K1, O1, P1, and Q1) (Gill 1982) is incorporated into the POP ocean model. The tidal forcing consists of a tide generating potential with corrections due to both the earth tide and self-attraction and loading following Marchuk and Kagan (1989).

The model domain of BESTMAS covers the northern hemisphere north of 39°N. The BESTMAS finite-difference grid is based on a generalized orthogonal curvilinear coordinate system with a horizontal dimension of 600×300 grid points. The “north pole” of the model grid is placed in Alaska. Thus, BESTMAS has its highest horizontal resolution along the Alaskan coast and in the Bering, Chukchi, and Beaufort seas, with an average of about 7 km for the whole Bering Sea and 10 km for the combined Chukchi and Beaufort seas. There are 20 grid cells across Bering Strait (Figure 29b), which allows a good connection between the Bering Sea and the Arctic Ocean. The TED sea ice model has eight categories each for ice thickness, ice enthalpy, and snow depth. The centers of the eight ice thickness categories are 0, 0.38, 1.30, 3.07, 5.97, 10.24, 16.02, and 23.41 m. The POP ocean model has 30 vertical levels of varying thicknesses to resolve surface layers and bottom topography. The first 13 levels are in the upper 100 m and the upper six levels are each 5 m thick. The model bathymetry is obtained by merging the IBCAO (International Bathymetric Chart of the Arctic Ocean) dataset and the ETOPO5 (Earth Topography Five Minute Gridded Elevation Data Set) dataset (see Holland 2000). BESTMAS is forced by daily NCEP/NCAR reanalysis (Kalnay et al. 1996) surface forcing fields. Model forcing also includes river runoff of freshwater in the Bering and Arctic seas. For the Bering Sea, monthly climatological runoffs of the Anadyr, Yukon, and Kuskokwim rivers are used (Zhang et al. 2010). For the Arctic Ocean, monthly climatological runoffs of the Pechora, Ob, Yenisei, Olenek, Yana, Indigirka, Kolyma, Mackenzie, Dvina, Lena, Khatanga, Taimyra, and Piasina rivers are from the Alfred Wegener Institute (Prange and Lohmann 2004). Although BESTMAS has a large model domain that includes the Arctic and the North Pacific, realistic lateral open boundary conditions are still necessary to create the right water masses and fluxes. The POP ocean model has been further modified to incorporate open boundary conditions so that BESTMAS is able to be one-way nested to a lower resolution, global POIM (Zhang 2005). Monthly mean open boundary conditions of ocean temperature, salinity, and sea surface height from the global POIM are imposed at the southern boundaries along 39°N.

2. Estimating the Circulation and Climate of the Ocean, Phase II (ECCO2)

The ECCO2 regional Arctic Ocean solution uses a configuration of the Massachusetts Institute of Technology general circulation model (MITgcm; Marshall et al. 1997; Losch et al. 2010; Nguyen et al. 2010). The domain boundaries are at $\sim 55^\circ$ North in both the Atlantic and Pacific sectors. These boundaries coincide with grid cells in a global, cubed-sphere configuration of the MITgcm (Menemenlis et al. 2005).

The grid covering the Arctic domain is locally orthogonal with horizontal grid spacing of approximately 18 km. There are 50 vertical levels ranging in thickness from 10 m near the surface to approximately 450 m at a maximum model depth of 6150 m. The model employs the rescaled vertical coordinate σ of Adcroft and Campin (2004) and the partial-cell formulation of Adcroft et al. (1997), which permits accurate representation of the bathymetry. Bathymetry is from the S2004 (W. Smith, 2010, personal communication) blend of the Smith and Sandwell (1997) and the General Bathymetric Charts of the Oceans (GEBCO) one arc-minute bathymetric grid. The non-linear equation of state of Jackett and McDougall (1995) is used. Vertical mixing follows Large et al. (1994). A 7th-order monotonicity-preserving advection scheme Daru and Tenaud (2004) is employed and there is no explicit horizontal diffusivity. Horizontal viscosity follows Leith (1996) but is modified to sense the divergent flow (Fox-Kemper and Menemenlis 2008).

The ocean model is coupled to the MITgcm sea ice model described in Losch et al. (2010). Ice mechanics follow a viscous-plastic rheology and the ice momentum equations are solved numerically using the line-successive-over-relaxation solver of Zhang and Hibler (1997). Ice thermodynamics use a zero-heat-capacity formulation and seven thickness categories, equally distributed between zero to twice the mean ice thickness in each grid cell. Ice dynamics use a 2-category thickness with one for open water and one for ice. Salt rejected during ice formation is treated using a sub-grid-scale salt-plume parametrization described in Nguyen et al. (2009). The model includes prognostic variables for snow thickness and for sea ice salinity.

Initial and lateral boundary conditions come from the globally optimized ECCO2 solution (Menemenlis et al. 2008). Surface atmospheric forcing fields are from the Japanese 25-year reanalysis (JRA25; Onogi et al. 2007). Monthly mean river runoff is based on the Arctic Runoff Data Base (ARDB) as prepared by P. Winsor (2007, personal communication).

The ECCO2 Bering Strait solution was optimized based on observations (Nguyen et al. 2010). The model bathymetry in the vicinity of Bering Strait and the location of the Bering Strait cross-section are shown in Figure 29c.

3. Naval Postgraduate School Arctic Modeling Effort (NAME)

The NAME coupled sea-ice–ocean model was described earlier in Chapter II. There are 15 grid cells across Bering Strait in this model (Figure 29d).

4. Nucleus for European Modelling of the Ocean (NEMO) With ORCA Configuration

The ORCA025-N102 model configuration of the National Oceanography Centre Southampton is an “eddy-permitting” z-level global coupled sea ice-ocean model. ORCA025-N102 was developed within the Nucleus for European Modelling of the Ocean (NEMO) framework for ocean climate research and operational oceanography (<http://www.nemo-ocean.eu/>; Madec 2008) as part of the DRAKKAR configurations (DRAKKAR group 2007) and is largely based on the ORCA025-G70 configuration (e.g., Lique et al. 2009). ORCA025-N102 includes the ocean circulation model OPA9 (Madec et al. 1998) coupled to the Louvain-la-Neuve Ice Model sea ice model LIM2 (Fichefet and Morales Maqueda 1997). The ocean model is configured on a tri-polar Arakawa C-grid (Arakawa 1966) with the model poles at the geographical South Pole, in Siberia and in the Canadian Arctic Archipelago. The horizontal resolution is approximately 28 km at the equator, increasing to 6–12 km in zonal and ~3 km in meridional directions in the Arctic Ocean. The model resolves large eddies (~30–50 km), while “permitting” most of smaller eddies. ORCA025-N102 has a higher vertical resolution than the ORCA025-G70 configuration, utilizing 64 vertical levels with thicknesses ranging from approximately 6

m near the surface to 204 m at 6000 m. The high vertical resolution in the upper ocean (8 levels in the upper 50 m and 13 levels in the upper 100 m) greatly improves the model representation of the shallow Arctic continental shelves, Bering and Chukchi Seas. There are 8 model cells across Bering Strait (Figure 29e). The fine model resolution in the both, horizontal and vertical, together with high-resolution model bathymetry adapted from ETOPO2 and partial steps in the model bottom topography accurately approximates the steep seabed relief near the Arctic shelves, resulting in the more realistic along-shelf flow (e.g., Barnier et al. 2006; Penduff et al. 2007). The LIM2 sea ice model uses the Viscous-Plastic (VP) ice rheology (Hibler 1979) and the 3-layer Semtner (1976) thermodynamics updated with sub-grid scale sea ice thickness distribution (Fichefet and Morales Maqueda 1997) and sea ice thickness-dependent albedo (Payne, 1972). To obtain more distinct sea ice edges, the model employs the positive-definite, second moments conserving advection scheme by Prather (1986). The sea ice model is coupled to the ocean model every five oceanic time steps through a non-linear quadratic drag law (Timmermann et al. 2005).

For the 1958–2001 simulations used in the present study, the ORCA025 model was driven by the DRAKKAR Forcing Set (DFS 3.1) atmospheric reanalysis (Brodeau et al. 2010). The reanalysis combines monthly precipitation, daily downward shortwave and longwave radiation from the CORE forcing data set (Large and Yeager 2004) and 6-hourly 10 m wind, 2 m air humidity and 2 m air temperature from ERA40 reanalysis. The turbulent exchanges between atmosphere and ocean and atmosphere and sea ice are computed during model integration using the bulk formulae from Large and Yeager (2004). Climatological monthly continental runoff (Dai and Trenberth 2002) is included as an additional freshwater source, applied along the coastline. Initial conditions for temperature and salinity are derived from a monthly climatology that merges the Levitus (1998) World Ocean Atlas climatology with the PHC2.1 database (Steele et al. 2001) in high latitudes. To avoid salinity drift, the sea surface salinity is restored toward the monthly mean climatological values on the timescale of 180 days for the open ocean and 12 days under sea ice.

5. Pan-Arctic Ice-Ocean Modeling and Assimilation System (PIOMAS)

PIOMAS is a variant of BESTMAS (see description above) with a coarser horizontal resolution (~22 km) and smaller model domain (north of 49°N; Zhang et al. 2008). However, it has 12 categories each for ice thickness, enthalpy, and snow depth (Zhang et al. 2008). The centers of the 12 ice thickness categories are 0, 0.26, 0.71, 1.46, 2.61, 4.23, 6.39, 9.10, 12.39, 16.24, 20.62, and 25.49 m. The model bathymetry in the vicinity of Bering Strait and the location of the Bering Strait cross-section are shown in Figure 29f.

C. BERING STRAIT OBSERVATIONAL MOORING DATA

Year-round moorings have been deployed in the strait almost continuously since 1990 (see Woodgate et al. 2006, 2010; and <http://psc.apl.washington.edu/BeringStrait.html>), at two locations, A2 and A3, as shown in Figure 29a. Site A2 is in the eastern portion of the strait and site A3 is just north of the strait (and in the US EEZ), and is hypothesized to provide a useful average of the flow through both of the channels (Woodgate et al. 2005a, b, 2006, 2007). For some years (92–93, 93–94, 94–95) the A3 mooring was deployed ~ 120 nm further north, but these data are not considered here. Observations from A2 and A3 are available since autumn 1990, except for a few missing months, and for the deployment year autumn 1996–1997 when no moorings were deployed in the strait. In addition, measurements from site A1 in the western channel of the strait, and thus in the Russian EEZ, are available for the early 1990s (from 90–91; 92–93, 93–94) and since 2004. A fourth mooring site, A4, was established near the U.S. coast in 2001 to measure the Alaska Coastal Current (Woodgate and Aagaard 2005). Measurements from these mooring sites were provided to the author for comparison with model results. A high-resolution array was deployed in the strait starting in 2007; for more details see <http://psc.apl.washington.edu/BeringStrait.html>.

Since the region is ice-covered in winter, all mooring instrumentation has traditionally been kept near-bottom to avoid damage by ice keels. The moorings provide measurements of temperature, salinity and velocity at a single depth, approximately 10 m

above bottom. High correlation (0.95; Woodgate et al. 2005b) in velocity was found between all sites in the strait region (Woodgate et al. 2005b). Available Acoustic Doppler Current Profiler (ADCP) data (a few moorings and ship-based ADCP sections from the eastern channel), show strong coherence in the vertical (see e.g., Roach et al. 1995), with some surface intensification of the flows, especially within the ACC. Based on spatial coherence, Woodgate et al. (2005a) used the near-bottom velocity measurements from A3 to estimate the total volume transport through Bering Strait. In terms of water properties, clearly the near-bottom data do not capture the upper layer, which in the summer/autumn period of the year is likely 10–20 m thick, about 1–2 °C warmer and about 1 psu fresher than the lower layer (Woodgate and Aagaard 2005; Woodgate et al. 2010).

The flow through the Bering Strait is generally believed to be driven by some far field forcing (often described as the pressure head forcing) modulated by local wind effects (see Woodgate et al. 2005b for discussion and historic references). Woodgate et al. (2005b) suggest this large-scale forcing likely explains the high correlation in velocities between sites. Near the Alaskan Coast on the edge of the eastern channel, there is a strong, surface-intensified seasonal current. This is the Alaskan Coastal Current, which is present from midsummer until about the end of the year (Paquette and Bourke 1974; Ahlnäs and Garrison 1984; Woodgate and Aagaard 2005), and in summer CTD sections it is present as a ~10 km wide, 40 m deep warm, fresh current (Woodgate and Aagaard 2005). Much less is known about the Siberian Coastal Current, which is present sometimes on the Russian coast (Weingartner et al. 1999) and could influence the flow in the western part of the strait.

D. RESULTS

Model representations of the geographical width across Bering Strait range from 90–160 km (Figures 30, 31). ORCA and PIOMAS have widths most similar to reality (~85 km), while BESTMAS, NAME, and ECCO2 are wider than reality. In the model results (and somewhat in contradiction to observations), the long-term mean velocity structure across Bering Strait shows horizontal shear (Figure 31). The various horizontal

resolutions from the 5 models and the different bathymetry schemes make the results appear disparate upon first glance. In fact, the model cross-sectional area of the strait varies from 2.37–4.50 km², which is an ~8% smaller area in two models (NAME and PIOMAS) and 25–73% larger area in the other models compared to the observational area estimate of 2.6 km² (Table 8). However, a closer look reveals agreement that horizontal shear is present and that the highest speeds tend to be in the eastern channel. Woodgate et al. 2005b showed no significant differences in the September 1990–October 1991 observed mean near-bottom velocities between the two channels; however, at shorter time scales, the monthly mean velocities may differ by up to 35 cm/s. The multi-year mean flow from all models is northward, however the NAME model shows a weak (< 5 cm/s) reversal near the center of the strait. Note that Coachman et al. (1975), sometimes observe a minimum (and even reversal) in this region, although their sections could be subject to time aliasing as discussed below. Vertical shear is present in some model results, particularly the NAME, ECCO2, and ORCA models.

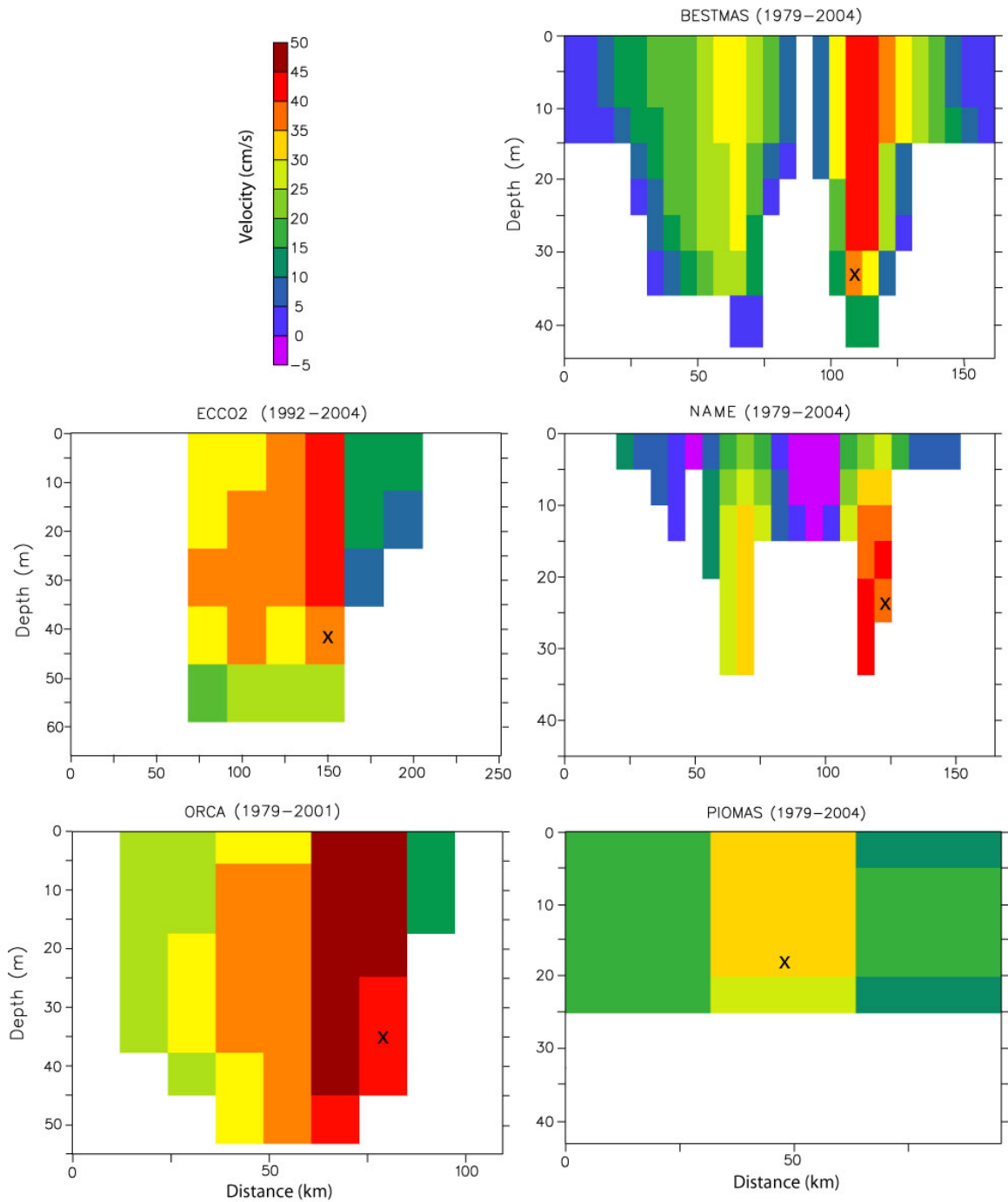


Figure 30. Vertical section of the long-term mean northward velocity (cm/s) across Bering Strait from all models. Positive velocity is northward. A black X marks the approximate location of the A2 mooring within each model domain.

Table 8. Cross-sectional area across Bering Strait for the models and observations and friction coefficients for the models.

Model/ Observed	Area (km ²)	Bottom Friction Coefficient	Lateral Boundary Condition	Lateral Friction Coefficient	Surface Friction Coefficient	
					Ice- Ocean	Air-Ocean
BESTMAS	3.24	quadratic bottom drag: 1.225×10^{-3}	no-slip	variable momentum harmonic horizontal mixing depending on variable grid size	5.5×10^{-3}	1.0×10^{-3}
ECCO2	4.50	quadratic bottom drag: 2.1×10^{-3}	free-slip	modified Leith [Fox-Kemper and Menemenlis, 2008]	5.4×10^{-3}	Large and Pond (1981, 1982)
NAME	2.37	quadratic bottom drag: 1.225×10^{-3}	no-slip	momentum biharmonic horizontal mixing: -1.25×10^{18} cm ⁴ /s	5.5×10^{-3}	0.6×10^{-3}
Observed	2.6	N/A	N/A	N/A	N/A	N/A
ORCA	4.17	quadratic bottom drag: 1.0×10^{-3}	free-slip	bi-harmonic (- $1.5\text{e}+11$ m ⁴ /s)	quadratic, 5.0×10^{-3}	CORE bulk formulae, Large and Yeager (2004)
PIOMAS	2.38	quadratic bottom drag: 1.225×10^{-3}	no-slip	variable momentum harmonic horizontal mixing depending on variable grid size	5.5×10^{-3}	1.0×10^{-3}

To compare with observations, monthly mean northward near-bottom velocity at sites A2 and A3 for models (color) and data (black) for 1979–2004 is shown in Figure 31. For A2 (eastern channel; Figure 29a), model velocities range from ~5 cm/s southward to over 80 cm/s northward. Predominantly, the flow is northward with the mean northward velocity ranging from 28.6 (+/- 1.0) to 40.1 (+/- 1.9) cm/s among models, over the time period when observations are available (Table 9). The range is 29.5 (+/- 0.49) to 43.2 (+/- 0.88) cm/s over the larger 1979–2004 time period (Table 10). Two of the lower resolution models (ORCA and ECCO2) have the highest velocities, while the higher resolution models (BESTMAS and NAME) have lower velocities. The observed mean northward velocity is 26.2 (+/- 2.8) cm/s, which is near the lower range of the modeled mean values. All of the models show a significant (at the 99% level) correlation with the observed velocities at this location. The correlation coefficients range from 0.67–0.78 for the monthly means at A2 (Table 11).

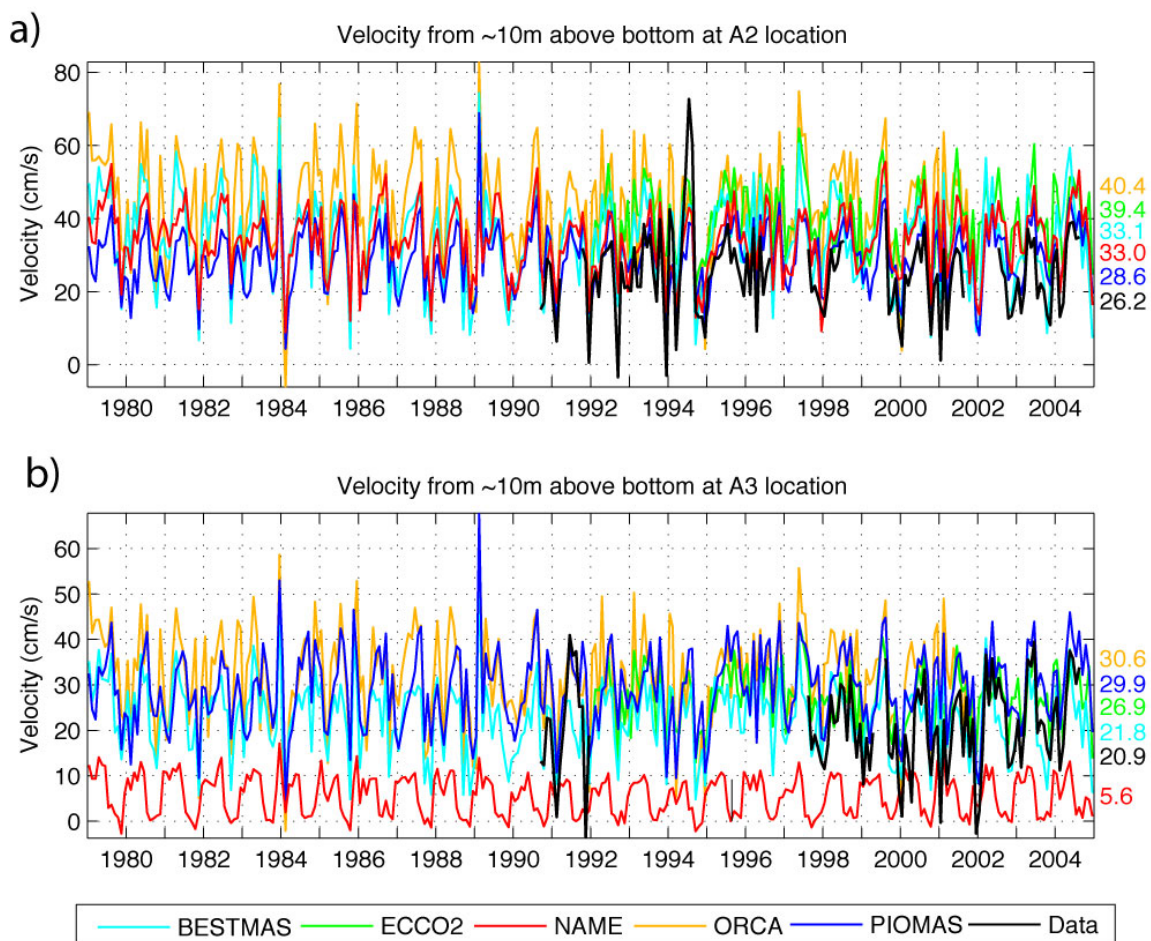


Figure 31. Monthly mean velocity at ~10 above the bottom from the A2 mooring location (upper) and A3 mooring location (lower). Model results are shown in color and the observations are shown in black. Mean values for the time period when data are available are shown on the far right.

Table 9. Mean velocity, volume transport, near-bottom temperature, and near-bottom salinity from the models and from observations, for the time period when observations are available, as shown in Figures 31–34. However, the values from ECCO2 are for 1992–2004 only and the values from ORCA are for 1990–2001 only. Error estimates are shown in parenthesis. All model errors are calculated as the standard error of the mean (sample standard deviation divided by the square root of the sample size).

Model/Data	Mean velocity ~10 m above bottom at the A2 location (cm/s)	Mean velocity ~10 m above bottom at the A3 location (cm/s)	Mean volume transport (Sv)	Mean temper- ature ~10 m above bottom at the A2 location (°C)	Mean temper- ature ~10 m above bottom at the A3 location (°C)	Mean salinity ~10 m above bottom at the A2 location (psu)	Mean salinity ~10 m above bottom at the A3 location (psu)
BESTMAS	33.1 (-1.3)	21.8 (-0.8)	0.69 (0.03)	0.79 (-0.25)	0.65 (-0.24)	33.16 (-0.06)	33.2 (-0.06)
Data	26.2 (-2.8)	20.9 (-2.3)	0.8 (0.20) ⁺	0.27 (-0.30)	-0.11 (-0.20)	32.26 (-0.08)	32.49 (-0.06)
ECCO2	39.4 (-1.2)	26.9 (-0.7)	1.06 (0.03)	1.1 (-0.27)	0.62 (-0.23)	31.72 (-0.06)	32.29 (-0.04)
NAME	33 (-1.0)	5.6 (-0.5)	0.67 (0.03)	-0.96 (-0.09)	-1.26 (-0.05)	32.45 (-0.04)	32.61 (-0.04)
ORCA	40.4 (-1.9)	30.6 (-1.3)	1.29 (0.06)	0.96 (-0.25)	0.79 (-0.24)	32.3 (-0.05)	32.47 (-0.03)
PIOMAS	28.6 (-1.0)	29.9 (-0.9)	0.81 (0.03)	0.34 (-0.21)	0.6 (-0.23)	33.09 (-0.05)	32.8 (-0.05)

+the uncertainty for the data estimate is ~25% (Woodgate et al. 2005a, b)

Table 10. Long-term mean velocity, volume transport, near-bottom temperature, and near-bottom salinity from the models, for the time periods shown in Figures 31–34. Error estimates are shown in parenthesis.

Model/Data	Mean velocity ~10 m above bottom at the A2 location (cm/s)	Mean velocity ~10 m above bottom at the A3 location (cm/s)	Mean volume transport (Sv)	Mean temper- ature ~10 m above bottom at the A2 location (°C)	Mean temper- ature ~10 m above bottom at the A3 location (°C)	Mean salinity ~10 m above bottom at the A2 location (psu)	Mean salinity ~10 m above bottom at the A3 location (psu)
BESTMAS	34 (-0.69)	22.8 (-0.45)	0.72 (0.02)	0.76 (0.17)	0.71 (-0.16)	33.18 (-0.05)	33.17 (-0.04)
ECCO2	39.9 (-0.78)	27.4 (-0.52)	1.07 (0.02)	1.08 (-0.25)	0.63 (-0.20)	31.72 (-0.05)	32.25 (-0.03)
NAME	34.1 (-0.52)	5.6 (-0.24)	0.65 (0.01)	-1.02 (-0.06)	-1.27 (-0.03)	32.46 (-0.02)	32.58 (-0.02)
ORCA	43.2 (-0.88)	31.6 (-0.65)	1.33 (0.03)	0.89 (-0.17)	0.69 (-0.15)	32.33 (-0.02)	32.47 (-0.02)
PIOMAS	29.5 (-0.49)	29.2 (-0.49)	0.79 (0.02)	0.26 (-0.14)	0.53 (-0.15)	33.13 (-0.03)	32.78 (-0.03)

Table 11. Correlation coefficients between models and the observations of northward velocity, temperature, and salinity at A2 and A3 locations. All correlations are significant at the 95% level.

Model	Velocity		Temperature		Salinity	
	A2	A3	A2	A3	A2	A3
BESTMAS	0.78	0.71	0.78	0.7	0.67	0.53
ECCO2	0.67	0.72	0.77	0.76	0.6	0.48
NAME	0.69	0.27	0.73	0.86	0.7	0.57
ORCA	0.68	0.7	0.79	0.76	0.6	0.39
PIOMAS	0.70	0.82	0.88	0.79	0.66	0.59

Figure 31b shows the near-bottom northward velocity at the A3 location. The model spread of velocities is larger for A3, with the NAME model having the lowest mean velocity (5.6 ± 0.5 cm/s) and ORCA having the highest mean velocity (30.6 ± 1.3 cm/s) over the same time period as observations. The observed mean northward velocity is 20.9 ± 2.3 cm/s. The NAME model has a problem representing the correct magnitude of the velocity at this location, which appears to be related to the upstream bathymetry representation. The correlation between the models and the data is more variable at A3, with correlation coefficients ranging between 0.27 and 0.82 (Table 11).

Near-bottom monthly mean temperatures at the A2 and A3 mooring locations are shown in Figure 32. (Temperature at A1 is not shown because there are too few data available at this time.) Temperatures tend to be warmer at the southern A2 location, with model means ranging between $-0.96 (\pm 0.09)$ to $1.1 (\pm 0.27)$ °C. The mean observed near-bottom temperature for the same location is $0.27 (\pm 0.3)$ °C. ORCA, ECCO2, and BESTMAS models tend to overestimate the temperature by $0.5\text{--}0.8$ °C in the mean, while NAME underestimates the temperature by 1.2 °C in the mean. It is possible that the colder temperatures for the NAME model may be related to excessive ice production, which causes the sinking of very cold surface water, especially in polynya regions of the northern Bering Sea. Surprisingly, the PIOMAS temperatures are closest to the observed, despite the fact that it is the lowest resolution model in this study and only has 3 grid points across the strait (Figure 30). Temperatures at the A3 location are, again, underestimated in the NAME model and overestimated in ORCA, ECCO2, BESTMAS and also in PIOMAS. While the magnitude of the model-data differences may be up to ~ 1 °C in the mean, the models' results are significantly correlated (at the 99% confidence level) with the observations. The correlation coefficients range between 0.73–0.88 at A2 and between 0.70–0.86 at A3 (Table 11). There is no trend, either observed or modeled, in the time series shown here. There is, however, a strong annual cycle present (as discussed by Woodgate et al. 2005a), which dominates the correlations. This annual cycle will be discussed below.

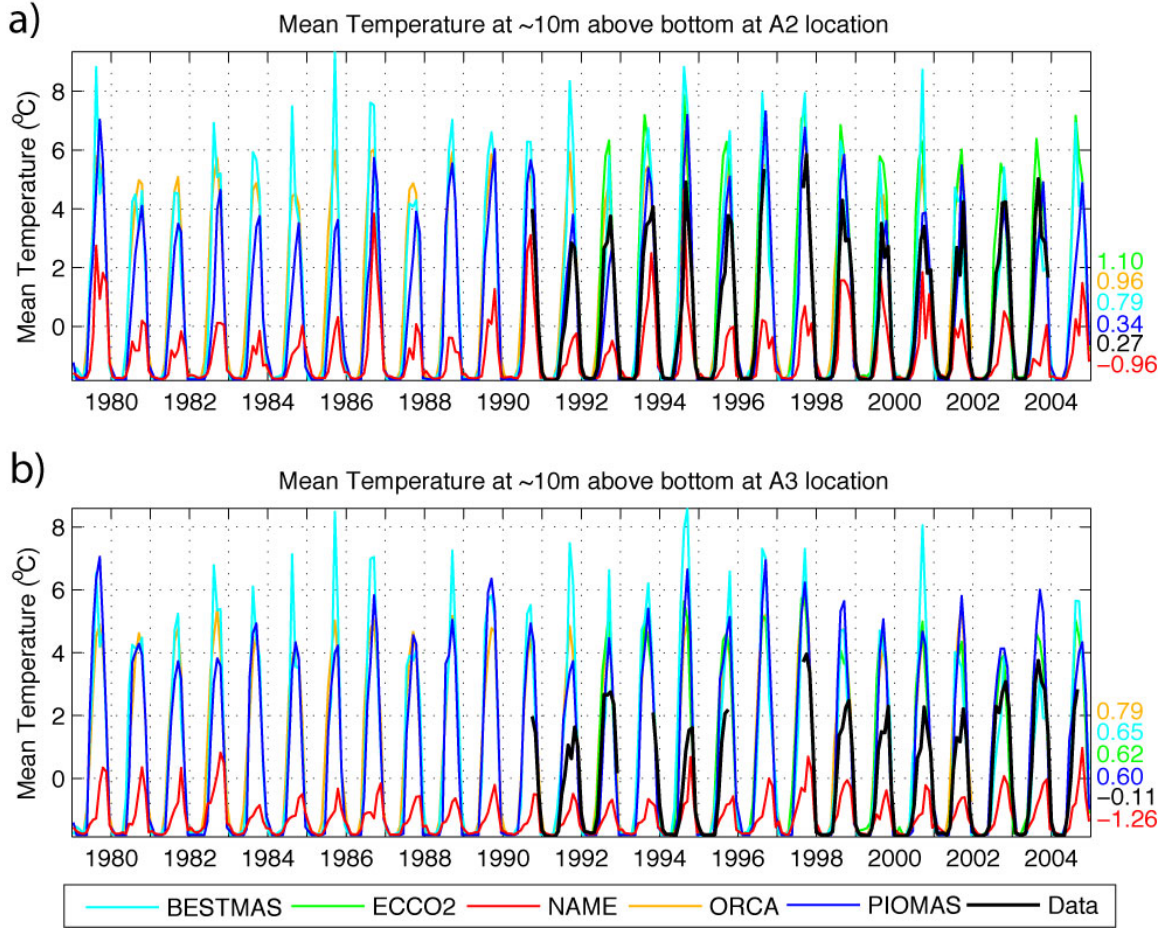


Figure 32. Monthly mean near-bottom temperature ($^{\circ}\text{C}$) at the (a) A2 and (b) A3 mooring locations. Model results are shown in various colors and observations are shown in black. Mean values for the time period when data are available are shown on the far right.

A similar analysis was performed for salinity at the A2 and A3 mooring locations (Figure 33). The mean modeled salinity ranges between 31.7 (± 0.06) and 33.2 (± 0.06) psu at A2 and between 32.2 (± 0.04) and 33.2 (± 0.06) psu at A3. The mean observed salinities are 32.3 (± 0.08) at A2 and 32.5 (± 0.06) at A3. The BESTMAS and PIOMAS models tend to overestimate the salinity, by up to 0.9 psu above the observed mean value, whereas the NAME, ECCO2, and ORCA models have values close to the observed. All of the models' results are significantly correlated (at the 99% confidence level) with the observations of salinity at A2 and A3. The correlation coefficients range between 0.60 and 0.70 at A2 and between 0.39 and 0.59 at A3 (Table

11). The correlations are not as high for salinity as they are for temperature, especially at the A3 location. Again, an annual cycle of salinity is apparent in the time series (also see Woodgate et al. 2005a); however, it is not as strong as the annual cycle of temperature. The actual annual cycles will be discussed below.

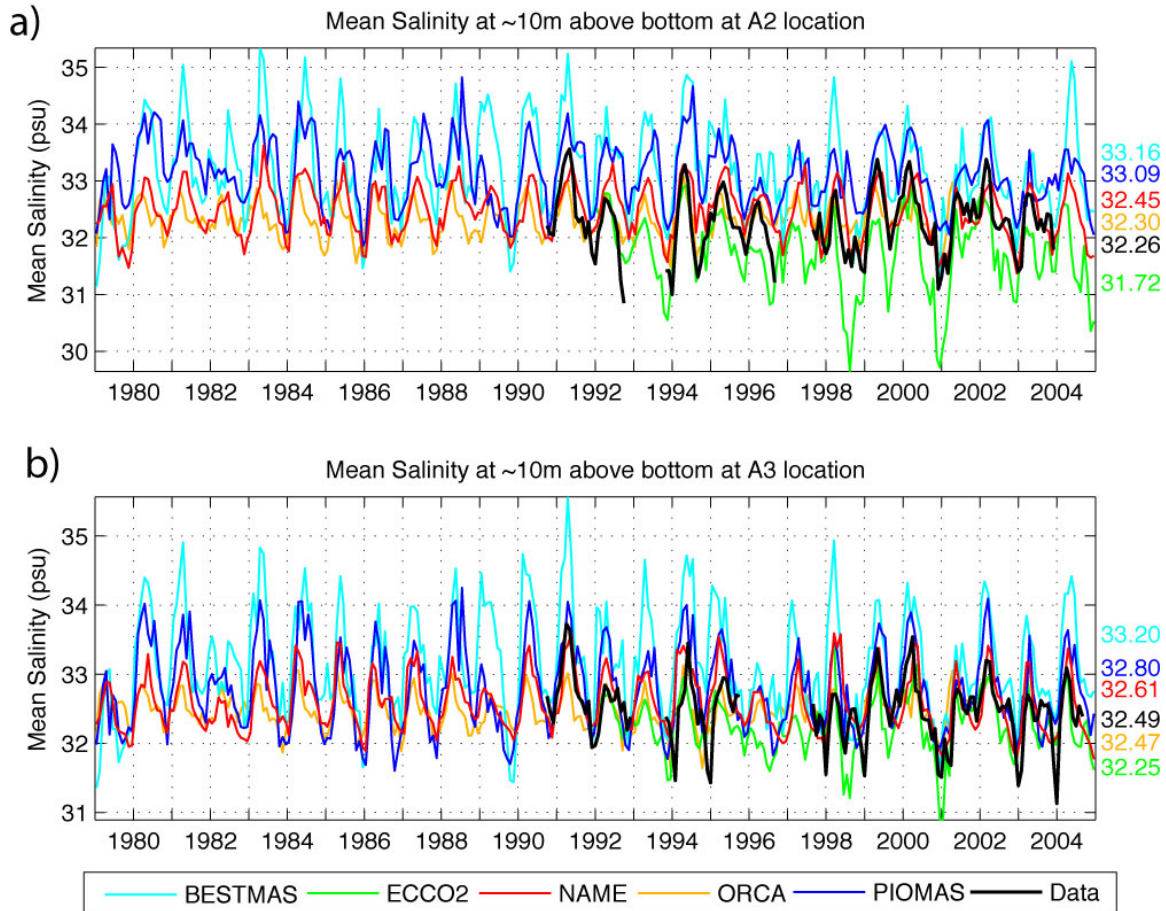


Figure 33. Monthly mean near-bottom salinity at the (a) A2 and (b) A3 mooring locations. Model results are shown in various colors and observations are shown in black. Mean values for the time period when data are available are shown on the far right.

It is important to recognize that a comparison between point measurements and model results is difficult. In the data, velocity, as well as temperature and salinity, is measured at a single point, while in models it is a grid-cell mean, which may range from a few to tens of kilometers in the horizontal and several meters in the vertical. In addition, the discrepancy between the real and model bathymetry introduces a difference in

bathymetric gradients, displacing model currents from their “true” geographical positions. Table 12 and Figure 30 illustrate these points. Table 12 shows the depth at the moorings A2 and A3 and model depth at the co-located virtual moorings; the difference between real and model bathymetry is clear. Moreover, in the models (although seemingly less so in the observations) velocity can vary significantly between the adjacent model grid cells (Figure 30), thus the results of model-data comparisons would strongly depend upon the exact geographical position of model virtual moorings. Finally, the stochastic nature of the oceanic turbulence is not simulated by the models used in this study. Therefore, it is likely more informative to evaluate model results using integrated fluxes, as discussed below.

Table 12. Depth information (m) for the models and the observations at the A2 and A3 mooring locations.

Location	Model/data	Water column depth (m)	Mid-depth of model grid cell or depth of observation ~10 m above bottom (m)
A2	Data	53.0	44.0
	BESTMAS	51.0	39.5
	ECCO2	50.0	35.0
	NAME	53.0	37.7
	ORCA	57.9	35.5
	PIOMAS	43.0	33.0
A3	Data	56.0	47.0
	BESTMAS	51.0	39.5
	ECCO2	50.0	35.0
	NAME	53.0	37.7
	ORCA	57.9	35.5
	PIOMAS	43.0	33.0

Monthly mean Bering Strait volume transport from the models and observations is shown in Figure 32. Model means range from 0.67 (+/- 0.03) to 1.29 (+/- 0.06) Sv (Table 9) over the time period when observations are available. The volume transport is highest for the ORCA and ECCO2 models and is lowest for the PIOMAS, BESTMAS and NAME models. The observed estimate of the long-term mean (1991–2004) volume transport through Bering Strait is 0.8 +/- 0.2 Sv (Woodgate et al. 2005a). This estimate is based on single-depth velocities at the A3 mooring location multiplied by the total cross-sectional area of 4.25 km², although numbers do not differ significantly if using observations from the A2 site.

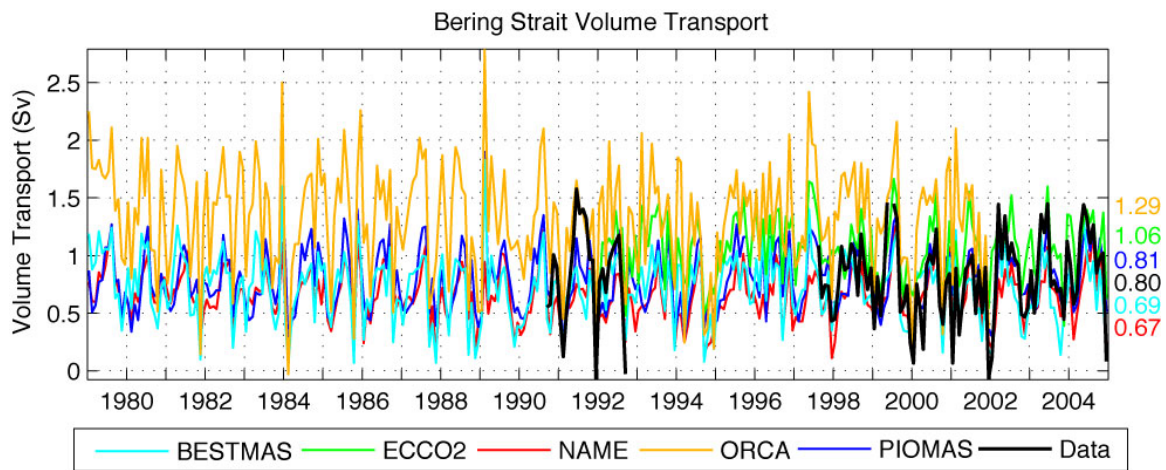


Figure 34. Monthly mean volume transport from the models and observations. The observations are based on the near-bottom velocity at the A3 mooring location multiplied by a cross-sectional area of 4.25 km², as per Woodgate et al. (2010). Mean values for the time period when data are available are shown on the far right.

Annual mean volume transport from models and observations is shown in Figure 35a. Observed volume transport ranges from 0.6–1 Sv (+/- 0.2 Sv; Woodgate et al. 2006), which is most similar to the estimates from the BESTMAS, NAME, and PIOMAS models. The ACC, which is not observed by the A2 or A3 near-bottom measurements, may add around 0.1 Sv to the summer estimates (Woodgate and Aagaard 2005); however, the main uncertainty with these estimates is the assumption of spatially uniform flow across the strait.

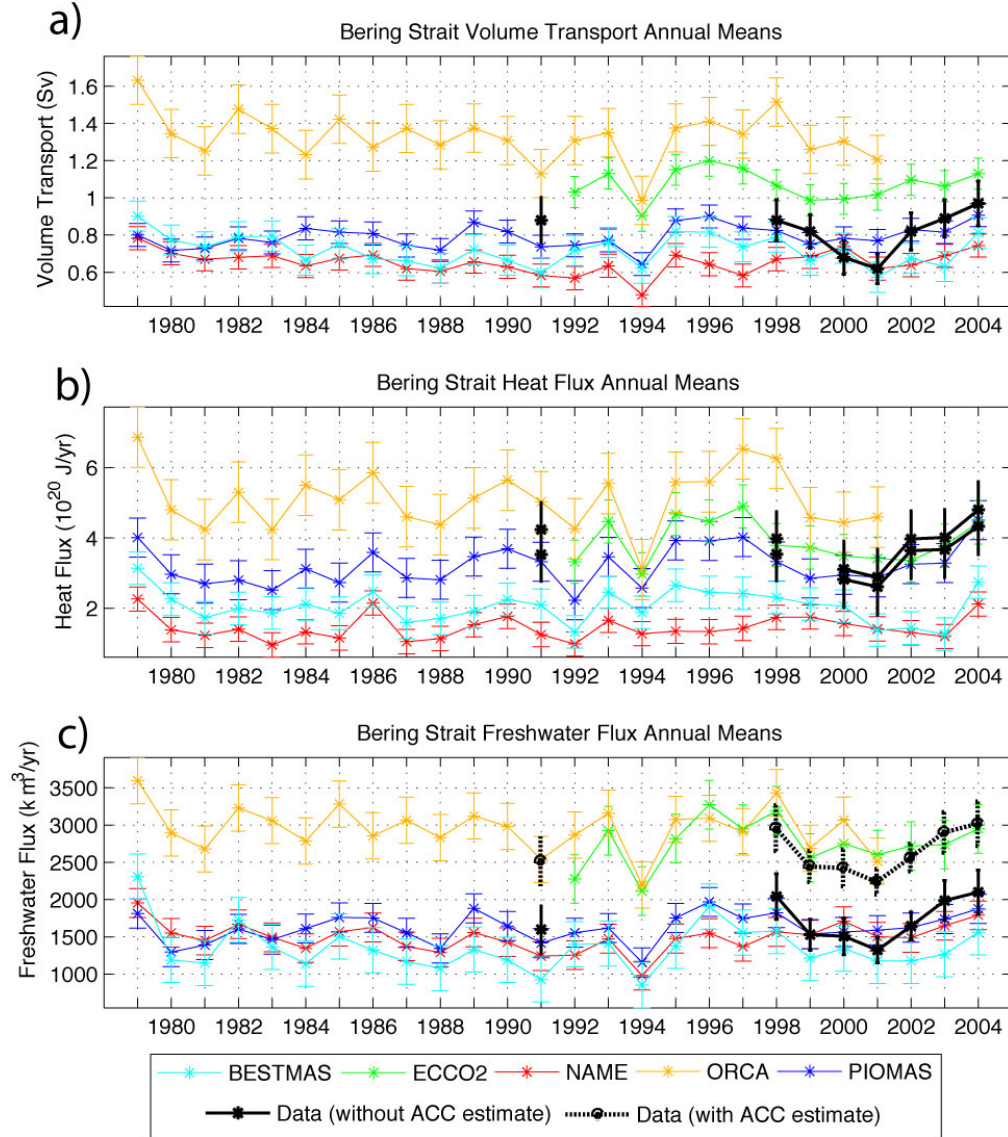


Figure 35. Annual mean (a) volume transport, (b) heat, and (c) freshwater fluxes. Heat is referenced to -1.9°C for NAME, ECCO2, and ORCA, in order to compare with cited observations in the text. Heat is referenced to -1.8°C for PIOMAS and BESTMAS, due to model limitations. Freshwater is referenced to 34.8 psu. Observed volume transport and freshwater flux values do not include the ACC and stratification, which likely add ~ 0.1 Sv and $800\text{--}1,000\text{ km}^3/\text{yr}$ (see Woodgate et al. 2006). The dashed black line (c) represents the freshwater flux with the estimated ACC and stratification correction of an additional $900\text{ km}^3/\text{yr}$. The observed heat flux values include an estimate for the ACC using SST for a 10-m surface layer (lower bound; lower black line) and a 20-m surface layer (upper bound; upper black line). Observed heat flux values are described further in Woodgate et al. (2010).

Freshwater flux from the Bering Sea into the Chukchi Sea is an important factor affecting stratification and the maintenance of the Arctic Ocean halocline (e.g., Aagaard et al. 1985a). Heat fluxes through Bering Strait and through the Chukchi shelf appear to influence the distribution and thickness of sea ice (Shimada et al. 2006; Woodgate et al. 2010). Previously published observations of heat flux (e.g., Woodgate et al. 2010) use a reference temperature of -1.9°C , which will overestimate heat fluxes when freezing temperature is above that value. However, for comparison, the same value was used for a reference temperature in the model calculations. The PIOMAS and BESTMAS models use constant reference temperature of -1.8°C to calculate heat flux because these two models use this temperature as the freezing temperature for an ease in conserving heat in the model. It is estimated that this difference in reference temperature between -1.9°C and -1.8°C produces errors that are $< 5\%$ of the mean. Oceanic heat flux through Bering Strait in the models was calculated as the vertical and horizontal integral of: the heat (heat capacity multiplied by the difference between the temperature and the reference temperature) multiplied by grid cell velocity normal to the cross-section on a monthly mean time scale.

The annual mean oceanic heat flux time series for the models and observations (as per Woodgate et al. 2010) are shown in Figure 37b. In the models, peaks in the heat flux occurred during several years (e.g., 1979, 1986, 1993, and 1997) and consistently showed up in results from all five models. However, data coverage is not sufficient to confirm these peaks. A peak in 2004 is noted in observations (see Woodgate et al. 2010) and is apparent in all of the models, except ORCA, which does not have results for that time period. ECCO2 is also able to simulate a recent increase in heat flux in 2007 (not shown), similar to the observations (Woodgate et al. 2010).

The long-term model mean heat flux ranged between $1.5\text{--}5.1 \times 10^{20}$ J/yr. ORCA and ECCO2 have much higher values than BESTMAS and NAME. Observations of the annual heat flux based on near-bottom measurements, a correction for the ACC, and SST from satellite data were published in Woodgate et al. (2010). The observationally

estimated range of heat flux is $\sim 2.8\text{--}4.5 \times 10^{20}$ J/yr with estimated uncertainty of 0.8×10^{20} J/yr, based on years 1991, 1998, 2000–2006. However, the 2007 heat flux was estimated at over 5×10^{20} J/yr.

For the calculation of freshwater fluxes, a reference salinity of 34.8 psu was used because this value is considered to be the mean salinity of the Arctic Ocean and has been used in most other Arctic studies (based on original work by Aagaard and Carmack 1989). Integrated annual mean oceanic freshwater fluxes were calculated on a monthly mean timescale (see Equation 1 in Melling 2000) from each of the models and are shown in Figure 37c. An observationally-based lower bound of annual mean freshwater fluxes is also shown, however these values do not include the ACC or stratification and according to Woodgate et al. (2005c, 2006) they underestimate the freshwater flux by about $800\text{--}1,000 \text{ km}^3/\text{yr}$. With this correction, the observed freshwater annual means are similar to results from the ECCO2 and ORCA models, with the other models appearing to underestimate the total freshwater flux. No long-term trend is apparent in either the heat or freshwater flux for this time period, however a gradual increase in freshwater during the early 2000s has occurred in the model results, ending with a peak in freshwater flux in 2004, similar to observations (also see Woodgate et al. 2006, 2010).

It is important to note that both the models and the data have limitations with respect to calculations of heat and freshwater fluxes. The models used here are too coarse to represent the narrow Alaska Coastal Current (ACC), which is estimated to carry 10–20% of the freshwater flux (Woodgate and Aagaard 2005) and 20–30% of the heat flux (Woodgate et al. 2010) through the strait. The historic near-bottom data used here does not measure the upper ocean seasonally varying stratification or ACC, which is a surface/coastal feature. Thus, on-going observational research is using extra moorings, hydrographic data and upper water column sensors to estimate stratification (see e.g., <http://psc.apl.washington.edu/BeringStrait.html>). Also, new models are configured at increasingly high spatial resolution, an example of which is presented at the end of this chapter.

Arctic shelf seas have a strong annual cycle of temperature and salinity, especially in the upper ocean; some areas may also exhibit strong annual changes in the oceanic circulation. The Bering Strait region is no different in this respect. Observations have shown stronger northward flows in summer (e.g., Woodgate et al. 2005a, b and references therein). According to the model results, volume transport peaks in summer (May–July) and is lowest in winter (December–March; Figure 36) and this agrees reasonably with observational results (peaking in May/Jun, minimum in December–February; Woodgate et al. 2005a). However, error bars make these maxima less certain in both the data and model results. The point data measuring near-bottom flow have a larger annual cycle, with a range of 0.4 to 1.3 Sv (errors order 25%; Woodgate et al. 2005a, b). PIOMAS, BESTMAS, ECCO2, and NAME models combining all points across the strait have similar annual cycles to the data; however, they are not as strong.

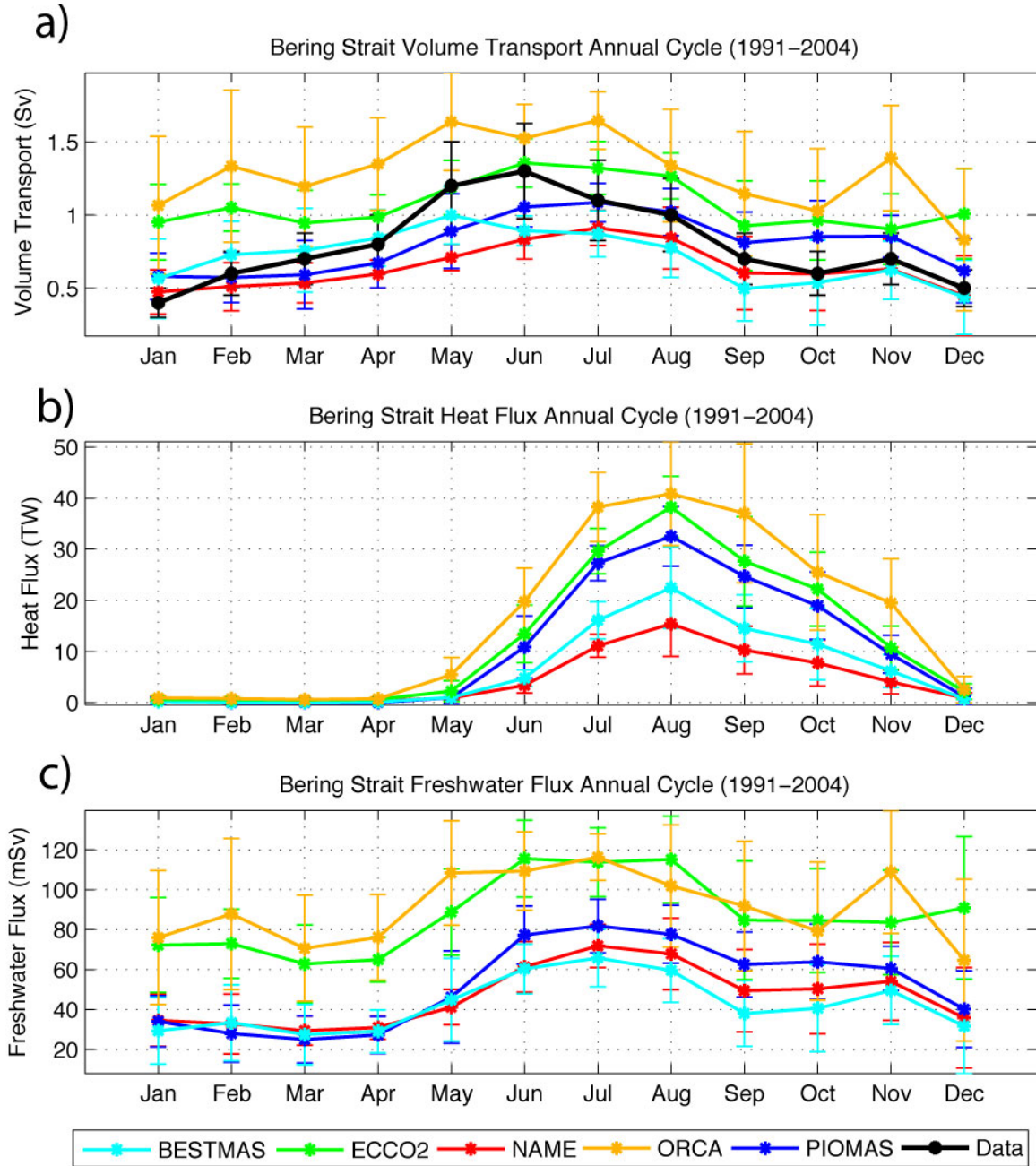


Figure 36. Annual cycles of (a) volume transport, (b) heat flux, and (c) freshwater transport. The annual cycles are averaged over 1991–2004, except for ORCA (1991–2001) and ECCO2 (1992–2004). The heat flux is referenced to -1.9°C for NAME, ECCO2, and ORCA. The reference temperature is -1.8°C for PIOMAS and BESTMAS due to model limitations. The freshwater transport is referenced to 34.8 psu.

As shown by Woodgate et al. (2010), the heat flux annual cycle is also very strong. Observational results from near-bottom moorings combined with SST from satellite data (Woodgate et al. 2010, Figure 3) suggest strong interannual variability in the timing of the summer peak, although the computation presented there does not include the seasonality of the ACC. In the models (Figure 36b), heat flux peaks in summer and is near-zero in winter. However, the models do not agree on the magnitude of the summertime peak, which ranges between 15 (+/- 6.4) to over 40 (+/- 14) TW. The heat flux is near zero for December–April (when water temperatures are around freezing). The models with the highest resolutions (BESTMAS and NAME) show lower peaks in the summertime heat flux [15 (+/- 6.4) and 22.5 (+/- 7.9) TW], while the lower resolution models have higher heat fluxes, which is in part related to their simulation of summer volume flux.

Freshwater flux is important to the Chukchi Sea and the Arctic Ocean due to the importance of maintaining the halocline there. This halocline separates the upper mixed layer from the deeper, warmer Atlantic layer. Annual cycles of freshwater flux through Bering Strait are similar for PIOMAS, BESTMAS, and NAME, with peaks in the summer (June–August) and lowest in winter (December–April; Figure 36c). Again, error bars make these peaks in the model results less certain. The freshwater flux maxima for these models is between 65 (+/- 14.3) - 80 (+/- 13.4) mSv in July. Annual cycles for ECCO2 and ORCA have somewhat similar shapes, however they transport more freshwater (up to 115 (+/- 11.7) mSv in summer and more than 60 (+/- 40) mSv in winter for ORCA) to the north.

Using the monthly mean volume transport values shown in Figure 36 and the annual cycles of volume transport shown in Figure 36a, I calculated the volume transport anomalies, which are shown in Figure 37. The anomalies confirm that there is no trend in the transport time series from 1979–2004. The ORCA model tends to produce larger anomalies than any of the other models or data. However, all of the models are significantly correlated (at the 95% level) with the data. The correlation coefficients range from 0.59 to 0.73.

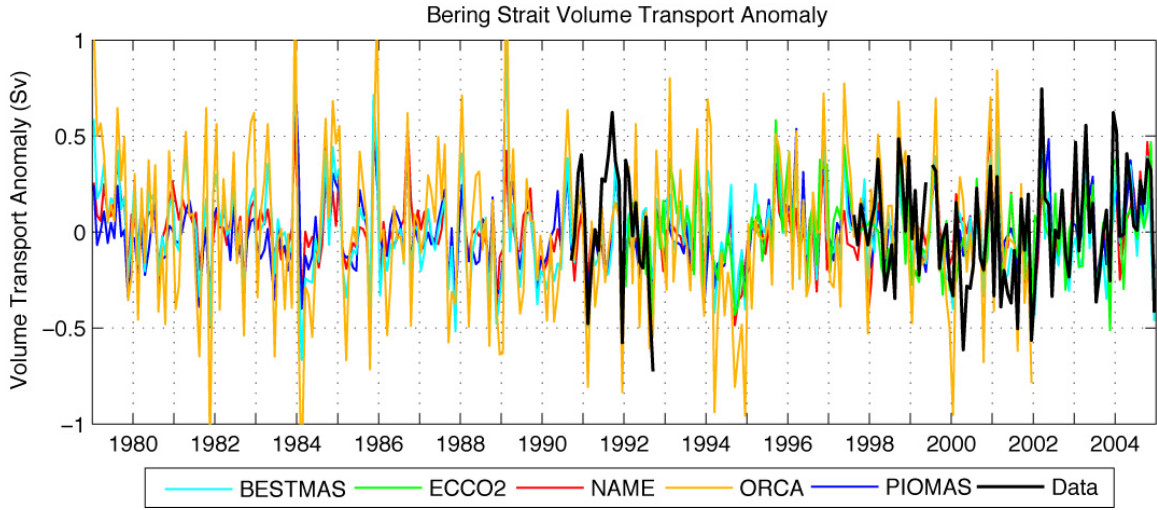


Figure 37. Monthly mean volume transport anomalies from the annual cycle (Sv). The annual cycle for each model and the data are shown in Figure 36a.

E. SUMMARY AND CONCLUSIONS

Model volume transports ranged from 0.67 (+/- 0.03) to 1.29 (+/- 0.06) Sv in the mean, compared to observational estimates of 0.8 +/-0.2 Sv. Thus, most of the models are in agreement with the observational estimate to within errors. ORCA and ECCO2 showed the highest volume transports, while NAME and BESTMAS showed the lowest transports. Note that of the models, ORCA and ECCO2 also have the largest cross sectional area of the strait. Higher resolution models seem to give lower transport estimates; the cause of this is not fully understood. The models are using both lateral and vertical friction parameterization to represent the flow next to the boundary (bottom/surface or lateral; see Table 8). Some uncertainty of model estimates of the volume transport throughout the strait might be related to the estimation of the frictional layers, subject to the parameterization used. Using a $1/4^\circ$ global model, Penduff et al. (2007) have demonstrated that enstrophy-conserving momentum advection schemes produce a spurious numerical sidewall friction, leading to a weaker topographic alignment of the mean flow and weaker barotropic transports. Both spurious sidewall and explicit no-slip lateral friction could contribute to lower transports in BESTMAS and

NAME models compared to ECCO2 and ORCA, as the last two models feature free-slip lateral boundary conditions. Besides, ORCA utilizes energy-ensrophy conserving advection, resulting in higher transport than in ECCO2 (Tables 9 and 10). However, this cannot explain a higher transport in the PIOMAS model compared to BESTMAS, since these two models share the same configuration, except for the resolution and different number of sea ice categories (12 and 8 respectively).

Panteleev et al. (2010) applied an inverse model (with 10 grid points across the strait) to reconstruct the flow using available data for 1990–1991 and recently calculated the transport through Bering Strait as 0.57 Sv (no stated uncertainty). The data used to reconstruct the circulation were from 12 moorings that were deployed in the Bering Strait and Chukchi Sea from September 1990 to October 1991 (Woodgate et al. 2005b). This estimate from Panteleev et al. (2010) tends to agree with the estimates from the BESTMAS and NAME models. In fact, the mean volume transports during the same time period (September 1990–October 1991) were 0.62 (+/- 0.03) and 0.59 (+/- 0.03) Sv for the BESTMAS and NAME models, respectively.

The model sections presented here show significant vertical and horizontal velocity shear across the strait. This appears to be somewhat in contrast to the limited observations, which show strong coherence of flow and agreement of near-bottom speeds in the 2 channels of the strait. However, a strong coherence between 2 point measurements in the strait does not indicate that the flow is homogenous throughout the strait. Observations indicate a stronger flow in the ACC (not shown), which would suggest some horizontal velocity shear across the strait. The only currently published sections of observed velocity in the strait are those of Coachman et al. (1975), which indicate both horizontal and vertical shear in the speeds across the strait. However, these sections may be subject to time aliasing being taken over a period of days.

It seems possible that some of the horizontal and vertical shear found in the models is due to edge effects and/or the poor resolution of the real world bathymetry. It must also be remembered however, that the observational transports presented here are based on near-bottom measurements of velocity at A2 or A3 and an assumption of

homogeneity of flow at all locations in the strait, which may not be an accurate assumption. This is currently being tested by an increased mooring effort in the strait region. Future observational results from this expanded mooring array should help to narrow the uncertainty in the measurements and produce more reliable integrated fluxes.

Increases in model resolution and improvements in model bathymetry are expected to improve the representation of the flow structure in Bering Strait. Initial spin-up results from a higher resolution version (~2.3 km in the horizontal) of the NAME model are compared with the current 9-km results in Figure 37. The improvements in the strait bathymetry are obvious, with actual Diomed Islands being present in the strait and a more realistic depth of ~50 m is reached in the two channels of the strait. However, representation of the northward velocity and its horizontal shear is not qualitatively different between the two models. The new 2.3-km model has 4 times as many (i.e., 60) grid cells across the strait, which allows for the representation of the narrow Alaska Coastal Current and its velocity core in the eastern part of the strait appears to be separated from the coast by a narrow boundary layer, which may be more similar to recent observations (Rebecca Woodgate, 2010, personal communication). When new model output becomes available, a future manuscript is planned to analyze those results in comparison with data from the extended array of moorings across the Bering Strait.

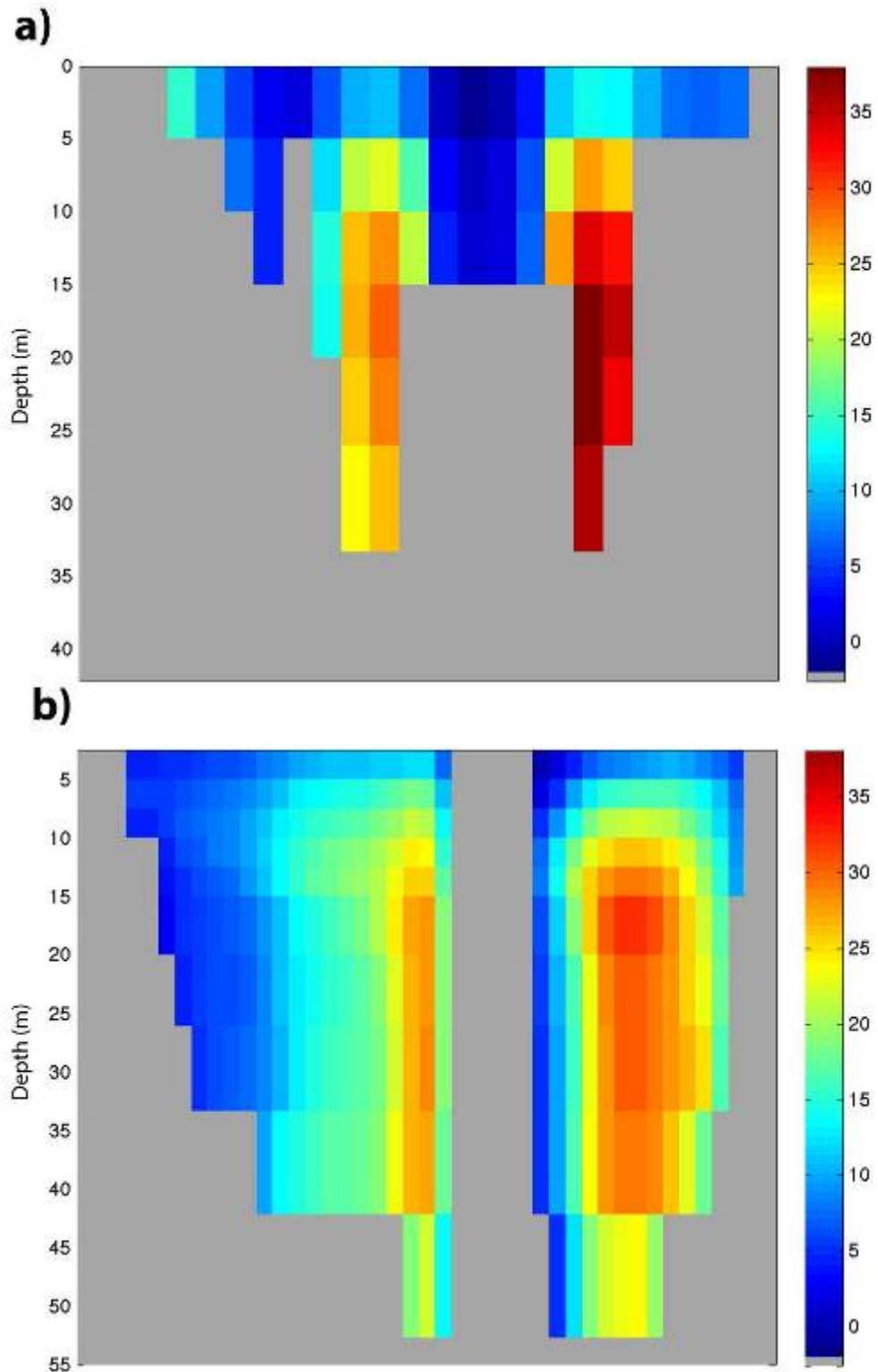


Figure 38. Bering Strait velocity (cm/s) from the (a) 9-km model during the 26-year mean March and (b) 2-km model during spin-up mean March.

VIII. LINKAGES TO WEATHER INDICES, BIOLOGICAL PRODUCTIVITY, AND THE WESTERN ARCTIC

A. LINKAGES TO LARGE-SCALE WEATHER INDICES

Three large-scale weather indices of the Arctic and/or North Pacific have been linked to several low-frequency oscillations within the northern North Pacific and the Bering Sea (e.g., Niebauer 1988; Niebauer and Day 1989; Niebauer et al. 1999). These indices are the Arctic Oscillation (AO), the Pacific Decadal Oscillation (PDO) and the Pacific/North American Pattern (PNA).

The AO is an atmospheric circulation pattern in which the atmospheric pressure over the polar regions varies in opposition with that over middle latitudes (about 45° North) on time scales ranging from weeks to decades (see e.g., http://nsidc.org/arcticmet/patterns/arctic_oscillation.html). High pressure over the polar region and low pressure at mid-latitudes characterizes the “negative phase”, while the “positive phase” exhibits the opposite pattern. A positive AO tends to drive ocean storms farther north due to the higher pressure at mid-latitudes.

The PDO Index is defined as the first principal component of extratropical North Pacific Ocean SST anomalies (Mantua et al. 1997; Zhang et al. 1997; Hare and Mantua 2000). The PDO index is available at <http://jisao.washington.edu/pdo/>. The PDO term was first introduced by Steven Hare in the late 1990s, who used it to help explain connections between Alaska salmon production cycles and Pacific climate (Hare et al. 1999). Major changes in northeast Pacific marine ecosystems have been correlated with phase changes in the PDO (e.g., Beamish 1993; Hare and Mantua 2000). Warm (positive) time periods have seen enhanced coastal ocean biological productivity in Alaska and inhibited productivity off the west coast of the contiguous United States, while cold (negative) PDO time periods have been associated with an opposite north-south pattern of marine ecosystem productivity.

The Pacific/North American teleconnection pattern (PNA) is an important mode of low-frequency variability in the Northern Hemisphere extratropics

(<http://www.cpc.noaa.gov/data/teledoc/pna.shtml>; Barnston and Livezey 1987). The positive phase of the PNA pattern exhibits above-average atmospheric geopotential height fields in the vicinity of Hawaii and over the Rocky Mountain region of North America, and below-average heights located south of the Aleutian Islands and over the southeastern United States (Wallace and Gutzler 1981). The negative phase is associated with a westward retraction of the jet stream toward eastern Asia, blocking activity over the high latitudes of the North Pacific, and a strong split-flow configuration over the central North Pacific. Anomalously warm temperatures over western Canada and the western United States are associated with a positive phase of the PNA, as well as high levels of precipitation from the Gulf of Alaska into the Pacific Northwestern United States. Yin (1994) demonstrated that the PNA is also strongly influenced by the El Niño/Southern Oscillation (ENSO) phenomenon. The positive phase of the PNA pattern tends to be associated with Pacific warm episodes (El Niño), and the negative phase tends to be associated with Pacific cold episodes (La Niña).

The monthly mean and 13-month running mean values of the AO, PDO, and PNA are shown in Figure 39 for 1979–2004. A 13-month running mean was chosen in order to smooth out the annual cycle.

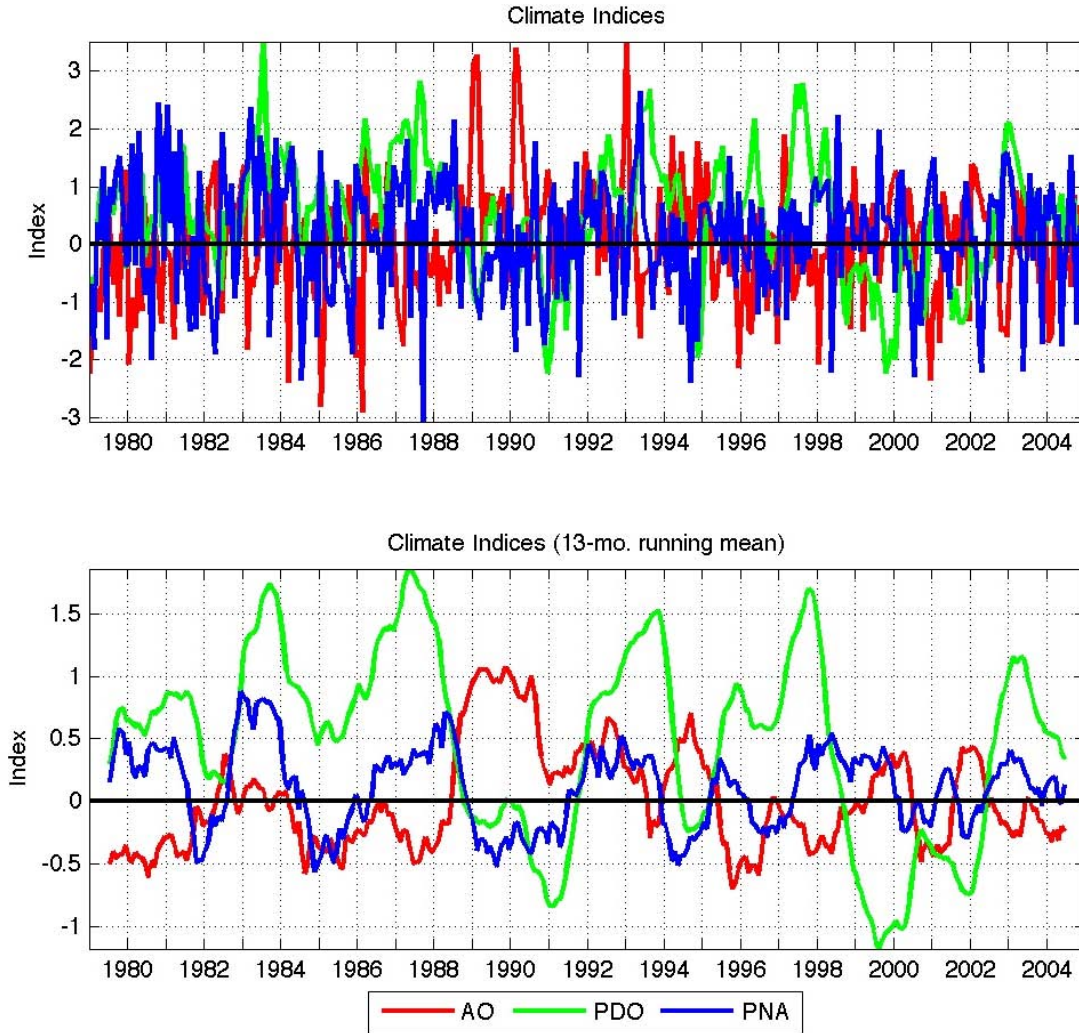


Figure 39. Monthly mean (upper) and (lower) 13-month running mean values of the AO, PDO, and PNA.

The low-frequency temperature changes in the Bering Slope Current (discussed in Chapter V) may be indirectly related to large-scale weather indices of the Arctic and/or North Pacific. Correlations between the monthly mean temperatures at sections BSC1, BSC2, BSC3, and BSC4 and the AO, PDO, and PNA were calculated for a lag range of ± 50 months. A lag range of ± 50 months was used because the low-frequency oscillations in Figure 39 are of a similar time period. Although the monthly mean temperatures are not significantly correlated at any of these BSC sections, the 13-month running means showed some significant correlations (Table 13).

Table 13. Correlation coefficients between the mean temperature across BSC sections and large-scale weather indices. Correlations are for the 13-month running mean values of both the temperature time series and the weather indices for 1979–2004. Correlations with no lag are shown (Corr. no lag) with the associated p-value. The maximum correlation (Max. Corr.) is also shown for a lag range of +/- 50 months, along with the lag time and p-value. A negative lag means that the mean temperature across the BSC section is leading the weather index. The significance level used is 95%.

Section	Index	Corr. no lag	P-value	Max. Corr.	Lag	P-value
BSC1	AO	-0.33	0.0000	-0.57	-8	0.0000
BSC1	PDO	0.02	0.6764	0.33	50	0.0000
BSC1	PNA	0.15	0.0080	0.32	-9	0.0000
BSC2	AO	-0.27	0.0000	-0.59	-36	0.0000
BSC2	PDO	0.09	0.1348	0.38	50	0.0000
BSC2	PNA	0.10	0.0936	0.42	-14	0.0000
BSC3	AO	-0.29	0.0000	-0.52	-17	0.0000
BSC3	PDO	0.09	0.1178	0.40	-44	0.0000
BSC3	PNA	0.28	0.0000	0.30	3	0.0000
BSC4	AO	-0.27	0.0000	-0.51	-34	0.0000
BSC4	PDO	0.13	0.0261	0.32	50	0.0000
BSC4	PNA	0.12	0.0310	0.30	-50	0.0000

The AO is negatively correlated with the mean temperature across all of the BSC sections. Although the correlation coefficients are somewhat low (-0.27 to -0.33), they are statistically significant at the 95% level with a zero lag time. This suggests that a positive AO, which is associated with increased storminess or weakened high pressure in the central Arctic leads to lower temperatures along the slope in the Bering Sea; however such a connection, if it exists at all, would require further verification. Using a range of +/- 50 months lag time, some correlations are higher (up to -0.59); however, the interpretation of the lagged correlations is even less conclusive. Correlations of temperature across the BSC with the PDO/PNA do not appear to be consistent or sensible.

Correlations between the 13-month running mean net volume transport through Bering Sea straits/passes and large-scale weather indices (AO, PDO, and PNA) are shown in Table 14. Although there are some significant correlations between Aleutian Island passes and straits, a clear pattern does not emerge with any of the indices. The correlations are not consistent for a given weather index, instead they may be negative or positive along the Aleutian Island sections. This suggests that the inflow into the Bering Sea is not strongly related to large-scale weather patterns. As shown in Chapter IV, this inflow appears to be more closely related to the strength and position of the Alaskan Stream and mesoscale eddies within the stream and in the southern Bering Sea.

Table 14. Correlation coefficients between the net volume transport through Bering Sea cross-sections and large-scale weather indices. Correlations are for the 13-month running mean values of both the volume transport time series and the weather indices for 1979–2004. Correlations with no lag are shown (Corr. no lag) with the associated p-value. The maximum correlation (Max. Corr.) is also shown for a lag range of +/- 50 months, along with the lag time and p-value. A negative lag means that the volume transport through the cross-section is leading the weather index.

Section	Index	Corr. no lag	P-value	Max. Corr.	Lag	P-value
Unimak	AO	-0.13	0.0201	-0.35	11	0.0000
Unimak	PDO	0.15	0.0073	-0.45	-19	0.0000
Unimak	PNA	0.19	0.0010	0.41	-44	0.0000
Akutan	AO	-0.08	0.1765	0.40	-29	0.0000
Akutan	PDO	0.29	0.0000	0.56	9	0.0000
Akutan	PNA	0.09	0.1107	0.42	-46	0.0000
Umnak	AO	-0.05	0.3855	0.39	-34	0.0000
Umnak	PDO	0.27	0.0000	0.50	8	0.0000
Umnak	PNA	0.07	0.2027	0.35	-44	0.0000
StraitH	AO	-0.05	0.3852	0.18	-43	0.0046
StraitH	PDO	0.05	0.3836	-0.38	-19	0.0000
StraitH	PNA	0.07	0.2227	-0.20	-23	0.0006
Samalga	AO	-0.03	0.5671	0.46	-35	0.0000
Samalga	PDO	0.29	0.0000	0.45	7	0.0000
Samalga	PNA	0.05	0.4373	-0.34	-27	0.0000
StraitG	AO	-0.16	0.0048	-0.42	44	0.0000
StraitG	PDO	0.23	0.0001	-0.37	-21	0.0000
StraitG	PNA	0.14	0.0168	-0.34	-29	0.0000
Amukta	AO	-0.27	0.0000	-0.45	-33	0.0000
Amukta	PDO	0.17	0.0040	0.41	-7	0.0000
Amukta	PNA	0.36	0.0000	0.43	-7	0.0000
Seguam	AO	0.02	0.7751	0.46	-34	0.0000
Seguam	PDO	0.24	0.0000	0.52	8	0.0000
Seguam	PNA	0.06	0.2690	0.48	-48	0.0000
StraitF	AO	-0.09	0.1300	0.36	-35	0.0000
StraitF	PDO	0.27	0.0000	0.52	8	0.0000
StraitF	PNA	-0.01	0.8523	0.37	26	0.0000
StraitE	AO	-0.07	0.2518	0.43	-35	0.0000
StraitE	PDO	0.39	0.0000	0.50	5	0.0000

Section	Index	Corr. no lag	P-value	Max. Corr.	Lag	P-value
StraitE	PNA	0.01	0.8479	0.40	26	0.0000
StraitD	AO	-0.05	0.3979	0.36	-35	0.0000
StraitD	PDO	0.40	0.0000	0.48	4	0.0000
StraitD	PNA	-0.01	0.8926	0.38	26	0.0000
Amchitka	AO	0.02	0.6677	0.34	49	0.0000
Amchitka	PDO	-0.35	0.0000	0.54	-22	0.0000
Amchitka	PNA	-0.09	0.1097	0.32	38	0.0000
StraitC	AO	-0.13	0.0287	0.23	-50	0.0003
StraitC	PDO	0.18	0.0017	-0.52	45	0.0000
StraitC	PNA	-0.19	0.0007	0.35	16	0.0000
Buldir	AO	-0.21	0.0002	-0.61	11	0.0000
Buldir	PDO	0.22	0.0002	0.59	10	0.0000
Buldir	PNA	0.08	0.1442	-0.51	-13	0.0000
StraitB	AO	-0.05	0.4003	-0.34	22	0.0000
StraitB	PDO	-0.28	0.0000	0.38	18	0.0000
StraitB	PNA	-0.48	0.0000	-0.48	0	0.0000
Near 1	AO	0.00	0.9351	0.39	-27	0.0000
Near 1	PDO	0.08	0.1718	0.42	29	0.0000
Near 1	PNA	-0.20	0.0006	-0.22	3	0.0001
Near 2	AO	-0.16	0.0054	-0.30	-35	0.0000
Near 2	PDO	0.13	0.0212	0.46	-43	0.0000
Near 2	PNA	0.20	0.0005	0.32	-46	0.0000
Near	AO	-0.15	0.0112	0.32	19	0.0000
Near	PDO	0.16	0.0050	0.56	-44	0.0000
Near	PNA	0.07	0.1983	0.31	-48	0.0000
Kamchatka	AO	0.27	0.0000	0.27	1	0.0000
Kamchatka	PDO	-0.11	0.0485	-0.47	-43	0.0000
Kamchatka	PNA	-0.09	0.1343	-0.38	-48	0.0000
Anadyr	AO	-0.40	0.0000	-0.44	-11	0.0000
Anadyr	PDO	0.02	0.7045	0.23	12	0.0001
Anadyr	PNA	0.14	0.0128	0.40	-43	0.0000
Shpanberg	AO	-0.17	0.0028	0.28	-11	0.0000
Shpanberg	PDO	0.02	0.7862	-0.35	14	0.0000
Shpanberg	PNA	0.22	0.0001	-0.31	-50	0.0000
Bering	AO	-0.49	0.0000	-0.51	2	0.0000
Bering	PDO	0.03	0.5978	0.29	-38	0.0000
Bering	PNA	0.28	0.0000	0.34	-39	0.0000

In the northern Bering Sea, there appears to be a consistent pattern of correlation with the AO. The net volume transports across Anadyr, Shpanberg, and Bering straits all show significant (at the 95% level) negative correlations with the AO at a zero time lag. The correlation is highest for Bering Strait (-0.49), with lower values at Anadyr (-0.40) and Shpanberg (-0.17). The correlations can be slightly higher when lag times are used, however they are not consistent among the sections, which minimizes their physical meaning. There is also an indication of a weak, but significant (at the 95% level), positive correlation between the northern straits and the PNA; correlation coefficients range between 0.14 and 0.28, with Bering Strait showing the highest correlation.

B. PHYSICAL IMPACTS ON BIOLOGICAL PROCESSES

The shelf waters of the northern Bering Sea are supplied with nutrients via upwelling of water from the deep Bering Sea basin (Tsunogai et al. 1979). The model results in Chapter IV provide a mechanism for how and where this upwelled water reaches the shelf. A biological ‘hotspot’ has been identified southwest of St. Lawrence Island between the 40- and 70-m isobaths (Grebmeier and Cooper 1995). Model results show that a relatively strong source of on-shelf transport occurs south of this ‘hotspot’ in the Zhemchug Canyon region. Upwelling of nutrient-rich deep Bering Sea water due to eddies and shelf-basin exchange in general could enhance biological productivity in this region. For example, the eddy mentioned above in Section G of Chapter V, had a mean salinity of 33.12, which can be converted to a nitrate concentration of 19.06 μM and also a silica concentration of 41.98 μM (based on relations from data in Cooper et al. 1997). If the 3-month (October–December 1993) mean volume transport (0.416 Sv) across Zhemchug Canyon section is used, this yields a total of 3,912 kg of nitrate and 8,350 kg of silica advected onto the Bering Sea shelf through Zhemchug Canyon due to the eddy. Focusing on upwelled water (deeper than 100 m), the mean salinity is 33.36, which would be associated with a nitrate concentration of 21.13 μM and a silica concentration of 45.61 μM . Over the 3-month lifetime of the eddy, the mean volume transport (for water deeper than 100m) is 0.11 Sv, which would result in 1,146 kg of nitrate and 2,426 kg silica advected onto the Bering Sea shelf. It is important to note that these relationships

between salinity and nutrient concentrations are rough estimates. However, to my knowledge this is the first calculation of the amount of nitrate or silica provided to the shelf via an eddy along the Bering Sea slope.

Some of the highest silicate concentrations in the Bering Sea have been measured in the Gulf of Anadyr (on the western part of the shelf; Cooper et al. 1997); however these are diluted and biologically utilized within the euphotic zone downstream, as this water moves northward toward Bering Strait (Clement et al. 2005). Modeled EKE fields show that the northern Bering Sea maintains year-round high energy and mixing, especially in Bering and Anadyr straits. Notably, these regions of high EKE are found just upstream of highly productive areas in the Bering Sea (e.g., the Chirikov Basin and the region just north of Bering Strait) that have been identified in previous studies such as Grebmeier et al. (1988), Springer and McRoy (1993), and Grebmeier and Dunton, (2000). This suggests that high-nutrient Anadyr Water is mixed into the euphotic zone as it flows generally northward and, upon encountering a region of lower EKE, can support water column primary production and the settling of organic matter to the benthos.

C. DOWNSTREAM EFFECTS

Satellite records of the Arctic sea ice cover show a negative trend in ice extent and concentration since 1979 (Cavalieri et al. 1997; Comiso 2002; Meier et al. 2005; Parkinson et al. 1999; Serreze et al. 2003; Stroeve et al. 2005). This trend, superimposed over large seasonal and interannual variability (Comiso et al. 2003), has been coincident with the increase of the Northern Hemisphere Annular Mode (NAM also known as the AO) represented by a reduced winter weather regime over mid- to high-latitude continental regions of the Northern Hemisphere between late 1960s and mid 1990s (Thompson and Wallace 2001; Rigor et al. 2002). The warming as represented by the declining ice pack in the Arctic Ocean in summer has intensified during the late 1990's and into the 2000's, especially in the western Arctic Ocean as observed from satellites and *in situ* measurements (Comiso et al. 2003; McPhee et al. 2003; Morison et al. 2002). The primary result of this warming has been melting of the Arctic ice pack and the dramatic reduction of summer sea ice cover (Maslowski et al. 2007; Rothrock et al. 1999,

2003; Serreze et al. 2003; Wensnahan et al. 2007). Updated estimates of Arctic September sea ice extent indicate a negative trend of over 10% per decade since 1979 (Comiso et al. 2006; Stroeve and Maslowski 2007; Stroeve et al. 2005), with some of the lowest extents occurring in 2002–2007. During these summers, the reductions in sea ice cover were particularly pronounced in the western Arctic and in particular off the shores of Alaska and Siberia. It is important to note that this accelerated warming in the 2000s has occurred under a relatively neutral AO regime (while warming has been typically associated with high positive AO index), which poses important questions about the actual role of AO in sea ice variability (Overland and Wang 2005).

Recent reduction of the Arctic ice pack has been primarily associated with anomalies of surface air temperature and atmospheric circulation over the Arctic (Francis et al. 2005; Francis and Hunter 2006) and those in turn have been linked to the AO (Rigor et al. 2002). Such studies typically assume that external atmospheric forcing plays the dominant role and neglect effects of processes internal to the Arctic Ocean. Two processes that tend to be especially overlooked are the oceanic thermodynamic control of sea ice via under-ice ablation and lateral melt at marginal ice zones and downstream along the advection path of warm Pacific Water (Shimada et al. 2006). The absolute magnitude and long-term variability of oceanic heat flux into the western Arctic are not well known from observations and are typically poorly represented in models. However, those ice-ocean interactions at seasonal to interannual time scales may act to decorrelate AO forcing, which could help explain some of the timing issues between AO/atmospheric forcing and sea ice variability, especially during the last decade (Overland and Wang 2005).

It is hypothesized that the oceanic heat flux into the western Arctic Ocean is one of the main driving forces acting to reduce the sea ice cover there. In addition to the atmospheric forcing at the surface, the oceanic heat distributed above the halocline modulates the state of sea ice cover and determines regions of net growth/melt of sea ice and variability in multi-year and first-year ice distribution. The removal of sea ice along the Alaskan coast and from the Chukchi shelf for prolonged periods of time acts to

increase oceanic heat content in the upper ocean and its effects on sea ice in the Beaufort and East Siberian seas by increasing the surface albedo. Therefore, it is possible for the flow through Bering Strait to have an important effect of the initial melting of sea ice within the Chukchi Sea.

Heat fluxes through Bering Strait and through the Chukchi shelf appear to influence the distribution and thickness of sea ice (Shimada et al. 2006; Woodgate et al. 2010). Woodgate et al. (2010) combined near-bottom measurements of the velocity and temperature with satellite-derived SST to produce time series of the heat flux through Bering Strait. Estimates show a doubling of the heat flux between 2001 and 2007 ($2\text{--}3 \times 10^{20} \text{J/yr}$ to $5\text{--}6 \times 10^{20} \text{J/yr}$). Woodgate et al. (2010) suggest that heat flux variability across Bering Strait is slightly larger than the variability of the annual shortwave input to the Chukchi Sea between 1998 and 2007 (~ 3 and $4.5 \times 10^{20} \text{J/yr}$, respectively). Shimada et al. (2006) note that the distribution of warm Pacific Summer Water is similar to the spatial pattern of recent sea ice reduction since the late 1990s. However, there does not appear to be a direct link to Bering Strait throughflow, as increases in Pacific Summer Water temperatures in the basin do not correlate with the temperature of the upstream source water from the Bering Sea.

Model results suggest that moderate increases in the Bering Strait heat flux in the early 2000s combined with solar heating on the shelf of the Chukchi Sea produced an increase in the northward oceanic heat flux across the Chukchi Sea. Two-thirds of the heat flux entering the basin was contained in the Alaska Coastal Current, which showed much warmer temperatures and higher velocities during September of the 2000s as compared to the previous two decades (Maslowski and Clement Kinney 2011).

Freshwater flux from the Bering Sea into the Chukchi Sea is an important factor affecting stratification and the maintenance of the Arctic Ocean halocline (e.g., Aagaard et al. 1985a). This halocline separates the upper mixed layer from the deeper, warmer Atlantic layer. Any disturbance or reduction in the strength of the halocline could allow warm Atlantic Water to be mixed into the surface layer and possibly come into contact with the overlying sea ice. Multiple model results and observations presented in Chapter

VII show no long-term trends in the freshwater flux time series across Bering Strait over the 1979–2004 time period. However, the available measurements and multiple models all have problems representing the ACC contribution to the total freshwater flux (see additional comments below).

IX. OVERALL CONCLUSIONS

The use of a high-resolution (~9km) ice-ocean model with a large domain (pan-Arctic) allowed for a comprehensive analysis of the circulation and property exchange within the Bering Sea, as well as the communication from the south and to the north. This model represents a large step forward in the ability to simulate the mesoscale activity in the North Pacific and deep Bering Sea basin, which was shown to be a strong control on the flow into and out of the western Aleutian Island passes and straits. A long integration time (1979–2004) reveals the large interannual variability in the flow through both the southern and northern straits of the Bering Sea. Results show that representation of the mesoscale features within the Alaskan Stream, Western Subarctic Gyre, and the deep Bering Sea basin is critical in order to simulate the communication between the North Pacific and the Bering Sea. In addition, long-term continuous observations of the flow through the western passes are necessary to better understand the actual variability there and to constrain models.

The Bering Slope Current appeared to be more a system of eddies rather than a continuous feature, which indicates the need for a fully eddy-resolving model to represent the complex dynamics along the slope. There does not appear to be a north-south split of the BSC at Cape Navarin, instead the model results show that the main source water for the Gulf of Anadyr comes from the outer shelf flow, roughly between the 100 and 200-m isobaths. Important areas of shelf-basin exchange were identified along the Bering Slope, particularly within the canyons, such as Zhemchug and Bering canyons. Peaks in the on-shelf transport of salt and heat were shown to be associated with cyclonic eddies in Zhemchug Canyon, which makes this area important for supplying nutrients to the Bering Sea shelf, as well as the entire Western Arctic. An eddy was estimated to supply 3,912 kg of nitrate and 8,350 kg of silica during the 3 months when it was present within the canyon.

The model represented a major anomaly in the flow and sea ice distribution across the northern Bering Sea shelf. The anomaly, which also was apparent in satellite-derived

sea ice concentration data, was caused by an unusual wind pattern. Strong winds from a more easterly direction created an Ekman transport on the shelf which reversed the Anadyr Current and greatly increased the northward flow through Shpanberg Strait. Additional model results within the northern Bering Sea showed that increased EKE in Bering and Anadyr straits may help explain the areas of high biological productivity located just downstream in the Chirikov Basin and north of Bering Strait.

Estimates of the transport through Bering Strait from multiple models ranged from 0.67 (+/- 0.03) to 1.29 (+/- 0.06) Sv in the mean, compared to the observational estimate of 0.8 +/-0.2 Sv. Thus, most of the models agreed with the observational estimate to within errors. However, there is still a need to reduce the uncertainty in the accurate estimation volume transport and property fluxes through Bering Strait, both from observations and model results. Similar to the need for more observations in the western Aleutian passes, there is a need to observe the horizontal and vertical structure of the flow through Bering Strait, including the western portion, on a continuous basis. An effort is currently underway to provide more observations within Bering Strait and these measurements will be important for many future studies of the Pacific-Arctic region. Increases in model resolution and improvements in model bathymetry should improve the representation of the flow structure in Bering Strait, as indicated by initial spin-up results from a new, higher resolution version of the NAME model.

X. FUTURE DIRECTIONS

The lack of tides in the NAME model limits its ability to properly represent short period (~1–15 days) variability in areas where tides are important, such as within the Aleutian Island Passes (e.g., Kowalik 1999; Stabeno et al. 2002). Residual tidal currents occur when the energy of the basic tidal constituents is transferred to shorter and longer periods and the oscillating velocity interacts either with the sea surface or with bottom topography. Although observations on the formation of new wave periods are very few, it appears that residual currents can be an important contribution to the mean flow (Kowalik 1999).

Model bathymetry representation of some features at 9-km grid cell spacing, namely important passes and straits, does not always agree with the observed bathymetry. In general, there are local inaccuracies in the digital bathymetric dataset and the resolution of the digital bathymetry is coarse relative to the dimensions of the Aleutian Island passes and straits of the northern Bering Sea. Increased model resolution and an improved digital bathymetry for the passes and straits are expected to improve the model skill at these locations. Improvements in the 2-km version of the NAME model bathymetry should rectify some of these problems.

It seems likely that the seasonally- and surface-intensified Alaska Coastal Current (ACC) volume transport is not fully accounted for in large-scale models due to spatial resolution limitations. At the same time, the estimates presented here from observations also lack continuous measurements in the surface layers and near the coast. Although estimates of the contributions from the ACC and stratification have been made by Woodgate et al. (2006, 2010), quantification of the seasonal contribution to the Bering Strait transport is yet to be computed from either observations or models. The freshwater flux, which has a significant influence on the density structure of the Arctic Ocean (e.g., Aagaard et al. 1985b), would also be better measured if salinity information could be obtained in the upper layers and nearby the coast. Similarly, for heat flux, it is crucial to get information on the upper layers where maybe 1/3 of the heat is advected [see

Woodgate et al. (2010) who used satellite-derived sea surface temperatures to estimate the contribution from the upper layers]. An international effort is currently underway with 8 moorings placed in the Bering Strait region. New information from these moorings will be important for better understanding details of the flow through the strait and for constraining models.

While it is encouraging that, in many of the larger-scale models, fluxes of volume, heat and salt through the Bering Strait are of the right order of magnitude and in interannual terms show correlated variations with observations, there are still discrepancies. These have to be considered when using model results to look at the role of Pacific waters in the Arctic. There is also a need for models with higher spatial resolution in the Bering Strait region. The ACC is only order 10 km in width and thus not resolved by global or regional Arctic models with resolutions of 7–22 km (Table 7). The implementation of higher-resolution (2 km or less) regional models should improve estimates of the volume, heat and freshwater fluxes in the strait. The challenge is to be able to capture small-scale features, such as the Alaska Coastal Current and mesoscale eddies in the strait itself and its immediate vicinity. The modeling community is working toward that goal to properly represent such features.

LIST OF REFERENCES

- Aagaard K., Carmack E.C. (1989) The role of sea-ice and other fresh water in the Arctic circulation. *Journal of Geophysical Research* 94:14485–14498.
- Aagaard K., Roach A.T., Schumacher J.D. (1985a) On the wind-driven variability of the flow through Bering Strait. *Journal of Geophysical Research* 90:7213–7221.
- Aagaard K., Swift J.H., Carmack E.C. (1985b) Thermohaline circulation in the arctic Mediterranean seas. *Journal of Geophysical Research* 90:4833–4846.
- Adcroft A., Campin J.M. (2004) Rescaled height coordinates for accurate representation of free-surface flows in ocean circulation models. *Ocean Modelling* 7(3-4):269–284.
- Adcroft A., Hill C., Marshall J. (1997) The representation of topography by shaved cells in a height coordinate model. *Monthly Weather Review* 125(9):2293–2315.
- Ahlnäs K., Garrison G.R. (1984) Satellite and oceanographic observations of the warm coastal current in the Chukchi Sea. *Arctic* 37:244–254.
- Arakawa A. (1966) Computational design of long-term numerical integration of the equations of fluid motion. *Journal of Computational Physics* 1:119–143.
- Arsen'ev V.S. (1967) Currents and water masses of the Bering Sea, Nauka, Izdatel'stro.
- Barnier B., Madec G., Penduff T., Molines J.M., Treguier A.M., Le Sommer J., Beckmann A., Biastoch A., Böning C., Dengg J., Derval C., Durand E., Gulev S., Remy E., Talandier C., Theetten S., Maltrud M., McClean J., de Cuevas B.A. (2006) Impact of partial steps and momentum advection schemes in a global ocean circulation model at eddy permitting resolution. *Ocean Dynamics* 56:543–567. doi: 10.1007/s10236-006-0082-1.
- Barnston, A.G., Livezey R.E. (1987) Classification, seasonality and persistence of low-frequency atmospheric circulation patterns. *Monthly Weather Review*, 115, 1083–1126.
- Beamish, R.J. (1993) Climate and exceptional fish production off the west coast of North America. *Canadian Journal of Fisheries and Aquatic Sciences*, 50, 2270–2291.
- Blumberg A.F., Mellor G.L. (1987) A description of a three-dimensional coastal ocean circulation model. In: Heaps N (ed) *Three-dimensional coastal ocean models*, American Geophysical Union, Washington, D.C.

- Bond N.A., Overland J.E., Turet P. (1994) Spatial and temporal characteristics of the wind forcing of the Bering Sea. *Journal of Climate* 7:1119–1130.
- Brodeau L., Barnier B., Treguier A.M., Penduff T., Gulev S. (2010) An ERA40-based atmospheric forcing for global ocean circulation models. *Ocean Modelling* 31(3–4):88–104. doi: 10.1016/j.ocemod.2009.10.005.
- Busby M.S., Mier K.L., Brodeur R.D. (2005) Habitat associations of demersal fishes and crabs in the Pribilof Island region of the Bering Sea. *Fisheries Research* 75:15–28.
- Cavalieri D.J., Gloersen P., Parkinson C.L., Comiso J.C., Zwally H.J. (1997) Observed hemispheric asymmetry in global sea ice changes. *Science* 272:1104–1106.
- Chelton D.B., deSzoeke R.A., Schlax M.G., Naggar K.E., Siwertz N. (1998) Geographical variability of the first baroclinic Rossby radius of deformation. *Journal of Physical Oceanography* 28:433–460.
- Ciannelli L., Bailey K.M. (2005) Landscape dynamics and resulting species interactions: the cod-capelin system in the southeastern Bering Sea. *Marine Ecology Progress Series* 291:227–236.
- Clement J.L., Cooper L.W., Grebmeier J.M. (2004) Late winter water column and sea ice conditions in the northern Bering Sea. *Journal of Geophysical Research* 109(C3), C03022, doi:10.1029/2003JC002047.
- Clement J.L., Maslowski W., Cooper L., Grebmeier J., Walczowski W. (2005) Ocean circulation and exchanges through the northern Bering Sea–1979–2001 model results. *Deep-Sea Research II* 52:3509–3540. doi: 10.1016/j.dsr2.2005.09.010.
- Clement Kinney J., Maslowski M. (2008) Results of recent Pacific-Arctic ice-ocean modeling studies at the Naval Postgraduate School. *Chinese Journal of Polar Science* 19(2):230–236.
- Clement Kinney J., Maslowski W., Okkonen S. (2009) On the processes controlling shelf-basin exchange and outer shelf dynamics in the Bering Sea. *Deep-Sea Research II* 56:1351–1362, doi:10.1016/j.dsr2.2008.10.023.
- Coachman L.K., Aagaard K., Tripp R.B. (1975) Bering Strait: The regional physical oceanography. University of Washington Press, Seattle.
- Coachman L.K. (1993) On the flow field in the Chirikov Basin. *Continental Shelf Research* 13:481–508.

- Codispoti L.A., Flagg C., Kelly V., Swift J.H. (2005) Hydrographic conditions during the 2002 SBI process experiments. *Deep-Sea Research II* 52(24–26):3199–3226, doi: 10.1016/j.dsr2.2005.10.007.
- Cokelet E.D., Schall M.L., Dougherty D.M. (1996) ADCP-referenced geostrophic circulation in the Bering Sea Basin. *Journal of Physical Oceanography* 26:1113–1128.
- Cokelet E.D., Stabenro P.J. (1997) Mooring observations of the thermal structure, density stratification and currents in the southeast Bering Sea basin. *Journal of Geophysical Research* 102(C10):22947–22964 .
- Comiso J.C. (2002) A rapidly declining Arctic perennial ice cover. *Geophysical Research Letters* 29(20):1956, doi:10.1029/2002GL015650.
- Comiso J.C. (2006) Abrupt decline in the Arctic winter sea ice cover. *Geophysical Research Letters* 33:L18504, doi:10.1029/2006GL027341.
- Comiso J.C., Yang J., Honjo S., Krishfield R.A. (2003) Detection of change in the Arctic using satellite and in situ data. *Journal of Geophysical Research* 108:3384, doi:10.129/2002JC001347.
- Cooper L.W., Whitledge T.E., Grebmeier J.M., Weingartner T. (1997) The nutrient, salinity, and stable oxygen isotope composition of Bering and Chukchi Seas waters in and near the Bering Strait. *Journal of Geophysical Research* 102:12,5563–12,573.
- Crawford W.R., Cherniawski J.Y., Forman M.G.G. (2000) Multi-year meanders and eddies in the Alaskan Stream as observed by TOPEX/Poseidon altimeter. *Geophysical Research Letters* 27(7):1025–1028.
- Dai A., Trenberth K.E. (2002) Estimates of freshwater discharge from continents: latitudinal and seasonal variations. *Journal of Hydrometeorology* 3:660–687.
- Daru V., Tenaud C. (2004) High order one-step monotonicity-preserving schemes for unsteady compressible flow calculations. *Journal of Computational Physics* 193(2):563–594. doi: <http://dx.doi.org/10.1016/j.jcp.2003.08.023>.
- DRAKKAR Group (2007) Eddy-permitting ocean circulation hindcasts of past decades. *CLIVAR Exchanges* No 42:12(3) 8–10.
- Dukowicz J.K., Smith R.D. (1994) Implicit free-surface method for the Bryan-Cox-Semtner ocean model. *Journal of Geophysical Research* 99:7791–8014.

- Favorite F. (1974) Flow into the Bering Sea through Aleutian Island passes. In: Hood DW, Kelley EJ (eds) *Oceanography of the Bering Sea*, University of Alaska, Fairbanks.
- Fichefet T., Morales Maqueda M.A. (1997) Sensitivity of a global sea ice model to the treatment of ice thermodynamics and dynamics. *Journal of Geophysical Research* 102(C6):12609–12646.
- Flato G.M., Hibler W.D. III (1995) Ridging and strength in modeling the thickness distribution of Arctic sea ice. *Journal of Geophysical Research* 100:18,611–18,626.
- Fox-Kemper B., Menemenlis D. (2008) Can large eddy simulation techniques improve mesoscale rich ocean models? In: Hecht M, Hasumi H (eds) *Ocean Modeling in an Eddy Regime*, AGU, Washington, D.C.
- Francis J.A., Hunter E. (2006) New insight into the disappearing Arctic sea ice. *Eos Transactions of the of the American Geophysical Union* 87:509–524.
- Francis J.A., Hunter E., Key J.R., Wang X. (2005) Clues to variability in Arctic minimum sea ice extent. *Geophysical Research Letters* 32:L21501, doi:10.1029/2005GL024376.
- Frey K., Maslanik J., Clement Kinney J., Maslowski W. (2011) Recent variability of sea ice cover in the Pacific Arctic region, submitted.
- Gill A. (1982) *Atmosphere-Ocean Dynamics*. Academic Press Inc, Burlington, MA.
- Goosse H., Campin J.M., Fichefet T., Deleersnijder E. (1997) Sensitivity of a global ice–ocean model to the Bering Strait throughflow. *Climate Dynamics* 13(5): 349–358.
- Grebmeier J.M. et al. (2006) A major ecosystem shift in the northern Bering Sea. *Science* 311:1461–1464.
- Grebmeier J.M., Cooper L.W. (1995) Influence of the St. Lawrence Island Polynya upon the Bering Sea benthos. *Journal of Geophysical Research* 100(C3):4439–4460.
- Grebmeier J.M., Dunton K.H. (2000) Benthic processes in the northern Bering/Chukchi seas: status and global change. In: Huntington HP (ed) *Impacts of changes in Sea-ice and other environmental parameters in the Arctic*. Report of the Marine Mammal Commission Workshop, 15–17 February 2000, Girdwood, Alaska.
- Grebmeier J.M., McRoy C.P., Feder H.M. (1988) Pelagic-benthic coupling on the shelf of the northern Bering and Chukchi seas. I. Food supply source and benthic biomass. *Marine Ecology Progress Series* 48:57–67.

- Hare R.H., Mantua N.J. (2000) Empirical evidence for North Pacific regime shifts in 1977 and 1989 *Progress in Oceanography* 47 (2000) 103–145.
- Hare S.R., Mantua N.J., Francis R.C. (1999) Inverse production regimes: Alaskan and West Coast Salmon. *Fisheries* 24(1):6–14.
- Hermann A.J., Stabeno P.J., Haidvogel D.B., Musgrave D.L. (2002) A regional tidal/subtidal circulation model of the southeastern Bering Sea: development, sensitivity analyses and hindcasting. *Deep-Sea Research II* 49:5945–5967.
- Hibler W.D. III (1979) A dynamic thermodynamic sea ice model. *Journal of Physical Oceanography* 9(4): 815–846.
- Hibler W.D. III (1980) Modeling a variable thickness sea ice cover. *Monthly Weather Review* 108:1943–1973.
- Holland D.M. (2000) Merged IBCAO/ETOPO5 Global Topographic Data Product. National Geophysical Data Center (NGDC), Boulder CO. <http://www.ngdc.noaa.gov/mgg/bathymetry/arc-tic/ibcaorelatedsites.html>. Cited 25 Dec 2000.
- Hughes F.W., Coachman L.K., Aagaard K. (1974) Circulation, transport and water exchange in the western Bering Sea. In: Hood DW, Kelley EJ (eds) *Oceanography of the Bering Sea*, University of Alaska, Fairbanks.
- Jackett D.R., McDougall T.J. (1995) Minimal adjustment of hydrographic profiles to achieve static stability. *Journal of Atmospheric and Oceanic Technology* 12(2):381–389.
- Jakobsson M., Cherkis N., Woodward J., Macnab R., Coakley B. (2000) New grid of Arctic bathymetry aids scientists and mapmakers. *Eos Transactions of the American Geophysical Union* 81(9):89.
- Kalnay E. et al. (1996) The NCEP/NCAR 40-year reanalysis project. *Bulletin of the American Meteorological Society* 77:437–471.
- Kinder T.H., Coachman L.K., Galt J.A. (1975) The Bering Slope Current system. *Journal of Physical Oceanography* 5:231–244.
- Kinder T.H., Chapman D.C., Whitehead J.A. (1986) Westward intensification of the mean circulation on the Bering Sea shelf. *Journal of Physical Oceanography* 16:1217–1229.
- Kinder T.H., Schumacher J.D. (1981) Circulation over the continental shelf of the Southeastern Bering Sea. In: Hood DW, Calder JA (eds) *The eastern Bering Sea shelf: Oceanography and resources*, University of Washington Press, Seattle.

- Kinder T.H., Schumacher J.D., Hansen D.V. (1980) Observations of a baroclinic eddy: an example of mesoscale variability in the Bering Sea. *Journal of Physical Oceanography* 10:1228–1245.
- Kowalik Z. (1999) Bering Sea tides. In: *Dynamics of the Bering Sea*. Loughlin T.R., Ohtani K. (eds) University of Alaska Sea Grant, Fairbanks, AK.
- Large W.G., McWilliams J.C., Doney S. (1994) Oceanic vertical mixing: A review and a model with a nonlocal boundary layer parameterization. *Reviews of Geophysics* 32(4):363–403.
- Large W.G., Pond S. (1981) Open ocean momentum flux measurements in moderate to strong winds. *Journal of Physical Oceanography* 11(3):324–336.
- Large W.G., Pond S. (1982) Sensible and latent-heat flux measurements over the ocean. *Journal of Physical Oceanography* 12(5):464–482.
- Large W.G., Yeager S.G. (2004) Diurnal to decadal global forcing for ocean and sea-ice models: The data sets and flux climatologies. Technical Report TN-460+STR, NCAR, 105pp.
- Leith C.E. (1996) Stochastic models of chaotic systems. *Physica D* 98:481–491.
- Levitus S., Boyer T.P., Conkright M.E., O'Brian T., Antonov J., Stephens C., Stathopoulos L., Johnson D., Gelfeld R. (1998) World ocean database 1998. NOAA Atlas NESDID 18, US Government Printing Office, Washington, DC.
- Lique C., Treguier A.M., Scheinert M., Penduff T. (2009) A model-based study of ice and freshwater transport variability along both sides of Greenland. *Climate Dynamics* 33:685–705, doi:10.1007/s00382-008-0510-7.
- Losch M., Menemenlis D., Heimbach P., Campin J.M., Hill C. (2010) On the formulation of sea-ice models. part 1: effects of different solver implementations and parameterizations. *Ocean Modelling* 33:129–144.
- Macklin S.A., Hunt G.J. Jr., Overland J.E. (2002) Collaborative research on the pelagic ecosystem of the southeastern Bering Sea shelf. *Deep-Sea Research II* 49:5813–5819.
- Madec G. (2008) NEMO reference manual, ocean dynamic component: NEMO-OPA. Rep. 27, Note du pôle de modélisation, Institut Pierre Simon Laplace (IPSL), France. ISSN No. 1288–1619.
- Madec G., Delecluse P., Imbard M., Levy C. (1998) OPA 8.1 ocean general circulation model reference manual. IPSL Tech. Rep. Tech Rep. 11, Institut Pierre-Simon Laplace, 91pp.

- Mantua, N. J., Hare, S. R., Zhang, Y., Wallace, J. M., & Francis, R. C. (1997) A Pacific interdecadal climate oscillation with impacts on salmon production. *Bulletin of the American Meteorological Society*, 78, 1069–1079.
- Marble D.C. (2001) Simulated annual and seasonal Arctic Ocean and sea-ice variability from a high resolution, coupled ice-ocean model. Ph.D. Dissertation, Naval Postgraduate School, Monterey, California.
- Marchuk G.I., Kagan B.A. (1989) *Dynamics of Ocean Tides*. Kluwer Academic Publishers, Heidelberg.
- Marshall J., Adcroft A., Hill C., Perelman L., Heisey C. (1997) A finite-volume, incompressible Navier-Stokes model for studies of the ocean on parallel computers. *Journal of Geophysical Research* 102(C3): 5753–5766.
- Maslowski W., Clement Kinney J., Jakacki J. (2007) Towards prediction of environmental arctic change. *Computing in Science and Engineering* 9(6):29–34.
- Maslowski W., Roman R., Clement Kinney J. (2008a) Effects of mesoscale eddies on the flow of the Alaskan Stream. *Journal of Geophysical Research* 113:C07036, doi:10.1029/2007JC004341.
- Maslowski W., Clement Kinney J., Marble D.C., Jakacki J. (2008b) Towards eddy-resolving models of the Arctic Ocean. In: Hecht MW, Hasumi H (eds) *Ocean Modeling in an Eddying Regime*, Geophysical Monograph Series, Volume 177, American Geophysical Union, Washington, DC.
- Maslowski W., Clement Kinney J. (2011) Influence of oceanic circulation, heat fluxes and eddies on recent warming in the western Arctic: results of a high-resolution ice-ocean model. In preparation.
- McPhee M.G., Kikuchi T., Morison J.H., Stanton T.P. (2003) Ocean-to-ice heat flux at the North Pole environmental observatory. *Geophysical Research Letters* 30, doi:10.1029/2003GL018580.
- Meier W., Stroeve J., Fetterer F., Knowles K. (2005) Reductions in Arctic sea ice cover no longer limited to summer. *Eos Transactions of the American Geophysical Union* 86(36):326, doi:10.1029/2005EO360003.
- Melling H. (2000) Exchanges of fresh-water through the shallow straits of the North American Arctic. In: Lewis E.L. et al. (eds) *The Fresh-water Budget of the Arctic Ocean*. Proceedings of a NATO Advanced Research Workshop, Tallinn Estonia, 27 April–1 May 1998, Kluwer Academic Publishers Dordrecht Netherlands.

- Menemenlis D., Campin J., Heimbach P., Hill C., Lee T., Nguyen A., Schodlok M., Zhang H. (2008) ECCO2: High resolution global ocean and sea ice data synthesis. *Mercator Ocean Quarterly Newsletter* 31:13–21.
- Menemenlis D., Hill C., Adcroft A., Campin J., Cheng B., Ciotti B., Fukumori I., Heimbach P., Henze C., Koehl A., Lee T., Stammer D., Taft J., Zhang J. (2005) NASA supercomputer improves prospects for ocean climate research. *Eos Transactions of the Geophysical Union* 86 (9):89, 95–96.
- Mesinger F., Arakawa A. (1976) Numerical methods used in atmospheric models. WMO-ICSU Joint Organizing Committee, pp. 64.
- Mizobata K., Wang J., Saitoh S.I. (2006) Eddy-induced cross-slope exchange maintaining summer high productivity of the Bering Sea shelf break. *Journal of Geophysical Research* 111:C10017, doi:10.1029/2005JC003335.
- Morison J.H., Aagaard K., Falkner K.K., Hatakeyama K., Mortiz R., Overland J.E., Perovich D., Shimada K., Steele M., Takizawa T., Woodgate R. (2002) North Pole Environmental Observatory delivers early results. *Eos Transactions of the American Geophysical Union* 83:357–361.
- Muench R.D., Ahlnäs K. (1976) Ice movement and distribution in the Bering Sea from March to June 1974. *Journal of Geophysical Research* 81(24):4467–4476.
- Mueter F.J., Ladd C., Palmer M.C., Norcross B.L. (2006) Bottom-up and top-down controls of walleye Pollock (*Theragra chalcogramma*) on the Eastern Bering Sea shelf. *Progress in Oceanography* 68:152–183.
- Niebauer H.J. (1988) Effects of El Niño-Southern Oscillation and North Pacific weather patterns on interannual variability in the subarctic Bering Sea. *Journal of Geophysical Research* 93:5051–5068.
- Niebauer H.J., Day R.H. (1989) Causes of interannual variability in the sea ice cover of the eastern Bering Sea. *GeoJournal* 18:45–59.
- Niebauer H.J., Bond N.A., Yakunin L.P., Plotnikov V.V. (1999) An update on the climatology and sea ice of the Bering Sea. In: Loughlin T.R., Ohtani K. (eds) *Dynamics of the Bering Sea*. University of Alaska Sea Grant, Fairbanks, AK.
- Nguyen A.T., Menemenlis D., Kwok R. (2009) Improved modeling of the Arctic halocline with a subgrid-scale brine rejection parameterization. *Journal of Geophysical Research* 114:C11014, doi:10.1029/2008JC005121.
- Nguyen A.T., Menemenlis D., Kwok R. (2010) Arctic ice-ocean simulation with optimized model parameters: approach and assessment. *Journal of Geophysical Research* (accepted).

- Ohtani K. (1970) Relative transport in the Alaskan Stream in winter. *Journal of the Oceanography Society of Japan* 26:271–282.
- Okkonen S. (1993) Observations of topographic planetary waves in the Bering Slope Current using Geosat altimeter. *Journal of Geophysical Research* 98(12):22,603–22,613.
- Okkonen S.R. (1992) The shedding of an anticyclonic eddy from the Alaskan Stream as observed by the GEOSAT altimeter. *Geophysical Research Letters* 19(24):2397–2400.
- Okkonen S.R. (1996) The influence of an Alaskan Stream eddy on flow through Amchitka Pass. *Journal of Geophysical Research* 101(C4):8839–8851.
- Okkonen S.R., Schmidt G.M., Cokelet E.D., Stabenro P.J. (2004) Satellite and hydrographic observations of the Bering Sea ‘Green Belt’. *Deep-Sea Research II* 51:1033–1051, doi:10.1016/j.dsr2.2003.08.005.
- Onogi K., Tsutsui J., Koide H., Sakamoto M., Kobayashi S., Hatsushika H., Matsumoto T., Yamazaki N., Kamahori H., Takahashi K., Kadokura S., Wada K., Kato K., Oyama R., Ose N.M.T., Taira R. (2007) The jra-25 reanalysis. *Journal of the Meteorological Society of Japan* 85(3):369–432.
- Overland J.E. (1981) Marine climatology of the Bering Sea. In: Hood D.W., Calder J.A. (eds) *The eastern Bering Sea shelf: Oceanography and resources, volume one*. University of Washington Press, Seattle, WA.
- Overland J.E., Pease C.H. (1982) Cyclone climatology of the Bering Sea and its relation to sea ice extent. *Monthly Weather Review* 110:5–13.
- Overland J.E., Roach A.T. (1987) Northward flow in the Bering and Chukchi seas. *Journal of Geophysical Research* 92:7097–7105.
- Overland J.E., Spillane M.C., Hurlburt H.E., Wallcraft A.J. (1994) A numerical study of the circulation of the Bering Sea basin and exchange with the North Pacific Ocean. *Journal of Physical Oceanography* 24:736–758.
- Overland J.E., Wang M. (2005) The Arctic climate paradox: the recent decrease of the Arctic Oscillation. *Geophysical Research Letters* 32(6):L06701, doi: 10.1029/2004GL021752.
- Paluszkiwicz T., Niebauer H.J. (1984) Satellite observations of circulation in the eastern Bering Sea. *Journal of Geophysical Research* 89:3663–3678.

- Panteleev G.G., Nechaev D., Proshutinsky A.Y., Woodgate R., Zhang J. (2010) Reconstruction and analysis of the Chukchi Sea circulation in 1990–1991. *Journal of Geophysical Research* 115:C08023, doi:10.1029/2009JC005453.
- Panteleev G.G., Stabeno P., Luchin V.A., Nechaev D.A., Ikeda M. (2006) Summer transport estimates of the Kamchatka Current derived as a variational inverse of hydrophysical and surface drifter data. *Geophysical Research Letters* 33:L09609, doi:10.1029/2005GL024974.
- Paquette R.G., Bourke R.H. (1974) Observations on the Coastal Current of Arctic Alaska. *Journal of Marine Research* 32:195–207.
- Parkinson C.L., Washington W.M. (1979) A large-scale numerical mode of sea ice. *Journal of Geophysical Research* 84:311–337.
- Parkinson C.L., Cavalieri D.J., Gloersen P., Zwally H.J., Comiso J.C. (1999) Variability of the Arctic sea ice cover 1978–1996. *Journal of Geophysical Research* 104:20,837–20,856.
- Payne R.E. (1972) Albedo at the sea surface. *Journal of Atmospheric Science* 29:959–970.
- Pease C.H. (1980) Eastern Bering Sea ice processes. *Monthly Weather Review* 108(12):2015–2023.
- Penduff T., Le Sommer J., Barnier B., Treguier A.M., Molines J.M., Madec G. (2007) Influence of numerical schemes on current-topography interactions in $1/4^\circ$ global ocean simulations. *Ocean Science* 3:509–524.
- Prange M., Lohmann G. (2004) Variable freshwater input to the Arctic Ocean during the Holocene: implications for large-scale ocean-sea ice dynamics as simulated by a circulation model. In: Fischer H. et al. (eds) *The KIHZ project: towards a synthesis of Holocene proxy data and climate models*, Springer, New York.
- Prather M.C. (1986) Numerical advection by conservation of second-order moments. *Journal of Geophysical Research* 91:6671–6681.
- Reed R.K., Khen G.V., Stabeno P.J., Verkhunov A.V. (1993) Water properties and flow over the deep Bering Sea basin, summer 1991. *Deep-Sea Research* 40:2325–2334.
- Reed R.K., Stabeno P.J. (1993) The recent return of the Alaskan Stream to Near Strait. *Journal of Marine Research* 51:515–527.
- Rigor I.G., Wallace J.M., Colony R.L. (2002) Response of sea ice to the Arctic Oscillation. *Journal of Climate* 15(18):2648–2668.

- Rigor I.G., Wallace J.M., Colony R.L. (2002) Response of sea ice to the Arctic Oscillation. *Journal of Climate* 15(18):2648–2668.
- Roach A.T., Aagaard K., Pease C.H., Salo S.A., Weingartner T., Pavlov V., Kulakov M. (1995) Direct measurements of transport and water properties through the Bering Strait. *Journal of Geophysical Research* 100:18443–18457.
- Rogachev K., Carmack E. (2002) Evidence of trapping and amplification of near-inertial motions in a large anticyclonic ring in the Oyashio. *Journal of Oceanography* 58:673–682.
- Rogachev K.A., Gorin I.I. (2004) Mass transport and long-term evolution of eddies in the Kamchatka Current. *Oceanology* 44(1):15–21.
- Rogachev K., Shlyk N., Carmack E. (2007) The shedding of mesoscale anticyclonic eddies from the Alaskan Stream and westward transport of warm water. *Deep-Sea Research II* 54:2643–2656.
- Rothrock D.A., Yu T., Maykut G.A. (1999) Thinning of the Arctic sea-ice cover. *Geophysical Research Letters* 26(23):3469–3472.
- Rothrock D.A., Zhang J., Yu Y. (2003) The arctic ice thickness anomaly of the 1990s: a consistent view from observations and models. *Journal of Geophysical Research* 108(C3):28–37, doi:10.1029/2001JC001208.
- Royer T.C. (1981) Baroclinic transport in the Gulf of Alaska, part II. A freshwater driven coast current. *Journal of Marine Research* 39:251–266.
- Schumacher J.D., Aagaard K., Pease C.H., Tripp R.B. (1983) Effects of a shelf polynya on flow and water properties in the northern Bering Sea. *Journal of Geophysical Research* 88(C5):2723–2732.
- Schumacher J.D., Stabenro P.J. (1994) Ubiquitous eddies of the eastern Bering Sea and their coincidence with concentrations of larval pollock. *Fisheries Oceanography* 3:182–190.
- Semtner A.J. (1976) A model for the thermodynamic growth of sea ice in numerical investigation of climate. *Journal of Physical Oceanography* 6:376–389.
- Serreze M.C., Maslanik J.A., Scambos T.A., Fetterer F., Stroeve J., Knowles K., Fowler C., Drobot S., Barry R.G., Haran T.M. (2003) A new record minimum Arctic sea ice and extent in 2002. *Geophysical Research Letters* 30:1110, doi:10.1029/2002GL016406.

- Shimada K., Kamoshida T., Itoh M., Nishino S., Carmack E., McLaughlin F., Zimmermann S., Proshutinsky A. (2006) Pacific Ocean inflow: influence on catastrophic reduction of sea ice cover in the Arctic Ocean. *Geophysical Research Letters* 33:L08605, doi:10.1029/2005GL025624.
- Shuert P.G., Walsh J.J. (1993) A coupled physical-biological model of the Bering-Chukchi seas. *Continental Shelf Research* 13:543–573.
- Sigler M.F., Harvey H.R., Ashjian C.J., Lomas M.W., Napp J.M., Stabeno P.J., Van Pelt T.I. (2010) How does climate change affect the Bering Sea Ecosystem? *EOS Transactions of the American Geophysical Union* 91(48):457–558.
- Smith R.D., Dukowicz J.K., Malone R.C. (1992) Parallel ocean general circulation modeling, *Physica D* 60:38–61.
- Smith W.H.F., Sandwell D.T. (1997) Global sea floor topography from satellite altimetry and ship depth soundings. *Science* 277(5334):1956–1962.
- Solomon H., Ahlnäs K. (1978) Eddies in the Kamchatka Current. *Deep-Sea Research* 25:403–410.
- Spaulding M., Isaji T., Mendelsohn D., Turner A.C. (1987) Numerical simulation of wind-driven flow through the Bering Strait. *Journal of Physical Oceanography* 17:1799–1816.
- Springer A.M., McRoy C.P. (1993) The paradox of pelagic food webs in the northern Bering Sea. III. Patterns of primary production. *Continental Shelf Research* 13:575–599.
- Stabeno P.J., Reed R.K. (1992) A major circulation anomaly in the western Bering Sea. *Geophysical Research Letters* 19:1671–1674.
- Stabeno P.J., Reed R.K. (1993) Circulation in the Bering Sea basin observed by satellite-tracked drifters: 1986–1993. *Journal of Physical Oceanography* 24:848–854.
- Stabeno P.J., Reed R.K. (1994) Circulation in the Bering Sea Basin observed by satellite-tracked drifters: 1986–1993. *Journal of Physical Oceanography* 24:848–854.
- Stabeno P.J., Reed R.K., Napp J.M. (2002) Transport through Unimak Pass. *Deep-Sea Research II* 49:5919–5930.
- Stabeno P.J., Schumacher J.D., Ohtani K. (1999) The physical oceanography of the Bering Sea. In: Loughlin TR, Ohtani K (eds) *Dynamics of the Bering Sea*. University of Alaska Sea Grant, Fairbanks, AK.

- Steele M., Morley R., Ermold W. (2001) PHC: a global ocean hydrography with a high quality Arctic Ocean. *Journal of Climate* 14(9):2079–2087.
- Stroeve J.C., Serreze M.C., Fetterer F., Arbetter T., Meier W., Maslanik J., Knowles K. (2005) Tracking the Arctic's shrinking ice cover: another extreme September minimum in 2004. *Geophysical Research Letters* 32:L04501, doi:10.1029/2004GL021810.
- Stroeve J., Maslowski W. (2007) Arctic sea ice variability during the last half century. In: Brönnimann S., Luterbacher J., Ewen T., Diaz H.F., Stolarski R.S., Neu U. (eds) *Climate variability and extremes during the past 100 years*. Springer, Netherlands.
- Tabata T. (1974) Movement and deformation of drift ice as observed with sea ice radar, *Oceanography of the Bering Sea with Emphasis on renewable resourced*, Occas. Publ. 2, p. 373, Inst. of Mar. Sci. Univer. Of Alaska, Fairbanks.
- Thompson D.W.J., Wallace J.M. (2001) Regional climate impacts of the Northern Hemisphere Annular Mode. *Science* 293:85–89.
- Thorndike A.S., Rothrock D.A., Maykut G.A., Colony R. (1975) The thickness distribution of sea ice. *Journal of Geophysical Research* 80:4501–4513.
- Timmermann R., Goose H., Madec G., Fichefet T., Ethe C., Duliere V. (2005) On the representation of high latitude processes in the ORCA-LIM global coupled sea ice-ocean model. *Ocean Modelling* 8:175–201.
- Tsunogai S., Kusakabe M., Iizumi H., Koike I., Hattori A. (1979) Hydrographic features of the deep water of the Bering Sea – the sea of silica. *Deep Sea Research Part A* 26(6):641–659.
- Verkhunov A.V., Tkachenko Y.Y. (1992) Recent observations of variability in the western Bering Sea current system. *Journal of Geophysical Research* 97:14,369–14,376.
- Wallace J.M., Gutzler D.S. (1981) Teleconnections in the geopotential height field during the northern hemisphere winter. *Monthly Weather Review*, 109: 784–812.
- Walsh J.J., McRoy C.P., Coachman L.K., Goering J.J., Nihoul J.J., Whitley T.E., Blackburn T.H., Parker P.L., Wirick C.D., Shuert P.G., Grebmeier J.M., Springer A.M., Tripp R.D., Hansell D.A., Djenidi S., Deleersnijder E., Henriksen K., Lund B.A., Andersen P., Müller-Karger F.E., Dean K. (1989) Carbon and nitrogen cycling within the Bering/Chukchi Seas: source regions for organic matter effecting AOU demands of the Arctic Ocean. *Progress in Oceanography* 22:277–359.

- Walsh J.J., Dieterle D.A., Maslowski W., Whitledge T.E. (2004) Decadal shifts in biophysical forcing of marine food webs in the Arctic: numerical consequences. *Journal of Geophysical Research* 109, C05031, doi:10.1029/2003JC001945.
- Walsh J.J., Dieterle D.A., Maslowski W., Grebmeier J.M., Whitledge T.E., Flint M., Sukhanova I.N., Bates N., Cota G.F., Stockwell D., Moran S.B., Hansell D.A., McRoy C.P. (2005) A numerical model of seasonal primary production within the Chukchi/Beaufort Seas. *Deep-Sea Research* 52:3541–3576.
- Weingartner T.J., Danielson S., Sasaki Y., Pavlov V., Kulakov M. (1999) The Siberian Coastal Current: a wind- and buoyancy-forced Arctic coastal current. *Journal of Geophysical Research* 104:29697–29713, doi:10.1029/1999JC900161.
- Wensnahan M., Rothrock D., Hezel P. (2007) New arctic sea ice draft data from submarines. *EOS Transactions of the American Geophysical Union* 88:55.
- Woodgate R.A., Aagaard K., Weingartner T.J. (2005a) Monthly temperature, salinity, and transport variability of the Bering Strait throughflow. *Geophysical Research Letters* 32:L04601, doi:10.1029/2004GL021880.
- Woodgate R.A., Aagaard K., Weingartner T.J. (2005b) A year in the physical oceanography of the Chukchi Sea: Moored measurements from autumn 1990–1991. *Deep-Sea Research II* 52:3116–3149, doi:10.1016/j.dsr2.2005.10.016.
- Woodgate R.A., Aagaard K. (2005c) Revising the Bering Strait freshwater flux into the Arctic Ocean. *Geophysical Research Letters* 32:L02602, doi:10.1029/2004GL021747.
- Woodgate R.A., Aagaard K., Weingartner T.J. (2006) Interannual Changes in the Bering Strait Fluxes of Volume, Heat and Freshwater between 1991 and 2004. *Geophysical Research Letters* 33:L15609, doi:10.1029/2006GL026931.
- Woodgate R.A., Aagaard K., Weingartner T.J. (2007) First steps in calibrating the Bering Strait throughflow: Preliminary study of how measurements at a proposed climate site (A3) compare to measurements within the two channels of the strait (A1 and A2). 20 pp, University of Washington.
- Woodgate R.A., Weingartner T.J., Lindsay R.W. (2010) The 2007 Bering Strait oceanic heat flux and anomalous Arctic sea-ice retreat. *Geophysical Research Letters* 37:L01602, doi:10.1029/2009GL041621.
- Yin Z.-Y. (1994) Moisture conditions in the south-eastern USA and teleconnection patterns. *International Journal of Climatology*, 14: 947–967.
- Zhang J. (2005) Warming of the arctic ice-ocean system is faster than the global average since the 1960s. *Geophysical Research Letters*, doi:10.1029/2005GL024216.

- Zhang J., Hibler W.D. (1997) On an efficient numerical method for modeling sea ice dynamics. *Journal of Geophysical Research* 102:8691–8702.
- Zhang J., Rothrock D.A. (2001) A thickness and enthalpy distribution sea-ice model. *Journal of Physical Oceanography* 31:2986–3001.
- Zhang J., Rothrock D.A. (2003) Modeling global sea ice with a thickness and enthalpy distribution model in generalized curvilinear coordinates. *Monthly Weather Review* 131:681–697.
- Zhang J., Rothrock D.A. (2005) The effect of sea-ice rheology in numerical investigations of climate. *Journal of Geophysical Research*. doi:10.1029/2004JC002599.
- Zhang J., Steele M., Lindsay R.W., Schweiger A., Morison J. (2008) Ensemble one-year predictions of arctic sea ice for the spring and summer of 2008. *Geophysical Research Letters*, doi:10.1029/2008GL033244.
- Zhang J., Woodgate R., Moritz R. (2010) Sea ice response to atmospheric and oceanic forcing in the Bering Sea. *Journal of Physical Oceanography* (in press).
- Zhang Y., Wallace J.M., Battisti D.S. (1997) ENSO-like interdecadal variability: 1900–93. *Journal of Climate* 10:1004–1020.
- Zhang Y., Maslowski W., Semtner A.J. (1999) Impact of mesoscale ocean currents on sea ice in high-resolution Arctic ice and ocean simulations. *Journal of Geophysical Research* 104(C8):18409–18430.

THIS PAGE INTENTIONALLY LEFT BLANK

INITIAL DISTRIBUTION LIST

1. Defense Technical Information Center
Ft. Belvoir, Virginia
2. Dudley Knox Library
Naval Postgraduate School
Monterey, California
3. Dr. Wieslaw Maslowski
Naval Postgraduate School
Monterey, California
4. Dr. John Walsh
University of South Florida
St. Petersburg, Florida
5. Dr. Mary Batteen
Naval Postgraduate School
Monterey, California
6. Dr. Peter Guest
Naval Postgraduate School
Monterey, California
7. Dr. Robin Tokmakian
Naval Postgraduate School
Monterey, California
8. Dr. Jacqueline Grebmeier
Chesapeake Biological Laboratory
Solomons, Maryland
9. Dr. Lee Cooper
Chesapeake Biological Laboratory
Solomons, Maryland
10. Dr. Andrew Roberts
Naval Postgraduate School
Monterey, California

11. Dr. Robert Osinski
Institute of Oceanology Polish Academy of Sciences
Sopot, Poland
12. Dr. Jaromir Jakacki
Institute of Oceanology Polish Academy of Sciences
Sopot, Poland
13. Dr. Anjuli Bamzai
National Science Foundation
Arlington, Virginia
14. Dr. Erica Key
National Science Foundation
Arlington, Virginia
15. Dr. Neil Swanberg
National Science Foundation
Arlington, Virginia
16. Dr. William Wiseman
National Science Foundation
Arlington, Virginia
17. Dr. Dorothy Koch
United States Department of Energy
Washington DC
18. Dr. Renu Joseph
United States Department of Energy
Washington DC
19. Dr. Scott Harper
Office of Naval Research
Arlington, Virginia